

Microstructure Optimization to Prevent Hydrogen-Induced Cracking of API X70 Pipeline Steels in Sour Environments

A Thesis Submitted to the College of
Graduate and Postdoctoral Studies
In Partial Fulfillment of the Requirements
For the Degree of Master of Science
In the Department of Mechanical Engineering
University of Saskatchewan
Saskatoon

By
Reza Pourazizi

PERMISSION TO USE

In presenting this thesis in partial fulfillment of the requirements for a postgraduate degree from the University of Saskatchewan, I agree that the Libraries of this University may make it freely available for inspection. I further agree that permission for copying of this thesis in any manner, in whole or in part, for scholarly purposes may be granted by the professor who supervised my thesis work or, in their absence, by the Head of the Department or the Dean of the College in which my thesis work was done. It is understood that any copying or publication or use of this thesis or parts thereof for financial gain shall not be allowed without my written permission. It is also understood that due recognition shall be given to me and to the University of Saskatchewan in any scholarly use, which may be made of any material in my thesis.

Requests for permission to copy or to make other use of the material in this thesis in whole or part should be addressed to:

Head of the Department of Mechanical Engineering
University of Saskatchewan
57 Campus Drive
Saskatoon, Saskatchewan, S7N 5A9
Canada

OR

Dean
College of Graduate and Postdoctoral Studies
University of Saskatchewan
116 Thorvaldson Building, 110 Science Place
Saskatoon, Saskatchewan S7N 5C9

ABSTRACT

These days, by increasing the demand for oil and gas resources, the failure of pipeline steels has become one of the crucial topics in the oil and gas transportation industry. The failure of pipeline steels is divided into two major categories: stress corrosion cracking (SCC) and hydrogen assistant cracking (HAC). Hydrogen-induced cracking (HIC) is the main cause of pipeline steels failure in sour environments, which is categorized as a type of HAC. In this type of failure, hydrogen atoms accumulate in the steel and cause cracking by different mechanisms. The main focus of this thesis is to find the effects of texture and microstructural parameters on HIC nucleation and propagation in steels exposed to sour environments and also the effect of such environment on the mechanical properties of steels with different microstructure and texture.

In this thesis, the electrochemical hydrogen charging experiment was used to introduce HIC in API 5L X70 pipeline steels with four different thermo-mechanical control processing (TMCP) parameters. Using the scanning electron microscope (SEM), HIC cracks at the cross-section of samples were observed. The SEM observations indicate that the sample which had more finish rolling steps and smaller grain size was more susceptible to HIC. However, the specimen with larger grains was more susceptible to hardness increment than the steels with smaller grains. The energy dispersive Spectrometer (EDS) results showed that two types of inclusions, namely calcium sulfide (CaS) and aluminum oxide (Al_2O_3), were responsible for the nucleation of HIC in all examined API 5L X70 samples in sour environments. Comparing the length and quantity of the cracks in the middle and top layers of all samples, it could be concluded that the middle layer was more susceptible to HIC. The martensite phase accumulated around the HIC crack was recognized as the weakest phase that could resist HIC propagation and the specimen which had more deformed grains was more susceptible to HIC.

The hydrogen permeation (HP) test was used to indicate the type of traps in each sample. My experimental results indicated that there are both reversible and irreversible traps in all samples, but the quantity of reversible traps was higher in the samples with smaller grains. These results showed that the increasing the finish rolling steps and cooling rate made the steel more susceptible to the HIC. However, lower cooling rate, more roughing and less finishing reduction steps led to large grains, which were more resistance to the HIC.

The effect of different testing environments, including sour and acidic environments, on the tensile strength and type of failure of X70 pipeline steels were investigated. The results indicate that the acidic environment does not have any significant effect on the failure type and mechanical properties of the samples while the sour environment causes hydrogen embrittlement, and as a result, a brittle fracture happens. The other result achieved by tensile test is that the middle layer of the pipeline slab is generally weaker than the top layer, and the reason is the difference in the microstructure and texture of these layers.

ACKNOWLEDGEMENT

I want to thank three persons who supported me during my program. First, I want to express my sincere gratitude to my supervisor, **professor Szpunar** for his valuable advice and supports during my program. Without his support, I would never have been able to complete my MSc. He always gave me enough motivation to become a material scientist, and he was who nominated me for Dean's scholarship and supported me financially to start studying in Canada. The second person who really influenced my progress was Dr. Mohtadi-Bonab. He always pushed me to work and step in a correct way. He helped me in publishing my papers and always corrected my attitude and misunderstanding of concepts. Last, but not least, I want to thank my wife. She was always beside me in all circumstances and tolerated so much uncomfotables to let me reach my goals. She was the person who compensated for my shortages in confronting difficulties and had the primary role in rearing our girl.

My appreciation also goes to my advisory committee members, Prof. Duncan Cree, Prof. Ikechukwuka N. Oguocha and Prof. Mohamed Boulfiza as well as chair of committee Prof. Akindele G. Odeshi for their advice and help. My gratitude also goes to the mechanical engineering departmental assistants, Nanfang Zhao and Robert Peace, for their training and permission to use the resources for sample preparations.

Finally, I would like to thank the R&D team of EVRAZ Inc. located in Regina for providing the steel specimens.

DEDICATION

I dedicate this thesis to my lovely **wife** for her unconditioned kindness and support.

TABLE OF CONTENTS

PERMISSION TO USE	i
ABSTRACT.....	ii
ACKNOWLEDGEMENT	iv
DEDICATION.....	v
TABLE OF CONTENTS.....	vi
LIST OF TABLES	ix
LIST OF FIGURES	x
LIST OF ABBREVIATIONS.....	xiii
LIST OF SYMBOLS	xiv
CHAPTER 1: INTRODUCTION	1
1.1 Overview.....	1
1.2 Motivation.....	1
1.3 Objectives	2
1.4 Thesis arrangement	2
CHAPTER 2: LITERATURE REVIEW	3
2.1 Overview.....	3
2.2 Introduction.....	3
2.3 Pipeline steel failure modes	4
2.2.1 Stress corrosion cracking.....	4
2.2.2 Sulfide stress cracking (SSC)	8
2.2.3 Hydrogen induced cracking (HIC)	9
2.3 Effects of microstructure on HIC susceptibility	16
CHAPTER 3: MATERIAL AND EXPERIMENTAL PROCEDURE	19
3.1 Overview.....	19

3.2 Material	19
3.3 Experimental procedure	19
3.3.1 HIC testing.....	19
3.3.2 Permeation testing	21
3.3.3 Mechanical testing	25
3.3.4 Thermo-Mechanical Control Processing (TMCP) of the samples	27
3.3.5 Microstructural evaluation.....	29
3.3.6 Phase identification.....	29
CHAPTER 4: RESULTS AND DISCUSSION.....	31
4.1 Microstructure evaluation of as-received samples.....	31
4.2 Texture and phase characterization of as-received samples	35
4.3 Mechanical testing	44
4.3.1 Tensile and hardness testing results.....	44
4.3.2 Fractography of failed samples.....	47
4.4 HIC testing results.....	52
4.5 Texture characterization of the samples around the cracks	56
4.6 Hydrogen permeation testing results	63
4.7 Results analysis.....	64
4.7.1 Effects of TMCP parameters on the microstructure, texture, and mechanical properties of the samples	64
4.7.2 Effects of environmental conditions on the mechanical properties of specimens	66
CHAPTER 5: CONCLUSION AND RECOMMENDATIONS	67
5.1 Overview.....	67
5.2 Conclusions.....	67
5.3 Recommendations for future researches.....	70

5.3.1 Potential areas for the future researches	70
5.3.2 Suggested improvements to experimental setup	70
REFERENCES	72
APPENDIX A: LIST OF PUBLICATIONS FROM THIS STUDY	82
APPENDIX B: ELSEVIER PERMISSION FOR USING PUBLISHED PAPER IN MY THESIS	83

LIST OF TABLES

Table 3.1. Chemical composition of API 5L X70 pipeline steel samples (Wt.%).....	19
Table 3.2. TMCP parameters of X70-2 and X70-3 specimens.....	28
Table 3.3. The rolling pass reductions in the specimens.....	29
Table 4.1. Grain size distribution of the samples.....	34
Table 4.2. The recrystallization fraction of BCC phase in the samples.....	43
Table 4.3. Mechanical properties of the samples before and after hydrogen charging.....	45
Table 4.4. Statistics of blisters and cracks on electrochemically charged samples.....	54
Table 4.5. Recrystallization fraction of grains around the cracks.....	62
Table 4.6. Permeation test results.....	63

LIST OF FIGURES

Figure 2.1. Causes of oil and gas transmission pipeline significant incidents[7].....	4
Figure 2.2. (a) Intergranular SCC failure in service; (b) Transgranular SCC in laboratory test with specimen exposed to simulated ground water containing CO ₂ , showing lateral corrosion on crack sides [12].....	5
Figure 2.3. Potential-pH diagram showing the regimes for IGSCC and TGSCC at 24° C in solutions containing different amounts of CO ₃ ²⁻ , HCO ₃ ⁻ , and CO ₂ to achieve different pH values [12].....	6
Figure 2.4. Cyclic stress-strain data at 75°C for various fluctuating components of stress (appended to the lines in MN/m ²) and the monotonic slow strain rate curves at the same temperature for steel [22].....	7
Figure 2.5. Longitudinal section of an X100 specimen loaded at 65%YS showing main SSC crack (right of image) and small micro-cracks (left of image) (light) [37].....	9
Figure 2.6. Stages of hydrogen material interactions [42].....	10
Figure 2.7. HIC mechanism according to internal pressure theory.....	11
Figure 2.8. Hydrogen permeation cell (constructed of polytetrafluoroethylene) with double junction electrodes [69].....	13
Figure 3.1. Schematic of hydrogen charging of samples.....	20
Figure 3.2. Schematic of top and middle layers prepared from the bulk rectangular plate.....	21
Figure 3.3. Assembly of permeation testing.....	22
Figure 3.4. Permeation test wire connections.....	23
Figure 3.5. Typical hydrogen permeation result after two polarizations.....	24
Figure 3.6. Tensile testing equipment [120].....	26
Figure 3.7. The dimensions of tensile test samples.....	27
Figure 3.8. Schematic diagram of the rolling process for a) X70-2 and b) X70-3 steels.....	28
Figure 4.1. Micro structure of X70-1 sample at a) middle b) top layers.....	31
Figure 4.2. Microstructure of a) X70-2-1, b) X70-2-2, c) X70-3-1, d) X70-3-2 samples at middle layer.....	32

Figure 4.3. Microstructure of a) X70-2-1, b) X70-2-2, c) X70-3-1, d) X70-3-2 samples at top layer.....	32
Figure 4.4. The grain size of a) X70-1, b) X70-2-1, c) X70-2-2, d) X70-3-1, e) X70-3-2 samples at middle layer.....	33
Figure 4.5. The grain size of a) X70-1, b) X70-2-1, c) X70-2-2, d) X70-3-1, e) X70-3-2 samples at top layer.....	34
Figure 4.6. The Phase map of a) X70-1, b) X70-2-1, c) X70-2-2, d) X70-3-1, e) X70-3-2 samples at middle layer.....	36
Figure 4.7. The Phase map of a) X70-1, b) X70-2-1, c) X70-2-2, d) X70-3-1, e) X70-3-2 samples at top layer.....	37
Figure 4.8. The IPF a) X70-1, b) X70-2-1, c) X70-2-2, d) X70-3-1, e) X70-3-2 samples at middle layer.....	38
Figure 4.9. The IPF a) X70-1, b) X70-2-1, c) X70-2-2, d) X70-3-1, e) X70-3-2 samples at top layer.....	39
Figure 4.10. The KAM map of a) X70-1, b) X70-2-1, c) X70-2-2, d) X70-3-1, e) X70-3-2 samples at middle layer.....	40
Figure 4.11. The KAM map of a) X70-1, b) X70-2-1, c) X70-2-2, d) X70-3-1, e) X70-3-2 samples at top layer.....	41
Figure 4.12. The recrystallization fraction of a) X70-1, b) X70-2-1, c) X70-2-2, d) X70-3-1, e)X70-3-2 samples at middle layer.....	42
Figure 4.13. The recrystallization fraction of a) X70-1, b) X70-2-1, c) X70-2-2, d) X70-3-1, e)X70-3-2 samples at top layer.....	43
Figure 4.14. Stress-Strain diagram of the samples.....	44
Figure 4.15. Stress-Strain diagram of a) middle, and b) top layer of X70-1 steel in different environmental conditions.....	46
Figure 4.16. SEM images from fracture surface of X70-1 in a) Air condition, b) Acidic environment, c) Ex-Situ testing after 24h hydrogen charging, d) In-Situ testing after 24h hydrogen charging, e)In-Situ testing without initial hydrogen charging.....	48-50
Figure 4.17. EDS images from fracture surface of electrochemically charged samples.....	51-52

Figure 4.18. The examples of blisters on a) X70-1, b) X70-2-1, c) X70-2-2, d) X70-3-1, e) X70-3-2 surfaces.....	53-54
Figure 4.19. The examples of cracking on a) X70-2-1, b) X70-2-2 and c) X70-3-2 cross-sections.....	55-56
Figure 4.20. a) The phase map, b) IPF, c) Misorientation, d) Grain size and e) Recrystallization fraction of X70-1 around the crack.....	57
Figure 4.21. a) The phase map, b) IPF, c) Misorientation, d) Grain size and e) Recrystallization fraction of X70-2-1 around the crack.....	58
Figure 4.22. a) The phase map, b) IPF, c) Misorientation, d) Grain size and e) Recrystallization fraction of X70-2-2 around the crack.....	59
Figure 4.23. a) The phase map, b) IPF, c) Misorientation, d) Grain size and e) Recrystallization fraction of X70-3-1 around the crack.....	60
Figure 4.24. a) The phase map, b) IPF, c) Misorientation, d) Grain size and e) Recrystallization fraction of X70-3-2 around the crack.....	61

LIST OF ABBREVIATIONS

API	American Petroleum Institute
AF	Acicular ferrite
B	Bainite
CSL	Coincidence site lattice
DP	Degenerate pearlite
EBSD	Electron backscatter diffraction
EDS	Energy dispersive spectroscopy
FRT	Finish rolling temperature
HAGBs	High angle grain boundaries
HE	Hydrogen embrittlement
HIC	Hydrogen induced cracking
HP	Hydrogen permeation
HSLA	High strength low alloy
IEA	International Energy Agency
IPF	Inverse pole figure
ISO	International Organization for Standardization
KAM	Kernel average misorientation
LAGBs	Low angle grain boundaries
ND	Normal direction
ODF	Orientation distribution function
OM	Optical microscopy
PF	Polygonal ferrite
SEM	Scanning electron microscope
SCC	Stress corrosion cracking
SSC	Sulfide stress cracking
QF	Quasi polygonal ferrite
RD	Rolling direction
TD	Transverse direction

LIST OF SYMBOLS

C_{app}	Apparent hydrogen solubility, mol. cm ⁻³
D_{eff}	Effective hydrogen diffusion coefficient, cm ² .s ⁻¹
I_{∞}	Steady-state current, μ A
$J_{\infty}L$	Hydrogen permeability, mol. cm ⁻¹ . s ⁻¹
N_t	Total number of hydrogen trapping sites per cm ³
N_r	Number of reversible hydrogen trapping sites per cm ³
N_{ir}	Number of irreversible hydrogen trapping sites per cm ³
T_L	Time lag, s
λ	Degree of freedom
σ	Standard deviation
%	Percentage

CHAPTER 1: INTRODUCTION

1.1 Overview

This chapter briefly defines the motivation for the thesis followed by the objectives of the research. Finally, the thesis arrangement is presented.

1.2 Motivation

By growing the population and improving the living standards, the demand for oil and gas resources, besides other types of energies, have been increased and are expected to be increased by 27% until 2040 [1]. The safest and cheapest method of transporting these resources is using the pipeline steels. The big oil and gas pipeline supplier companies all around the world, especially in North America, spent lots of money annually to improve the quality of their pipeline steels [2]. As an example, the Enbridge company invested about 12.1 million USD in 2019 for the research and development of its products [3]. One of their un-answered questions is how to increase the resistance of pipeline steels against HIC that occur in sour environments. All companies develop their products to manufacture pipeline steel, which has higher strength and, at the same time, be resistant to HIC as it is believed that by increasing the steel strength, its resistance to the HIC will be decreased. HIC depends on many parameters such as chemical composition, structure and morphology of inclusions, the service environment parameters and microstructural texture parameters. All these parameters affect the mechanical strength of the pipeline steels too. Therefore, optimizing the parameters is the question that needs to be answered.

The motivation for this work is to improve understanding of the role of TMCP parameters on HIC susceptibility of pipeline steels and evaluate the effects of different service environments on their mechanical strength. Different TMCP parameters lead to different microstructural texture, trapping sites, inclusion and grain boundary distributions, which all of them affect the HIC susceptibility of steels. This thesis specifically focused on texture and grain boundary distribution of steels around HIC to anticipate the cracking path in the sour environments and suggest the best TMCP parameters of X70 pipeline steel, which create most HIC resistance texture in the steel. Moreover, the effects of different service environments on the mechanical properties of X70

pipeline steels will be examined. Besides these, the impact of varying TMCP parameters on the trapping sites and role of different inclusions on the initiation of cracking in the service environments will be evaluated. This thesis helps produce better HIC resistance X70 pipeline steels, resulting in improvements in the safety and reliability of transporting sour gas and oils. Besides, pipeline steels which are used for the sour service environments might also be used to transport hydrogen that is expected to become a clean fuel for the future economy.

1.3 Objectives

The main goals of this research are to evaluate the role of texture in HIC susceptibility of API X70 pipeline steels and estimate the effect of different environments on the mechanical properties of investigated steel specimens. The specific objectives are as below.

1- Determine the effects of different TMCP parameters on the microstructural texture of API 5L X70M pipeline steels.

2- Evaluate the relationship between different microstructure, texture, and mechanical properties and HIC susceptibility of API 5L X70M pipeline steels.

3- Assess the role of different service environments (sour and acidic environments) on the mechanical properties of API 5L X70M pipeline steels and understand the parameters that affect the resistance of steels to failure in different environments.

1.4 Thesis arrangement

This thesis contains five chapters. All chapters have a brief overview. The first chapter includes the motivation, objectives and arrangement of the thesis. The second chapter includes problem definition and the literature review. In the third chapter, the material and experimental procedures are explained. In the fourth chapter, the results, discussions and analysis of the results are presented. Finally, the fifth chapter contains a conclusion of this study and recommendations for future works.

CHAPTER 2: LITERATURE REVIEW

2.1 Overview

This chapter first define the problem and introduce different type of failure modes occur in pipeline steels and the efforts have been done by researchers to prevent these failures. HIC failure, which is the focus of this study, is explained specifically with more details including the mechanism of the failure and effect of different parameters like microstructure and texture parameters on it.

2.2 Introduction

One of the most challenging matters that the oil and gas industry faced with it is the transportation of these resources. The pipeline steels were used to transport the majority of oil and gas resources, because it is quicker, safer and cheaper method of transportation in compare with other methods such as using train and tanker ships [4]. However, using pipeline steels caused too many expenses annually, itself. In addition to the initial cost of pipeline steels, the failure of pipelines, specifically the corrosion of them, is the most portion of these expenses as these pipeline steels usually work at harsh conditions like sour environments (Figure 2.1). According to the report of National Association of Corrosion Engineers (NACE) in 2016, about 2.5 trillion USD is the cost of pipeline steels corrosion in this industry, which is 3.4% of the world's gross domestic product (GDP)[5]. However, this number does not include the environmental problems and safety expenses. This is the evidence of importance of the pipeline steels corrosion in oil and gas industry. To minimize the amount of these expenses, the first step is to recognize the type of pipelines failure. The National Energy Board (NEB) of Canada reported that more than one third of the pipeline steels failure is related to the cracking [6]. In the following sections, different type of pipeline steels cracking will be explained.

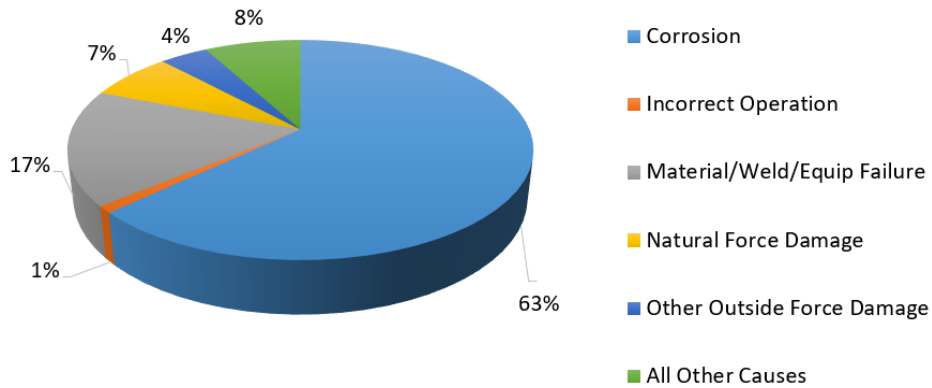


Figure 2.9. Causes of oil and gas transmission pipeline significant incidents [7].

2.3 Pipeline steel failure modes

Low carbon steels are used for construction of pipelines in the oil and gas transportation systems due to their desirable mechanical properties. However, pipeline steels might fail after some years and the failure is often a catastrophic accident. Therefore, engineers and scientists have tried to investigate and suggest practical solutions to improve the resistance to the failure for many years. Although many efforts have been made to characterize and mitigate the failures, this problem has to be further investigated to improve safety of oil and gas transport.

The failure of pipeline steels in oil and gas industry is most often classified as stress corrosion cracking (SCC) and the hydrogen assisted cracking (HAC). HAC can be then related to hydrogen induced cracking (HIC) or sulphide stress cracking (SSC), where the first one is in the absence of stress while the second is under stress. In this chapter, a brief review of each of these processes is followed by a detailed literature review where the effects of different parameters on HIC are explained.

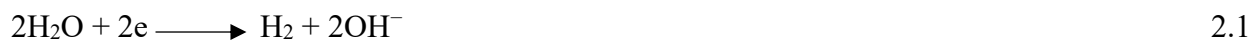
2.2.1 Stress corrosion cracking

One of the most important failure modes in pipeline steels is stress corrosion cracking (SCC). In this type of failure, cracks initiate and propagate in a corrosive environment at the presence of stresses and usually in higher than room temperatures [8].

Three different factors affect SCC in pipeline steels [9]. 1) Environmental factors like water chemistry in the field, including oxygen and ionic concentrations in the groundwater 2) Mechanical factors including the residual stress and applied stress from inside or outside of the

pipeline 3) Metallurgical factors like chemical composition of steel. Depending on the environment of service some of these factors can be considered more important than others.

Pipeline steels usually are protected with coatings and cathodic protection. After some times, the coating protecting against corrosion can be destroyed. By destroying the coating of the pipelines, the damaged coating shield is exposed to the cathodic current flow on the pipeline surface and water will contact the surface of the pipelines [10]. The chemical composition of water beside the pipelines depends on some factors like cathodic protection current that makes different pH for water [10]. High cathodic current generates the hydroxyl ions and increase the pH by these reactions:



Some other factors involving carbon dioxide (CO_2) gas also change the pH of the solution around the pipeline by converting the bicarbonate to carbonate ions [11].

Now, according to the pH of the surrounding solution, the SCC will occur. In the pH close to 7, the near-neutral SCC will happen. This kind of SCC is transgranular stress corrosion cracking (TGSCC) and the cracks initiate and propagate across or through the grains (Figure 2.2). TGSCC is usually a straight cracking without any branches, and the edges of cracks are usually corroded which make wider cracks.

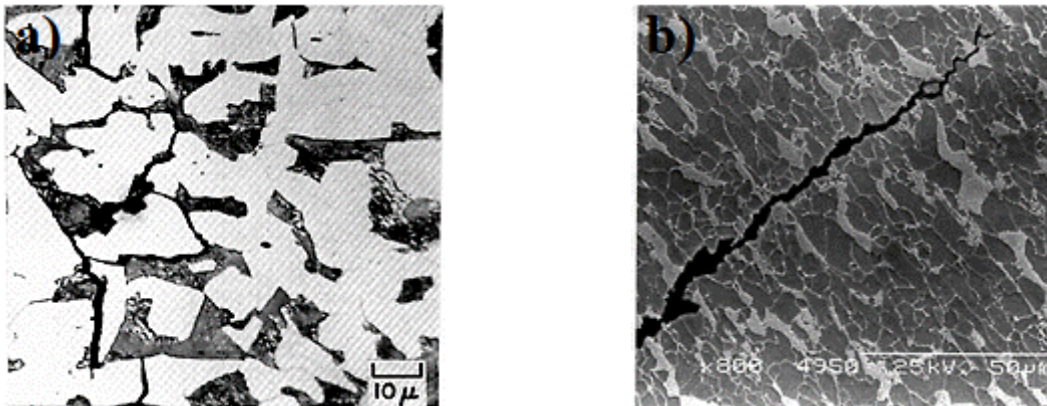


Figure 10.2. (a) Intergranular SCC failure in service; (b) Transgranular SCC in laboratory test with specimen exposed to simulated ground water containing CO_2 , showing lateral corrosion on crack sides [12].

The other type of SCC is when the pH of surrounding solution is 9 or higher because of existence of carbonate. In this pH, the pipe surface become passivated and intergranular corrosion cracks propagate through the grain boundaries [13]. These type of SCC is characterized by some

sharp edges in comparison with TGSCC but both IGSCC and TGSCC are happening in outer surface of pipelines, parallel to the longitudinal axis of pipes [14]. The range of pH for IGSCC and TGSCC are shown in Figure 2.3.

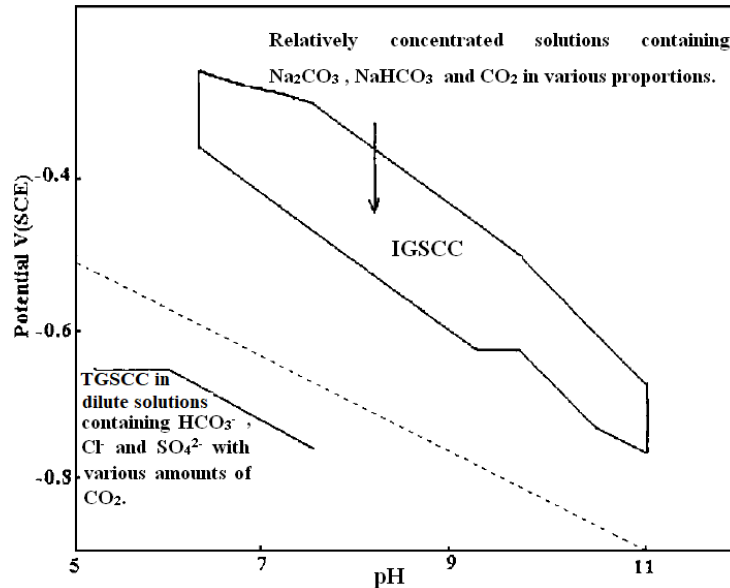


Figure 2.11. Potential-pH diagram showing the regimes for IGSCC and TGSCC at 24° C in solutions containing different amounts of CO_3^{2-} , HCO_3^- , and CO_2 to achieve different pH values [12].

The most common type of SCC that usually happen in the fields is IGSCC. The reason is the cathodic protection of pipeline steels. When the cathodic protection is applied on the pipes, the concentration of hydroxyl ions (OH^-) will be increased in surrounding solution, because of cathodic reactions (O_2 reduction or hydrogen evolution), and the pH of the solution will increase [14–17] which leads to IGSCC.

As it mentioned before, the second factor that affect the SCC are stresses. It can be residual stress or applied stress from inside or outside of the pipelines. The stress concentration profoundly effects the material susceptibility to SCC. It is reported that the original surface of pipeline steels are more susceptible to SCC than polished surface and lower stress in the presence of pits (stress concentration) can easily initiate SCC [22, 23].

Parkins [11, 21] investigated the effects of pressure on the crack initiation of pipeline steels and concluded that the number of cracks depends on the maximum pressure and the type of pressure (Figure 2.4). He reported that a cyclic pressure caused cracking at low pressures regardless of the surrounding solution. A similar conclusion was reported by other researchers [21].

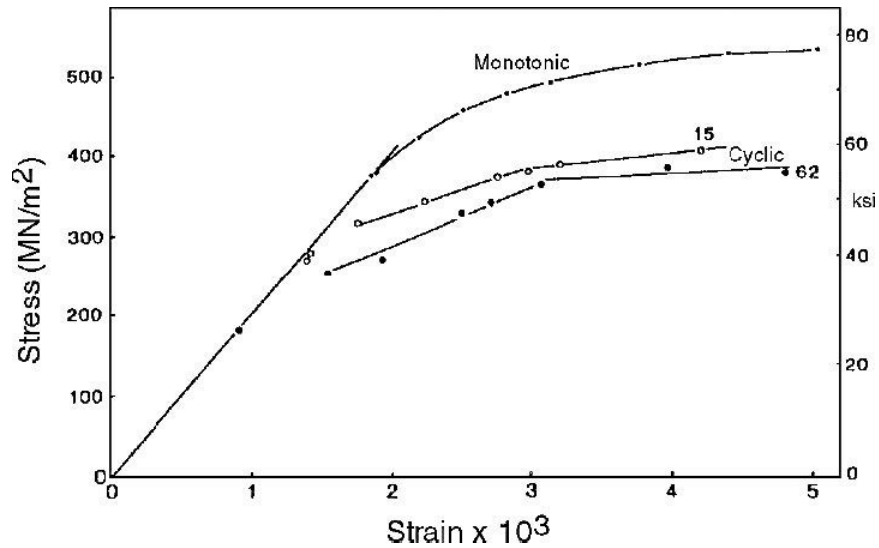


Figure 2.12. Cyclic stress-strain data at 75°C for various fluctuating components of stress (appended to the lines in MN/m²) and the monotonic slow strain rate curves at the same temperature for steel [22].

Some researchers investigated the role of microstructure in SCC susceptibility of steels. According to their reports, ferrite-pearlite structure is more susceptible to SCC than acicular ferrite or fine grained bainitic structures. They also reported that the more homogeneous and uniform structure has higher SCC resistance [34,35]

The effects of acidic environments on SCC resistance of pipeline steels were studied by other researchers [24,25]. According to their findings, brittle fracture occurred in acidic environments and by increasing the acid concentration, the samples became more brittle. They reported that the synergy of SCC and hydrogen induced cracking (HIC) known as stress oriented hydrogen induced cracking (SOHIC) is the main reason of failure in the acidic environments while in the high pH environments, the mechanism of SCC involves anodic dissolution for both crack initiation and propagation [28,13].

Arafin and Szpunar [28] in 2010 used API 5L X65 pipeline steels to predict the intergranular SCC behavior in polycrystalline materials. They made a model according to the Markov Chain theory and used the Monte Carlo simulations in order to predict the intergranular SCC and compare their result with experimental results obtained from EBSD. They reported a good agreement between their model and experiments on crack propagation.

Zhao et al. [29] investigated the role of pipeline steels strength on SCC susceptibility and reported no considerable effect of this parameter on SCC. They also concluded that only the applied stress has significant influence on SCC susceptibility. Lu et al. [30], on the other hand,

reported the inverse relationship between the strength of the pipeline steels and SCC resistance of them.

In 2007, Cheng et al. [31] found that the sulfur environment enhance the SCC susceptibility of X65 pipeline steels by concentrating the hydrogen atoms close to the surface of steel. They also added that existence of sulfide increase the hydrogen permeation into the metal.

Some researchers tried to evaluate the crack propagation path in steels and to find relation between the path and texture and the type of grain boundaries. Arafin et al. [32] found that low angle and special coincident site lattice (CSL) boundaries are crack-resistant while the CSL boundaries beyond R13b and the random high angle boundaries are prone to cracking. They suggested that by engineering the low angle and CSL grain boundaries, it would be possible to improve the intergranular cracking resistance of steels. King et al. [33] reported that the grain boundaries linked with low $\{hkl\}$ index planes are resistant for intergranular SCC.

In conclusion, it seems that the SCC is not a new topic for researchers and almost all aspects of it including the crack initiation and propagation and their relationship with texture and microstructure were investigated.

2.2.2 Sulfide stress cracking (SSC)

As it was mentioned before, one type of HAC failure is sulfide stress cracking (SSC) which is observed in sulfide environments in presence of constant stress that is lower than the yield stress of steel and at room temperature [8]. In this failure mode, the corrosion of steel in sulfide environment produce hydrogen and because of presence of sulfide ions the hydrogen atoms cannot recombined and form hydrogen molecules [36,37]. It causes the concentration of hydrogen atoms on the surface of steel and diffusion of atoms through the steel. This can result in the crack propagation under any stresses that can be residual stress, or applied stress. Scientists made efforts like changing the steel microstructure, changing the chemical composition, controlling the heat treatment process to improve the SSC resistance. They also conducted some tests on steels in the constant load situations for 720 hours, according to NACE TM0177A standard [36] to measure the SSC susceptibility of steels.

Many researchers worked on SSC susceptibility of pipeline steels in sour environments. Al-Mansour et al. [37] investigated the SSC susceptibility of API X100 pipeline steels. They reported that the corrosion pits are the initiation sites of nucleation and propagation of SSC cracks.

They added that these cracks are created perpendicular to the applied stress and the control of non-metallic inclusions is an effective way to improve the SSC resistance (Figure 2.5).

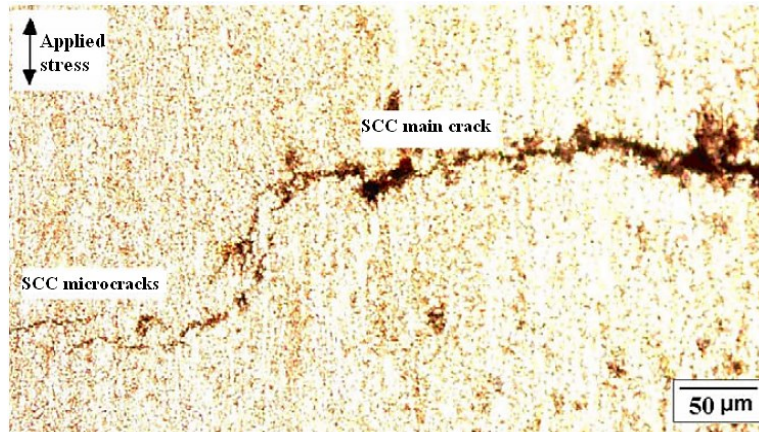


Figure 2.13. Longitudinal section of an X100 specimen loaded at 65%YS showing main SSC crack (right of image) and small micro-cracks (left of image) (light) [37].

Some researchers considered the role of microstructure on SSC susceptibility. Koh et al. [38] showed that acicular ferrite microstructure had the highest resistance to SSC, whereas ferrite-bainitic and coarse ferrite-pearlite microstructures had the lowest resistance. They also concluded that metallurgical parameters such as matrix structure and the defects such as intergranular carbides and inter-lath M/A constituents are more important parameters for controlling SSC in comparison with the hydrogen diffusion rate.

Ume et al. [39] studied the effect of distribution of phases on SSC susceptibility. They also reported that the presence and the shape of oxides like Al_2O_3 and sulfide like MnS inclusions can affect the SSC susceptibility.

In conclusion, many efforts have been made to improve the resistance to SSC and many reports were published, but there is still no solution for this problem.

2.2.3 Hydrogen induced cracking (HIC)

Hydrogen induced cracking is one category of HAC failure mode in which there is no load on pipeline steel. HIC is the most critical mode of cracking in sour environments. The sour environment in oil and gas pipeline steels is when the partial pressure of H_2S gas is more than 0.3 KPa [40]. In this condition, hydrogen atoms from H_2S gas ingress into the steel microstructure and cause the HIC failure of pipeline steels. Moreover, hydrogen is generated as a result of the corrosion of steel surface in the acidic or sour environments. Regardless of the source of generated

hydrogen, corrosion reactions or H_2S gas, existence of hydrogen can cause HIC. On the other hand, the sulfide ions prevent combination of hydrogen molecules and exacerbate diffusion of hydrogen atoms in the steel. According to Barnoush [41], the hydrogen–metal reaction chain before diffusing into the metal consists of three steps: Physisorption, chemisorption and absorption. First, by physisorption van der Waals bonds are generated between the adsorbent and the surface. In chemisorption, the surface atoms and adsorbent atoms make a chemical reaction and, finally, in absorption step, the adsorbent atoms become ready to ingress into the bulk lattice of the metal (Figure 2.6).

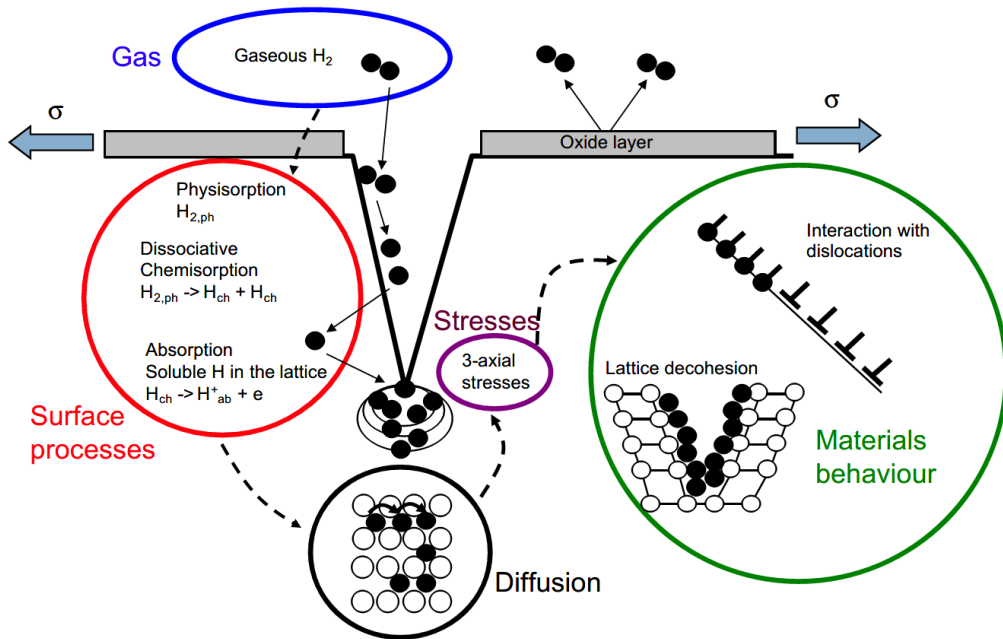


Figure 2.14. Stages of hydrogen material interactions [42].

Several theories have been developed to explain the mechanism of HIC, such as the decohesion model, hydride formation, hydrogen enhanced localized plasticity model and internal pressure theory. Among these theories, the internal pressure theory presented by Zapffe and Sims [43] is the most accepted one [42- 44]. According to this theory, hydrogen atoms that accumulate in traps, such as inclusions and grain boundaries, can combine to create hydrogen molecules. Then, hydrogen molecules can produce the internal pressure and initiate the crack. The cracks will propagate until the failure of the metal [45,46]. The whole reactions between hydrogen sulfide and metal that result in the increase of hydrogen pressure inside the metal are shown in Figure 2.7.

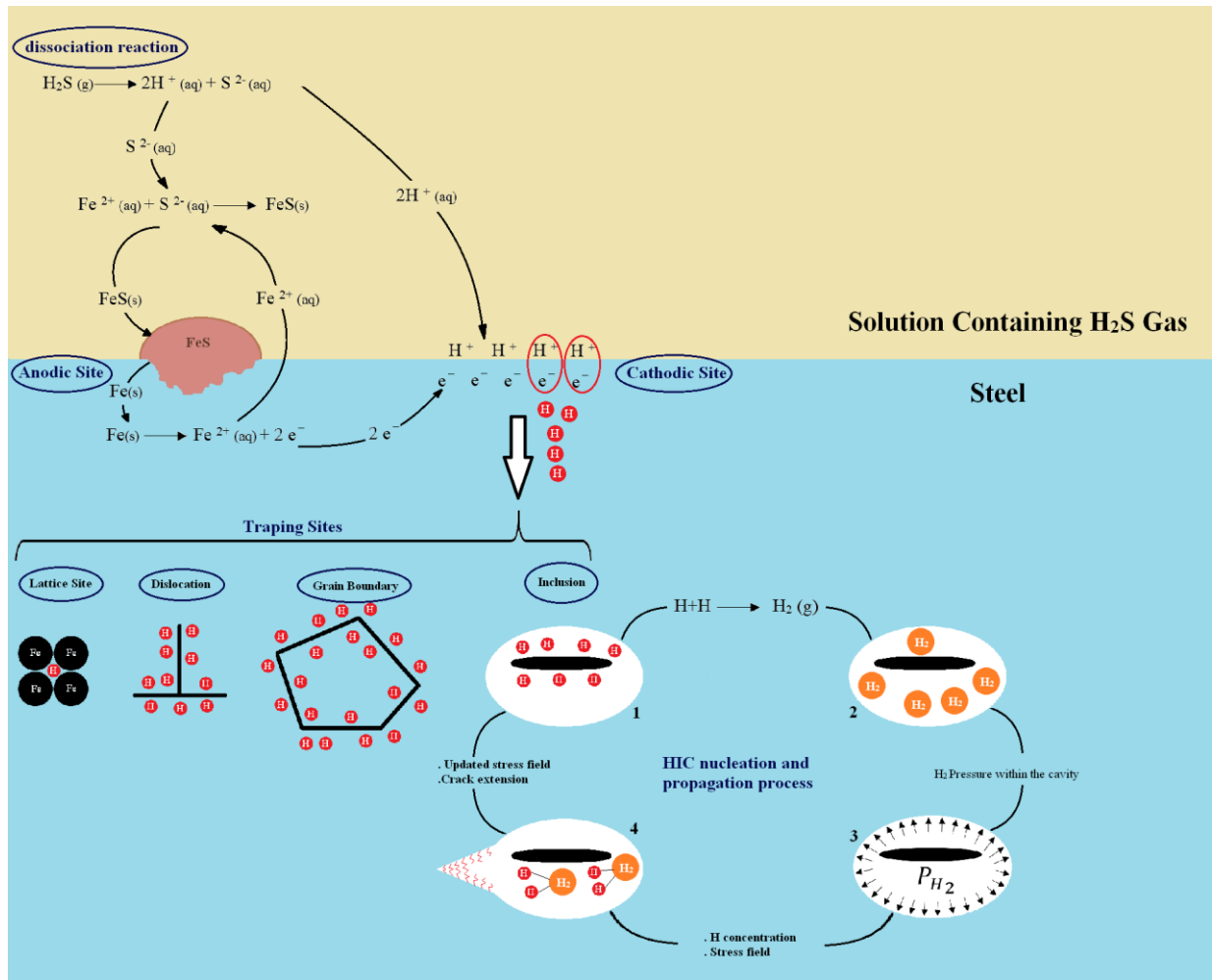


Figure 2.15. HIC mechanism according to internal pressure theory.



According to Figure 2.7 and equations, iron and sulfide ions, formed in anodic and dissociation reactions respectively, react to make the most stable form of themselves, which is FeS (Equation 2.6). On the other hand, H^+ ions from dissociation reaction and electrons from anodic reaction form the hydrogen atoms in the cathodic site, which are absorbed by the metal according to the process described earlier. These atoms accumulate in trapping sites like the space between

inclusions and metal matrix. Then the hydrogen atoms are combined and form the hydrogen molecules. The hydrogen molecules increase the pressure inside the voids produced by traps and cause cracking. Again the hydrogen atoms come to the site and the circular process continues which allows propagation of the crack until the failure of the metal. By diffusing the hydrogen atoms inside the steel, the slip systems will be disrupted. Therefore, hydrogen embrittlement will happen. It is worth-mentioning that hydrogen embrittlement affects also the strength of pipeline steels.

Scientists usually conduct experiments according to National Association of Corrosion Engineers (NACE) TM0284 standard to measure HIC susceptibility of the steels [48]. In this method, the specimen is immersed in synthetic seawater solution, which is saturated with H₂S gas in ambient conditions, or sodium chloride-acetic acid solution. The standard time for putting the sample in the solution is 96 hours and after that, try to find any cracks in the specimen. There is a standard level of cracks, which is the criteria for passing this test by the specimen. According to the NACE MR-0175-2009 standard, there are three levels of resistance to sour environments: MS (mild sour) level, IS (intermediate sour) level and SS (severe sour) level [40].

Some researchers used electrochemical charging of specimen instead of using the H₂S gas because of the safety regulations related to using the H₂S [48–67]. In any case, HIC susceptibility is not function of the sources of hydrogen and is specified according to the amount of hydrogen ingress in the alloy. They used the ISO 17081 standard test to measure the amount of hydrogen permeation, determine the hydrogen uptake and transport in metals by an electrochemical technique [69]. Alloying and microstructural features such as dislocations, grain boundaries, inclusions, and precipitate particles introduce traps for hydrogen atoms, which retard hydrogen transport. Some researchers claimed that the HIC susceptibility of steels directly depends on the amount of the traps in the steel [69,70].

As it was mentioned, there are two types of traps in steels: reversible and irreversible. The hydrogen atoms are released from the reversible traps, such as grain boundaries and dislocations, instantly after hydrogen charging, while the irreversible traps, such as inclusion interfaces, permanently ensnares the hydrogen atoms. Scientists classify traps based on their binding energies with hydrogen, and if the binding energy is higher than 60 kJ.mol⁻¹, it is considered as an irreversible trap [71, 72]. The hydrogen atoms can be released from the irreversible traps if the steel is heated to relatively high temperatures. The higher the binding energy, the higher the release temperature. It is reported by many scientists that the reversible traps are the most important factors

in HIC susceptibility of steels [48, 50, 52, 69, 73–75]. The most common reversible trap sites are dislocations.

In Figure 2.8, a schematic of the permeation testing process is shown. There are two cells, charging and oxidation cells, in this test the sample is a membrane between these cells. The type and amount of solutions used in each cell can be different according to the alloys we are using. For example for stainless steels with Martensitic structure, it is recommended to use 0.1 mol/l NaOH in both cells [69].

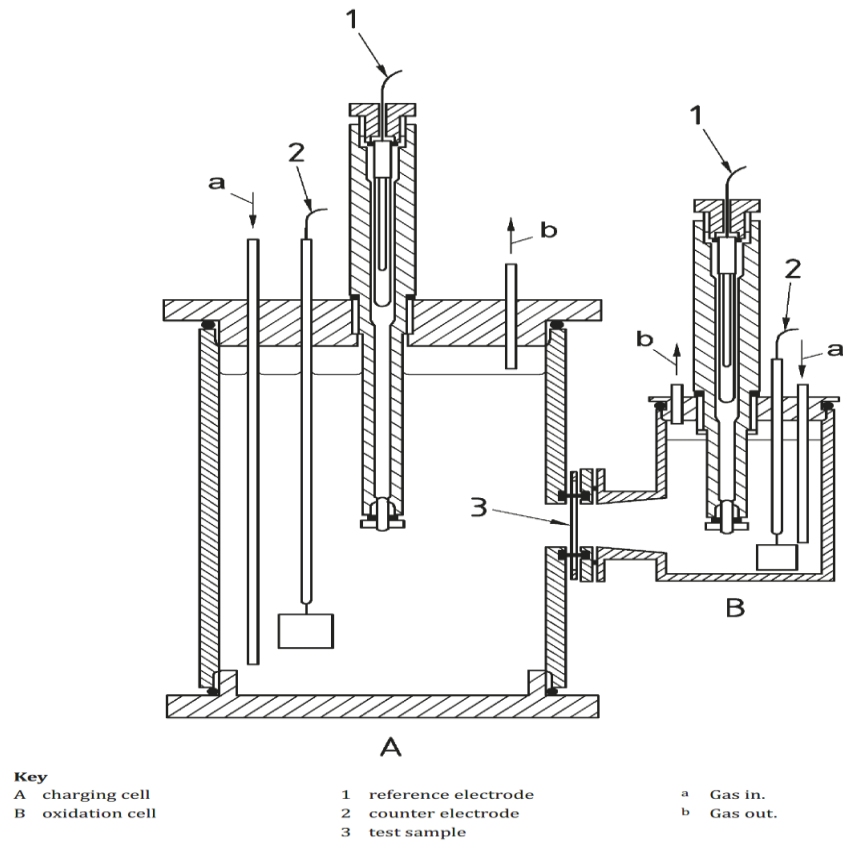


Figure 2.16. Hydrogen permeation cell (constructed of polytetrafluoroethylene) with double junction electrodes [69].

Some researchers used these standards to study the relation between steels' failure and their texture and mechanical properties. Kumar [77] investigated the mechanism of failure in pipeline steels exposed to sour environments. In this study, the X70 pipeline steel samples were electrochemically charged for different durations and then the crack nucleation and propagation sites were examined by performing some characterization tests like EDS, SEM, and OM. HIC cracks nucleated and propagated from regions full of precipitates and inclusions, such as sulfides, silicates, and carbides, and they were found in the center of the sample cross-section. With the Vicker hardening test, he found that the cracked area has a harder phase than the non-cracked area.

Hejazi et al. [78] investigated the role of different inclusions on HIC susceptibility of steels. They considered aluminum oxide, aluminum-calcium-silicon oxide, and elongated manganese sulfide and their effects in their study. They reported that all inclusions decrease HIC resistance of steel and the manganese sulfide is the worst as it decreases the fracture toughness of the steel, too.

Some researchers worked on adding or removing some inclusions to change the nature of traps in steels from reversible to irreversible and control the HIC in this way. For example, researchers have made some efforts to reduce sulfide environments by using calcium treatment. The calcium treatment helps to reduce elongated manganese sulfide (MnS) inclusions. As they said, when sulfur content is <10 ppm and the calcium/sulfur ratio (Ca/S) is >2, the shape of sulfide is completely controlled, and HIC does not occur [79]. Moon et al. [80] reported the same result. In their research, the critical ratio of calcium/sulfur is 1.25. They reported that the CaS inclusions created by adding calcium have a spherical shape and cannot form the stress concentration.

Although most researchers claimed that MnS inclusions are harmful to HIC and the cracks are initiated at those regions, others claimed the opposite. Lee et al. [81] reported that MnS is a strong irreversible trap, while eleven years later, Garet [82] reported completely different results and said that MnS is a reversible trap which is harmful for HIC. The other researcher introduced precipitates like (Nb, Ti)(C,N), which can improve HIC resistance of the steels [83].

Huang [84] worked on the role of cold rolling on trap density and its effect on the HIC susceptibility of AISI 430 sheets. They reported that the cold rolling increases the density of hydrogen traps and caused blistering on the steel's surface. They also analyzed MnS and Al₂O₃ inclusions as the nucleation sites of HIC. Although cold rolling was considered as deteriorating HIC resistance of steel, warm rolling, tempering and quenching decreased the number of traps, and as a result decreased the HIC susceptibility of steel [84–86].

In 2004, Hara et al. [88] tried to find a relation between the amount of H₂S gas and permeability of hydrogen in X65 pipeline steels. They measured the permeability for various combinations of H₂S partial pressure and pH of the solution and associated the permeability with the extent of cracking. They suggested two equations for the permeation of X65 pipeline steels as a function of solution pH and H₂S gas pressure. Kittle et al. [89] reported that in constant H₂S pressure and constant pH solution, the exposure time has a key role in HIC susceptibility of pipeline steels.

Findley et al. [72] tried to establish a standard model for crack initiation and propagation processes. They suggested that as the hydrogen embrittlement susceptibility increases with the strength of pipeline steels and cannot decrease the strength of pipelines steels, we should work on these pipes' microstructural features and inclusions to use larger diameter and smaller thickness in them. Therefore, they considered the effect of thermo-mechanically-processed microstructures on HIC resistance of X52 steel alloys and tried to model it.

Some researchers suggested that the fine and dispersed inclusions as well as second phase particles, increase internal stresses and binding energies. These lead to some irreversible traps in steel, which is beneficial to HIC resistance in steel [89, 90].

Some other researchers evaluated the role of TiC precipitates on hydrogen trapping in steels. They changed the grain size and strength of steels by adding TiC precipitates [49, 73, 91, 92]. All these researchers reported that coherent and semi-coherent TiC precipitates, created depending on tempering conditions, have lower binding energy, and create reversible trap sites in steel. On the other hand, the incoherent TiC sites binding energy is high and make some irreversible trap sites, which is useful in increasing HIC resistance [49, 91].

Moon et al. [94] tried to find the effects of (Nb, Ti, V)(C, N) particles on HIC susceptibility of API X70 pipeline steels. They reported that the crack propagates along coarse (Nb, Ti, V)(C, N) particles at mid-thickness. They claimed that this is because of the hydrogen trapping between these particles and the main matrix.

Wei et al. [94, 95] investigated the role of NbC, TiC, and VC micro alloy particles in steels' hydrogen trapping. They reported that the incoherent TiC particles can trap hydrogen atoms at high temperatures, while coherent and semi-coherent TiC particles have the ability to trap hydrogen at the precipitate/matrix interface at room temperature. They also reported that incoherent NbC and VC particles are unable to trap hydrogen atoms while coherent and semi-coherent NbC and VC particles can trap hydrogen on their interface, depending on their surface area. They compared the trapping capacity of the coherent and semi-coherent type of these three particles and reported this relation for their capacity: $\text{NbC} > \text{TiC} \gg \text{VC}$. Some other researchers reported the same results for the same particles [89, 96].

Nagao et al. [98] investigated the effects of nano size (Ti, Mo)C precipitates on HIC resistance of high-strength tempered lath martensitic steels. They reported that these precipitates provide a high density of hydrogen traps, which improve the hydrogen resistance of steels.

However, when the traps become saturated, the susceptibility of hydrogen embrittlement will return. They also reported that the large size precipitates do not have any effect on hydrogen trapping and the HIC susceptibility of steels. The same results were obtained by Turk et al. [99].

Li et al. [100] considered the role of Vanadium precipitates on hydrogen trapping and HIC. They reported that as the vanadium precipitates increase, the trapped hydrogen increase. They also found that the hydrogen diffusion coefficient decreased from $4.74 \times 10^{-6} \text{ Cm}^2.\text{S}^{-1}$ in the vanadium-free steel to $8.48 \times 10^{-7} \text{ Cm}^2.\text{S}^{-1}$ in the steel with 0.16% Vanadium. They got that the 0.12% V in the steels, which has the largest amount of small (less than 60 nm) vanadium carbide particles, has the lowest HIC susceptibility.

Some researchers tried to decrease HIC susceptibility by changing the manufacturing process of steels. They tended to decrease the plastic deformation of steel to decrease the number of dislocations, representing reversible trapping of hydrogen. Ogibayashi et al. [101] attempted to decrease steels' HIC susceptibility by optimizing the reduction process. They suggested that by soft reduction and reduction with the divided rolls, improving the center segregation of slab in low carbon and low manganese steels is possible. This improvement is related to a significant decrease in manganese and phosphorus segregation due to the optimum reduction.

Some researchers investigated the effects of grain size on hydrogen permeation and diffusion. They found that the susceptibility to hydrogen embrittlement can increase by increasing the grain size, and the coefficient of hydrogen diffusion decrease as the steel hardness increase [101, 102]. Takasawa et al. [104] related the role of grain size to the hydrogen pressure and reported that the grain refinement reduces the hydrogen embrittlement in high hydrogen pressure (around 45 MPa).

2.3 Effects of microstructure on HIC susceptibility

The microstructure of pipeline steels used in the oil and gas industry mostly consists of ferrite morphologies such as acicular and granular ferrite and some pearlite, and small amounts of microconstituents like micro-alloy precipitates and austenite/martensite (M-A) islands [2, 3]. Scientists use microalloying and thermomechanical processing to refine grains, modify the structure of precipitates, and remove large carbides to reach the stronger structure. In this way, the resistance to HIC will be modified, as generally with increasing strength, the hydrogen embrittlement susceptibility will increase. There are some efforts done to compensate for the HIC

susceptibility of pipeline steels. Most of them use one technique like desulphurization, inclusion control, microalloying, microstructure engineering, and crystallographic texture control [4, 5].

In 2008, Park et al. [109] created three different microstructures of API X65 pipeline steel by controlling the start cooling temperature (SCT) and the finish cooling temperature (FCT) in the thermo-mechanically controlled process (TMCP). They reported significant changes in both hydrogen trapping and hydrogen diffusion by changing the microstructure. They found that Ferrite/degenerated pearlite (F/DP), ferrite/acicular ferrite (F/AF), and ferrite/bainite (F/B) are the microstructures that trap hydrogen effectively, respectively. They also reported that HIC is initiated at the local martensite/austenite (M/A) microstructure, and bainite is the most sensitive microstructure to HIC, among others.

The same conclusion can be found in Beidokhti et al. [110] research paper. They reported that the acicular ferrite (more than 60%) decrease the HSLA steels susceptibility to HIC and contrary presence of the martensite and bainite structures makes steel highly susceptible to HIC. They also reported that changing the inclusion type from manganese-base to titanium-based makes the steel more resistant to HIC.

Ohaeri et al. [111] reported the same results. They claimed the mid thickness layer is more resistant to hydrogen assisted failure than the surface thickness layer. The reason is that the surface layer has higher strength and lower ductility. The mid-thickness microstructure is mostly acicular ferrite, while the top surface is dominated by bainitic-acicular ferrite. They also investigated the crystallographic orientation of grains, which were approximated by $\{111\}$ and $\{110\}$ texture fibers (specifically $\{123\}$) at the mid thickness, and mostly $\{001\}$ textured grains (specifically $\{013\}$) at top thickness layers.

Mohtadi-Bonab et al. [59] electrochemically charged API X60 and API X60SS pipeline steels and used electron backscatter diffraction (EBSD) to analyze the specimens. They reported different results than Ohaeri. They suggested that the HIC happened in the specimens' middle surface and propagate through $\{100\}$ grains in various directions. They also found that the high fraction of recrystallized microstructure in X60SS steel is led to lower stored elastic energy and higher resistance to HIC in comparison to API X60 steel.

Some others researchers suggested to increase the cooling rate after hot rolling in order to gain uniform microstructure. This can cause uniform distribution of carbon in all regions of steel

as well as reduction of hardening in center segregation region, resulting in the dispersing of the second phase finely [112].

Masoumi et al. [113] investigated the role of crystallographic texture on HIC resistance. They found that $\{110\}$ grains and a small number of $\{001\}$ grains both parallel to the normal direction improved the HIC resistance while $\{001\}$ grains parallel to normal direction were highly susceptible to cracking. They suggested that it is possible to change the HIC susceptibility just with controlling the texture. In another research, Verdeja et al. [114] showed that $\{332\}$ texture increased the resistance of steels to HIC.

Based on the aforementioned points, it seems that TMCP is the most effective technique to gain optimum HIC properties in pipeline steels [115]. With TMCP it is possible to change the texture and grains orientation to reach $\{111\}$ texture which has been suggested to be the best orientation in sour environments [52]. Some researchers suggested warm rolling in order to obtain $\{111\}$ texture in steels [116]. On the other hand, in addition to the type of texture the type of grain boundaries are important to prevent crack propagation too. Arafin and Szpunar [32] reported that low angle grain boundaries (LAGB) and coincident site lattice (CSL) especially with low sigma like $\Sigma 13b$, $\Sigma 11$ and $\Sigma 5$ have lower energy and are resistant to intergranular crack propagation. The same results were obtained by other researchers [111, 115, 116]. They reported that there is a concentration of CSL and low angle grain boundaries around $\{111\}$ grains.

There were many efforts to improve HIC resistance of steels and the results obtained were often contradictory. Very few researchers considered the effect of different TMCP parameters such as timing and annealing and normalizing temperature on HIC susceptibility of pipeline steels to the best of found knowledge. The effect of the service temperature on HIC susceptibility of pipeline steels is also unknown, as they are often being used in negative temperatures especially in Canada. There are still many unexplored opportunities to improve the pipeline steel performance.

CHAPTER 3: MATERIAL AND EXPERIMENTAL PROCEDURE

3.1 Overview

This chapter describes the supplied materials and the experimental procedure used in the thesis. Three different samples with detail of their chemical composition are presented in the material section. In the experimental procedure, all tests used in this study contain hydrogen charging of samples, hydrogen permeation test, mechanical tests, phase, texture, and microstructural characterization methods are explained, followed by the sample preparation for each test.

3.2 Material

This study focused on API 5L X70 pipeline steels produced by EVRAZ Company in Regina. The first batch of pipeline steels, n

amed as X70-1 in this study, was received in 2016 and used by other researchers in the laboratory. The second and third batches were received in 2019 and were sent specifically for this research. The second batch, named as X70-2, has more Ni in comparison with others, while the last batch, X70-3, has more Cr. The chemical composition of the samples are presented in Table 3.1.

Table 3.1. Chemical composition of API 5L X70 pipeline steel samples (Wt.%).

Pipe	C	Si	Mn	P	S	V	Nb	Al	Cr	Ni	Cu	Mo	Sn	Ca	Ti	N	O
X70-1	0.047	0.8	1.65	0.009	0.0018	0.001	-	0.044	0.06	0.07	0.29	0.247	0.01	0.0014	0.022	0.01	0.003
X70-2	0.054	0.25	1.61	0.012	0.0017	0.004	0.081	0.046	0.09	0.45	0.25	0.174	-	-	0.014	0.007	-
X70-3	0.043	0.28	1.35	0.013	0.003	0.004	0.09	0.036	0.24	0.1	0.29	0.23	-	-	0.016	0.006	-

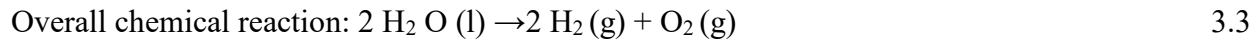
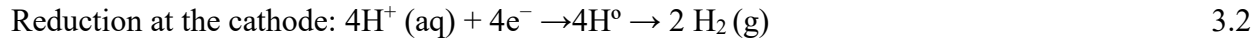
3.3 Experimental procedure

Different experiments, including hydrogen permeation, HIC, and mechanical testing, were conducted in this study. The methods of each test, the sample preparation and characterization methods are explained in this section.

3.3.1 HIC testing

The pipeline steels are usually used in sour environments, which cause HIC. The samples were electrochemically charged with hydrogen to simulate the sour environment. In this regard,

the samples were the cathode and a constant current density of 20 mA/cm² was applied with an Instek DC power supplier throughout the hydrogen-charging period (Figure 3.1). The following reactions occurred during hydrogen charging to produce hydrogen:



According to the NACE TM 0284-2016 standard, this test was performed to evaluate the HIC resistance of specimens. The solution contained 0.2 M sulfuric acid (H₂SO₄) and 3 g/l ammonium thiocyanate (NH₄SCN). The ammonium thiocyanate was added to promote hydrogen ingress into the metals by preventing the formation of hydrogen molecules.

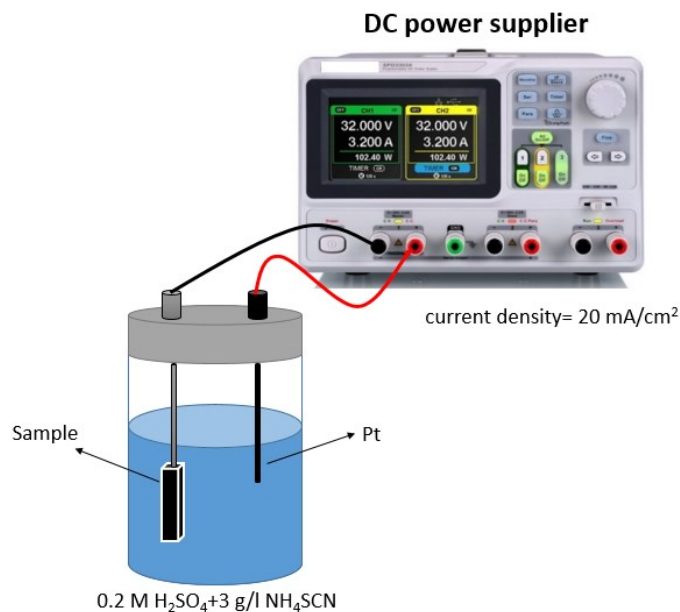


Figure 3.1. Schematic of hydrogen charging of samples.

3.3.1.1 Sample preparation for HIC testing

All experiments were done on specimens in the middle and the top layers of the plates for investigating the HIC behaviour of different regions with different microstructure texture and inclusions segregation in pipeline steels. In this regard, long strips from each sample's top and middle layers were prepared using the CNC machine (Figure 3.2). Then cubic samples from each layer were cut using Buehler 95-C1800 abrasive cutter.

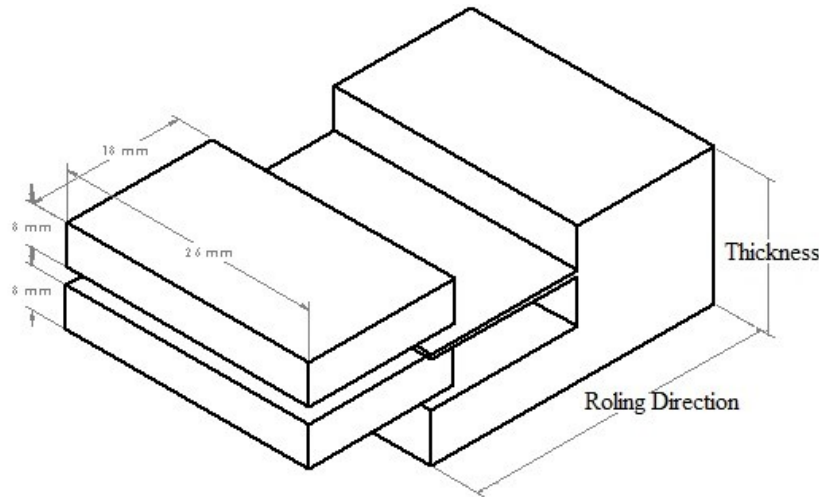


Figure 3.2. Schematic of top and middle layers prepared from the bulk rectangular plate.

All samples are polished before HIC testing with SiC papers started from 180 grit paper followed by 320, 500, 800, 1000, 1200, 2400, and 4000 grits using Struers, Labopol-5 automatic polishing machine to have a smooth and even surface.

3.3.2 Permeation testing

The permeation testing is used according to the ISO 17081 standard testing [69] to see the type of traps inside the samples (reversible or irreversible) and the amount of hydrogen absorbed and permeated through them.

The permeation testing was first utilized by Devanathan and Stachurski at the University of Pennsylvania to calculate hydrogen permeation through a palladium membrane [119]. The test setup used in this research is the same as what they did with a little modification to obtain more repeatable results. This setup contains two identical glass beakers that have a flange on their bottom. One beaker acts as the charging cell where the hydrogen production occurs while the other beaker acts as the oxidation cell, and the diffused hydrogen is oxidized there. The charging cell contains 250 ml of 0.1 molar sulfuric acid (H_2SO_4) with 3 grams per litre of ammonium thiocyanate as the hydrogen recombination poison. In contrast, the oxidation cell contains 250 ml sodium hydroxide (NaOH) acts as the electrolyte (Figure 3.3). On each cell's lid, a 5 mm diameter graphite rod is placed to act as the counter electrode. One other hole embedded on the oxidation cell lid to place saturated calomel with three molar potassium chloride acts as the reference electrode. To deaerating the cells from oxygen, the inert argon gas is used during the entire testing period. For this reason, two holes are embedded on each lid for inhaling and exhaling the argon gas. Two

beakers are connected through their bottom flanges. The sample is placed in the gap between the two flanges. One square centimetre area rubber O-ring is used in each flange to avoid any leakage through the flanges and provide an equal exposed area on both sides of the sample. To fasten two beakers, a nylon fastening belt as used around both beakers.

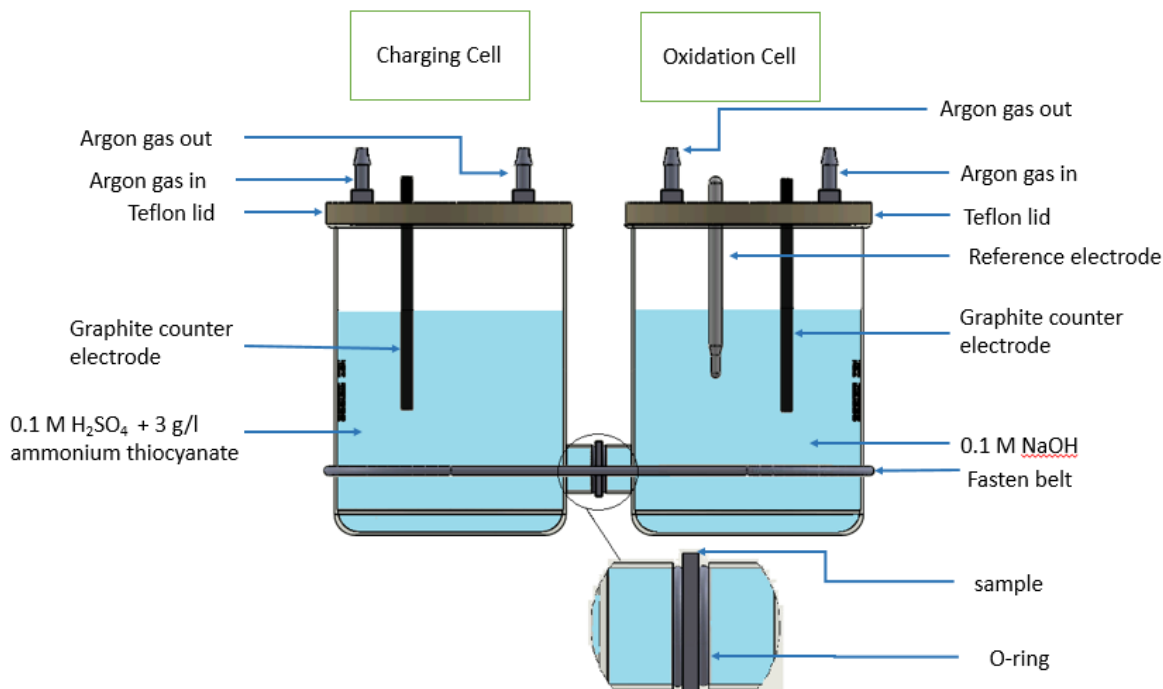


Figure 3.3. Assembly of permeation testing.

The wire connections of this test are shown in Figure 3.4. The counter electrode in the charging cell was connected to the positive pole of the DC power supplier while the sample is connected to the negative pole and acts as the cathode, where the hydrogen generation occurs. The reference electrode, counter electrode, and the sample were connected to Gamry G750 potentiostat in the oxidation cell and created the second electrochemical cell, where the diffused hydrogen is oxidized.

The DC power supplier provided 5 mA current in the system, which was used for hydrogen production. In the oxidation cell, the Gamry potentiostat provided 250 mV constant potential between the sample and reference electrode to oxidize the hydrogen atoms diffused through the sample. When both cells worked, the oxidation cell side of the sample acted as the anode, and the charging cell side of the sample acted as the cathode. The Gamry software recorded the current flowing through the counter electrode, which shows the amount of oxidized hydrogen.

Before applying the current, the test assembly was set up. It took about four hours that the residual hydrogen in the oxidation cell electrolyte became oxidized, and the Gamry recorder showed the oxidation current less than 200 nA. In this stage, the 5 mA current was applied to the charging cell, and the hydrogen generation was begun around the sample. The generated hydrogen diffused through the sample and oxidizes in the other cell. This provided the oxidation current, which was recorded by Gamry software on the computer.

After about three hours, the current became stable, and at this point, the current of the power supplier was turned off. The oxidation current gradually reduced after turning off the current. This process took about 4 to 5 hours that all diffused hydrogen atoms in the oxidation cell became oxidized, and the oxidation current, shown by Gamry software, becomes close to the zero again. However, some hydrogen atoms were still stuck in the traps inside the sample (irreversible traps) after this stage.

The same process was repeated to evaluate the amount of reversible and irreversible trap sites inside the sample. It is worth mentioning that to avoid corrosion of the sample in the charging cell when there is no need to apply the current in this cell; the acidic electrolyte was emptied.

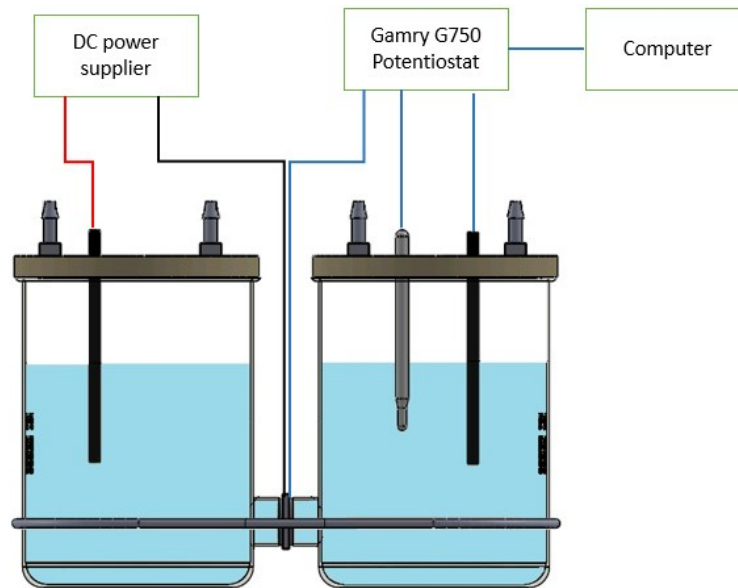


Figure 3.4. Permeation test wire connections.

The typical result which was obtained by this experiment looks like Figure 3.5. There is some information in this curve, like the steady-state current (I_{∞}) and time lag (T_L), which help to calculate other desired parameters.

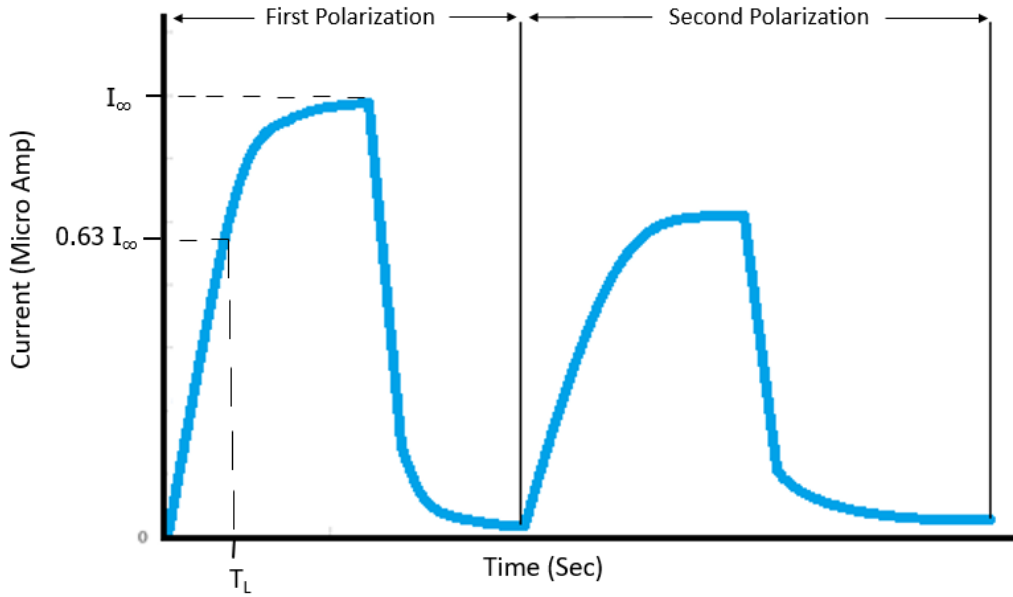


Figure 3.5. Typical hydrogen permeation result after two polarizations.

The equations for calculating the permeability coefficient ($J_{\infty}L$), effective diffusivity (D_{eff}), apparent solubility (C_{app}), and the total number of hydrogen-trapping sites (N_T) are as below:

$$J_{\infty}L = \frac{I_{\infty}L}{FA} \quad 3.4$$

$$D_{eff} = \frac{L^2}{6t_L} \quad 3.5$$

$$C_{app} = \frac{J_{\infty}L}{D_{eff}} \quad 3.6$$

$$N_T = \frac{C_{app}}{3} \left(\frac{D_L}{D_{eff}} - 1 \right) \quad 3.7$$

where, I_{∞} (μA), L (cm), A (cm^2), F (C/mole), T_L (s), and D_L ($cm^2 s^{-1}$) are steady-state current, the thickness of the steel membrane, area of the specimen subjected to charging and oxidation cells, Faraday's constant, time lag, and lattice diffusion coefficient, respectively. The steady-state current will be found from the curves (Figure 3.5), and time lag is the elapsed charging time when the proportion of $J(t)/I_{\infty}$ is equal to 0.63. The lattice diffusion coefficient and Faraday's constant are equal to $1.28 \times 10^{-4} \left(\frac{cm^2}{s} \right)$ and $96500 \left(\frac{C}{mol} \right)$, respectively.

In this test, the sample was charged twice. In the first charging, both reversible and irreversible traps were filled with hydrogen atoms. After stopping the power supply current, the hydrogen atoms that were captured in reversible traps discharged. Again, the same current was

applied, and the oxidation current was measured. The amount of reversible hydrogen trap sites was calculated using the second oxidation current. From the difference between the first and second oxidation current, the amount of irreversible trap sites was calculated. The amount of discharged hydrogen in the oxidation side was estimated by calculating the area below the hydrogen permeation current curve in the discharging section.

3.3.2.1 Sample preparation for hydrogen permeation testing

To prepare the samples for the HP test, the samples were first cut in $25 \times 20 \times 2 \text{ mm}^3$ from both the middle and top layers of each steel plate. After cutting, both surfaces of the specimens were ground with SiC papers from 180 to 4000 grits. The samples were polished with diamond paste to eliminate the flux-limiting surface impedances and having a smoother surface (less than $1 \mu\text{m}$). The final thickness of the samples was around 1 mm. The specimens were coated with 20 nm thickness of palladium on either side to decrease the surface corrosion and increase the hydrogen oxidation rates.

3.3.3 Mechanical testing

The mechanical testing used in this research consists of tensile testing and hardness testing. In this section, the method of each experiment is explained briefly.

3.3.3.1 Tensile testing

The tensile testing was used in this research to compare the strength of pipeline steels in different service environments, including sour and acidic environments, as well as atmospheric conditions. This test was just conducted on X70-1 samples. The strength of other samples were tested by the company and the effect of different service conditions on them were not evaluated in this research.

To simulate the acidic environment, one molar hydrochloric acid (HCl) solution was used, and then the samples were immersed in the solution for 24 hours. After that, tensile testing was carried out. To simulate the sour environment, the HIC testing, which was explained in the previous section, was conducted inside the tensile testing machine tank to see the in-situ effect of that environment on the tensile strength of steels. The other test was performed on X70-1 pipeline steels to measure the ex-situ effects of sour environments on the strength of pipeline steels. In this regard, the samples were charged according to what was explained in the HIC testing procedure. Then tensile testing was conducted to measure the tensile strength of steels after exposure to the

sour environments. The last test was the combination of the previous two tests. In this test, the sample was charged for 24 hours, followed by conducting the tensile testing in-situ.

The machine designed by Mostafijur Rahman was used in this research (Figure 3.6). This machine has this ability to conduct tensile testing with different strain rates. The slow strain rate testing (SSRT) with an elongation rate of 1.7615×10^{-6} (sec^{-1}) was used to obtain the stress-strain diagram for all samples.

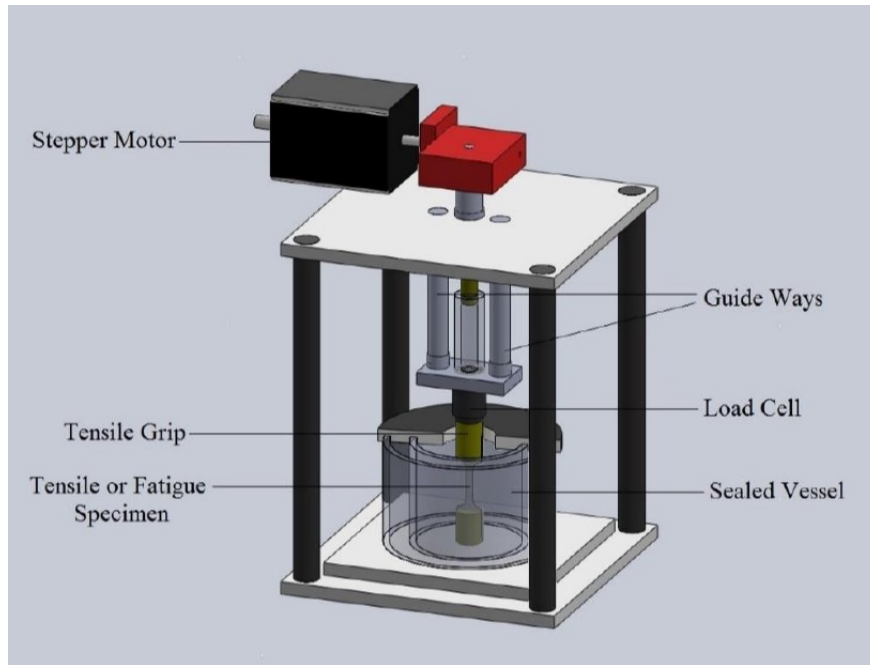


Figure 3.6. Tensile testing equipment [120].

3.3.3.1.1 Tensile testing sample preparation

All testing process and sample dimensions (Figure 3.7) are according to the ASTM E8 standard [121]. The dog-bone shape specimens were prepared in the machine shop of the engineering college using the CNC machine. After shaping the samples, SiC papers from 320 to 2400 grits were used to make a smoother surface for the samples and avoid stress concentration and remove corrosion sites.

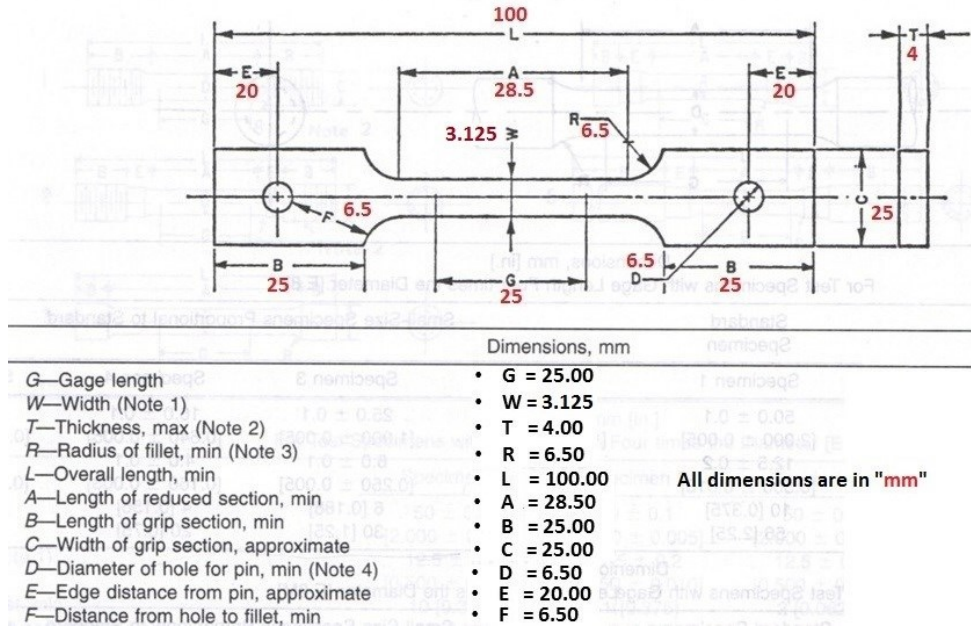


Figure 3.7. The dimensions of tensile test samples.

3.3.3.2 Hardness testing

As was mentioned in the literature review chapter, many researchers believe that hydrogen diffusion increases the hardness of steel. On the other side, harder materials have lower resistance to HIC. For these reasons, knowing the hardness of each sample before and after the HIC test help to understand the role of the sample's hardness on HIC cracking, and also it's a way to compare the behaviour of different samples with different TMCP parameters and chemical compositions to the HIC. In this study, MVK-H1 Mitutoyo hardness tester is used with 1 kg load for 12 seconds, and the Vickers scale (HV) is reported for all samples. This test is according to ASTM E384-17 standard test [122] and conducted five times for each sample, and the average value is reported for each sample. For performing this test, the surface of all samples is polished with SiC papers from 180 to 4000 grits. To do hardness testing for the samples exposed to the hydrogen charging, they are quickly removed from the charging set-up and do testing immediately to minimize the desorption of hydrogen from the steel.

3.3.4 Thermo-Mechanical Control Processing (TMCP) of the samples

As was mentioned in the mechanical testing section, the X70-1 specimens are used to evaluate the effect of different conditions on mechanical properties and their HIC resistance. The X70-2 and X70-3 samples are used to study the effects of varying TMCP parameters on their

resistance to HIC. In this regard, two different TMCP parameters are utilized in each sample, which is presented in Table 3.2 and Figure 3.8.

Table 3.2. TMCP parameters of X70-2 and X70-3 specimens.

Pipe	#	Reheat (C)	Charge time	Roughing Passes	Rough Time (m:s)	Last Pass Temp (C)	Hold (min)	Finish rolling entry Temp (F)	Finishing Passes	Finish Time	Exit Temp (C)	Cooling temp (C)	Cooling Rate (C/S)
X70-2	1	1247	07:07	8	03:50	1016	4	892	5	03:17	780	563	30.8
	2	1282	07:02	5	01:56	1114	6	880	7	03:42	855	536	62.5
X70-3	1	1192	04:22	6	06:13	977	5	876	7	04:16	786	509	34.2
	2	1192	05:27	6	04:40	1002	6	886	5	03:26	816	513	26.9

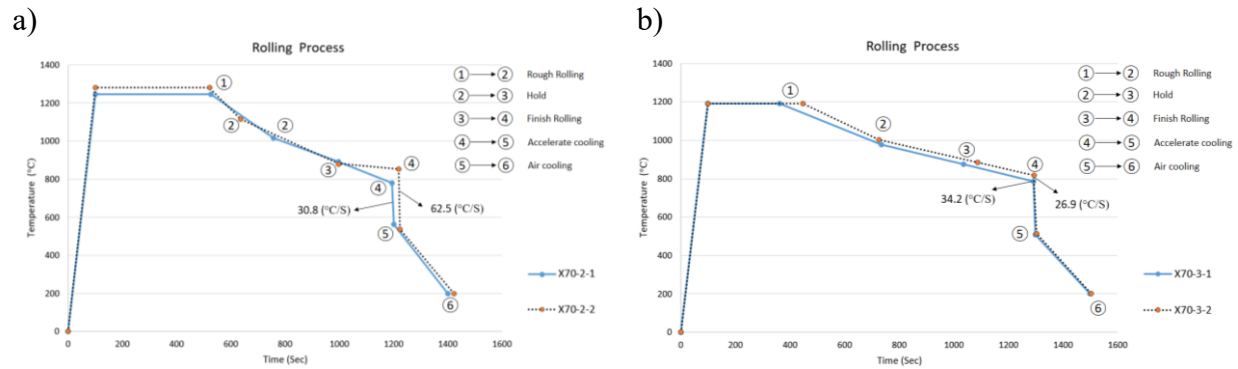


Figure 3.8. Schematic diagram of the rolling process for a) X70-2 and b) X70-3 steels.

The table indicates different temperatures at which various treatment stages are conducted, and the figures schematically show the rolling process of both samples. As shown in the pictures, the whole rolling process is about 1400 seconds for X70-2 samples, while it is about 1500 seconds for X70-3 samples. There are three bold differences in TMCP of X70-2 samples. In the X70-2-1 specimen, the reheating temperature is 35°C less than X70-2-2, and rough rolling is conducted in 8 steps, while there are just 5 roughing passes in the X70-2-2 specimen. On the other hand, the finish rolling is conducted in 5 and 7 passes for X70-2-1 and X70-2-2 samples. The other difference is the cooling rate of the samples, which is almost twice in the X70-2-2 specimen, 62.5 versus 30.8 °C/s. The detail of rolling passes is presented in Table 3.3.

Table 3.3. The rolling pass reductions in the specimens.

Sample	Roughing Passes	Total Roughing Reduction (%)	Pass 1 (%)	Pass 2 (%)	Pass 3 (%)	Pass 4 (%)	Pass 5 (%)	Pass 6 (%)	Pass 7 (%)	Pass 8 (%)
X70-2-1	8	77.1	11.7	13.2	14.2	15.7	17.1	18.4	20	23
X70-2-2	5	62.5	13.1	15.8	18.5	21.4	24.5	-	-	-
X70-3-1	6	69.8	13.3	15.1	17.1	19	21	25.2	-	-
X70-3-2	6	69.9	13.3	15.1	17	18.8	20.7	25	-	-

Sample	Finishing Passes	Finishing Mill Reduction (%)	Pass 1 (%)	Pass 2 (%)	Pass 3 (%)	Pass 4 (%)	Pass 5 (%)	Pass 6 (%)	Pass 7 (%)
X70-2-1	5	67.2%	20.1	20.2	20.2	19.1	19.2	-	-
X70-2-2	7	75.7%	19.5	17.4	19.8	21	17.6	14.5	13.2
X70-3-1	7	74.9%	15.2	15	16.2	17.5	18.9	19.8	21.6
X70-3-2	5	74.5%	25.2	25.6	24.7	21.7	22.3	-	-

In the X70-3 samples, there are two bold differences in their TMPCs. In the X70-3-1 specimen, there is 7 finish rolling while this number is 5 for X70-3-2. Another difference is their cooling rate, which is 34.2 and 26.9 for X70-3-1 and X70-3-2, respectively. It is worth mentioning that the final reduction of all four samples after both rolling is about 92%.

3.3.5 Microstructural evaluation

By using the Nikon Eclipse MA100 Optical Microscope (OM) and SU6600 Hitachi scanning electron microscope (SEM) equipped with Energy Dispersive Detector (EDS), the study of microstructure, the fracture surface and elemental analysis are done, and the metallographic images are collected. To prepare the samples, they are first hot mounted, followed by polishing with SiC papers (180, 320, 500, 800, 1000, 1200, 2400 and 4000 grits). Then they are finely ground using 3 μm MD-Dac and 1 μm MD-Nap provided by Struers. The etching is done using the standard 2% Nital (2 vol% nitric acid and 98vol% alcohol) solution for about 15 seconds.

3.3.6 Phase identification

SU 6600 Hitachi field emission SEM equipped with an Oxford Instruments Nordlys Nano EBSD detector is used to identify the phase and texture of all specimens across their thickness. To prepare the samples for phase and texture evaluation, all explained steps in the previous section

are done, followed by using the Buehler VibroMet 2 vibratory polisher with Master Met 2 polishing suspension for final polishing. The EBSD machine gives more information about the phase distribution, grain boundary distribution, grain size, the inverse pole figure, the misorientation, and the recrystallization fraction of the samples used to analyze and compare the samples.

CHAPTER 4: RESULTS AND DISCUSSION

In this chapter, the results obtained from experimental investigations are presented. These test results include microstructure and texture characterization of all samples before and after hydrogen charging, mechanical testing results, and hydrogen permeation (HP). A brief discussion of each test result is provided in each section. The relationships between all obtained results, the texture, and TMCP parameters are discussed at the end of the chapter in the results analysis section. This section is followed by examining the hydrogen effects on the crack initiation, propagation and the role of microstructure in HIC.

4.1 Microstructure evaluation of as-received samples

The microstructure of all samples is evaluated in both middle and top layers using OM and SEM. Figure 4.1 shows the microstructure of X70-1 samples at the center and top layers, respectively.

The microstructure of both middle and top layers of the X70-1 sample mostly consisted of polygonal and acicular ferrite (flat light regions) and tiny amounts of pearlite (darker regions) around the ferrite boundaries. This microstructure is due to the small amount of carbon in the samples' chemical composition and the thermo-mechanical processing of pipelines with a low cooling rate. It also seems that regions with ferrite regions are more co-axial in the middle layer.

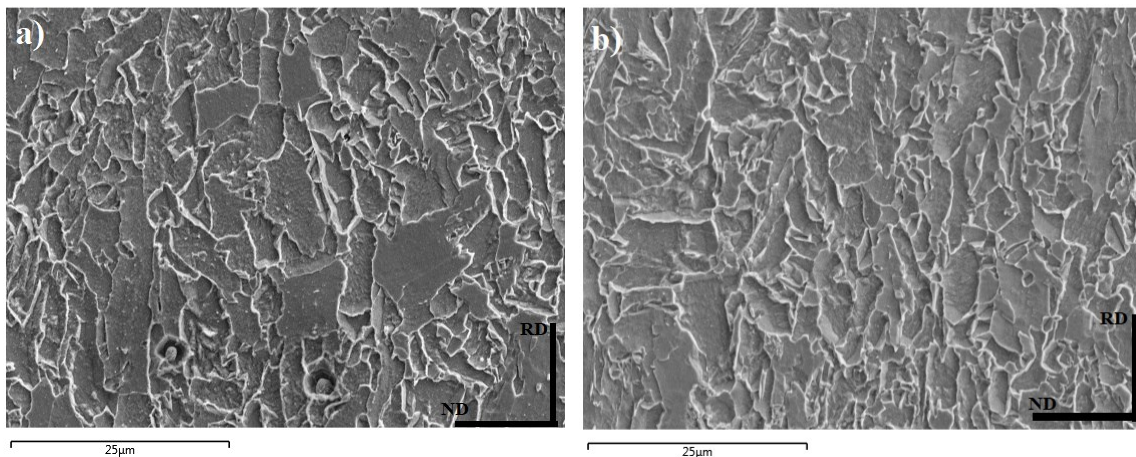


Figure 4.1. Micro structure of X70-1 sample at a) middle b) top layers.

The microstructure of X70-2-1, X70-2-2, X70-3-1, and X70-3-2 steels with different TMCP parameters are presented in Figures 4.2 and 4.3 for both top and middle layers, respectively.

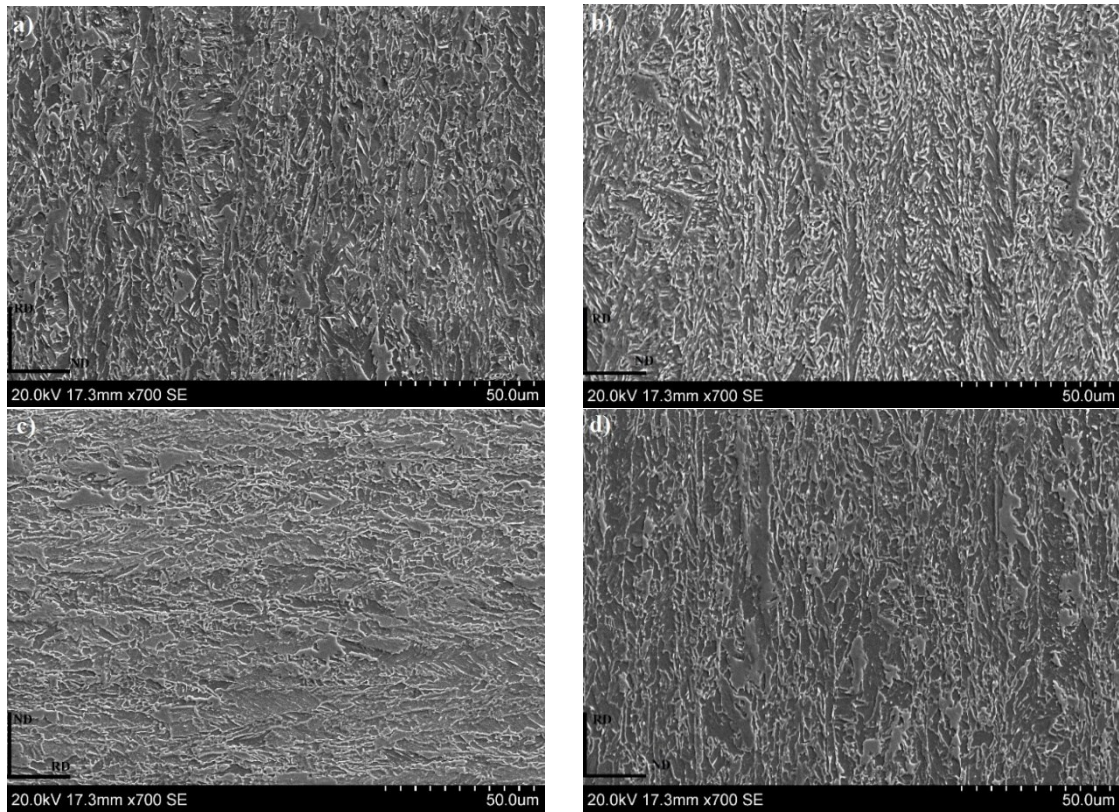


Figure 4.2. Microstructure of a) X70-2-1, b) X70-2-2, c) X70-3-1, d) X70-3-2 samples at middle layer.

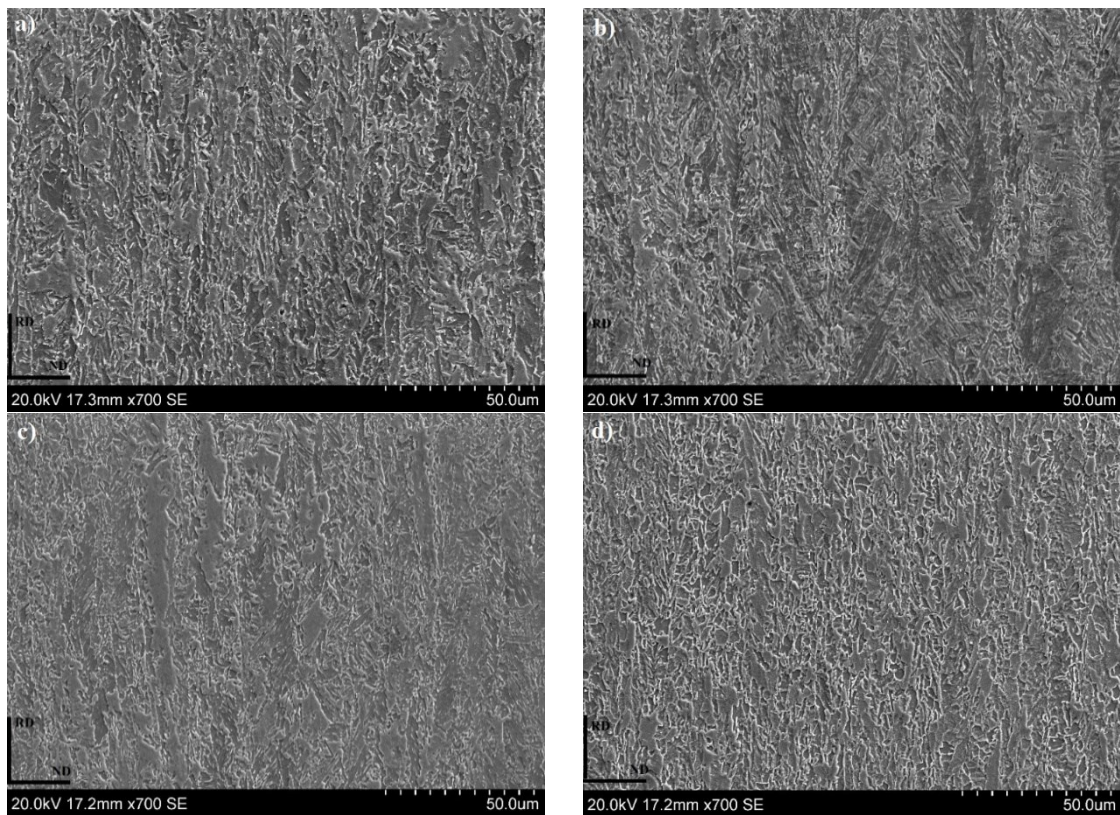


Figure 4.3. Microstructure of a) X70-2-1, b) X70-2-2, c) X70-3-1, d) X70-3-2 samples at top layer.

As shown in the figures, the microstructure of the specimens, except X70-2-2, mostly consisted of polygonal and acicular ferrite and very small amounts of pearlite, same as X70-1 samples. Some martensite can be distinguished in X70-2-2, and the reason is the higher cooling rate in this specimen (62.5 C/s) while in the other specimens, this number is between 26.9 and 34.2 C/s. The other difference between these photos is different grain size, which is measured in the next part.

The grain size of the samples is calculated using the EBSD machine. The grain size distribution maps of all samples are presented in Figures 4.4 and 4.5. These maps are created according to the circle equivalent diameter of the grains, and high angle grain boundaries (15°) are considered.

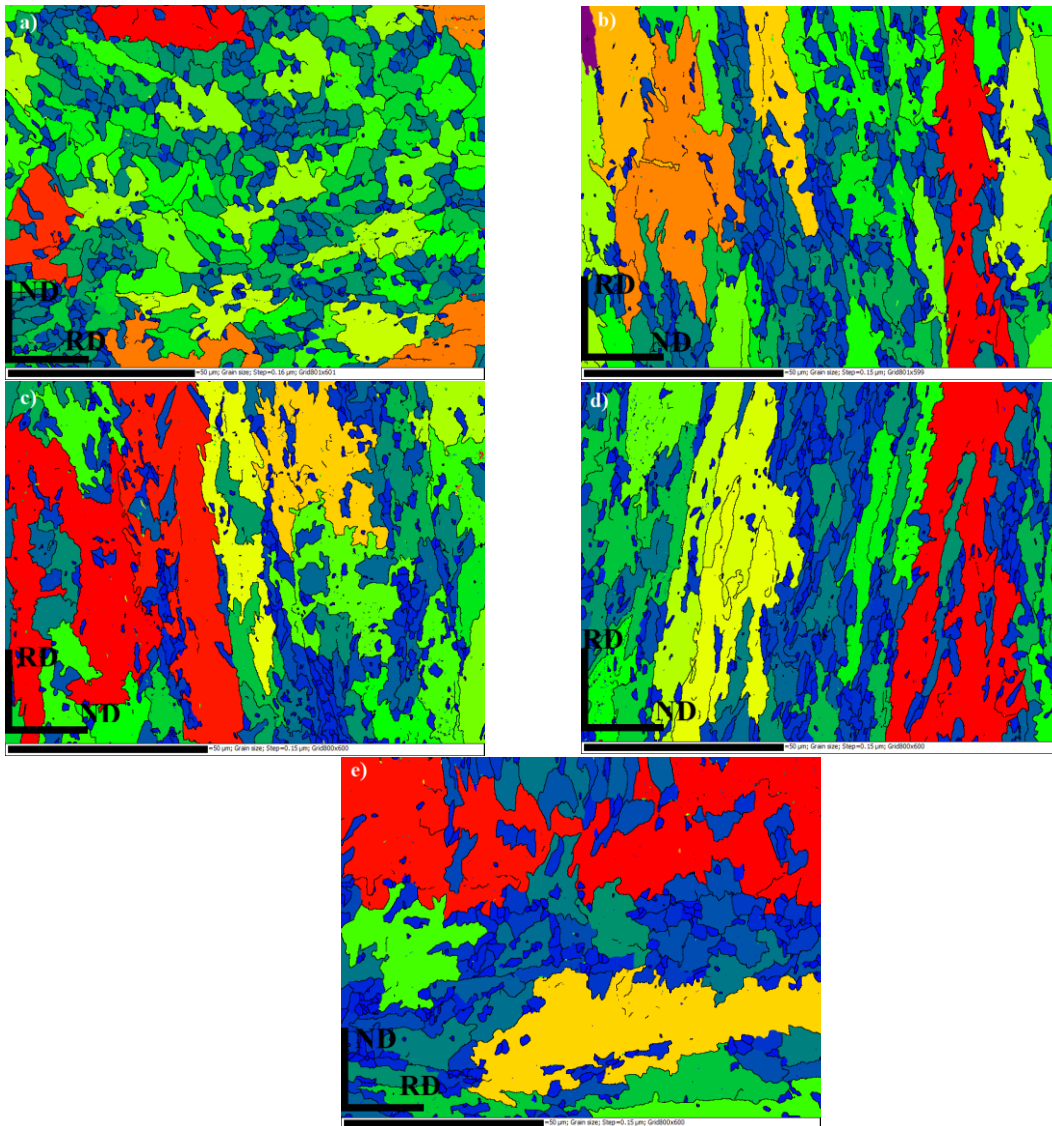


Figure 4.4. The grain size of a) X70-1, b) X70-2-1, c) X70-2-2, d) X70-3-1, e) X70-3-2 samples at middle layer.

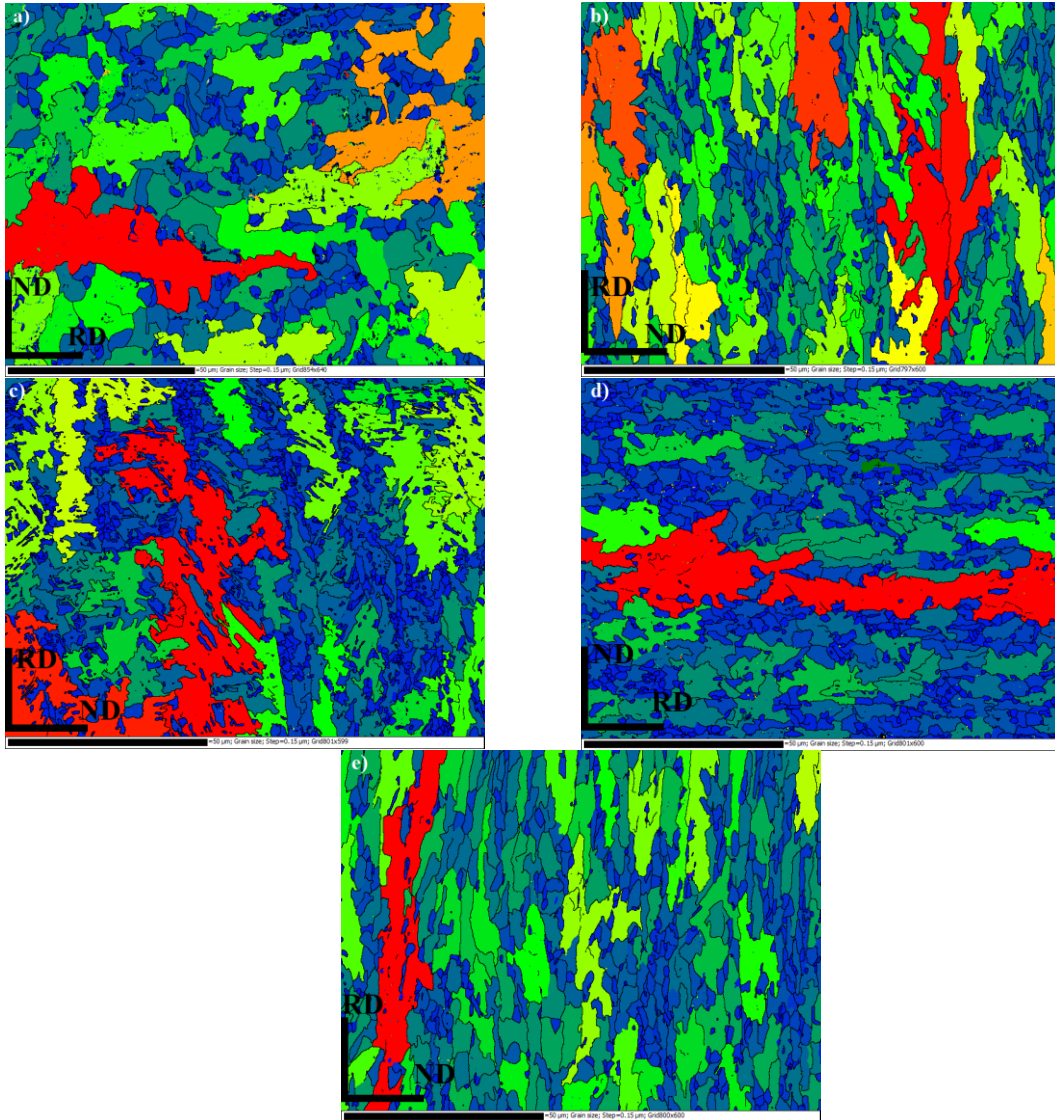


Figure 4.5. The grain size of a) X70-1, b) X70-2-1, c) X70-2-2, d) X70-3-1, e) X70-3-2 samples at top layer.

Because of different TMCP in the samples, different grain sizes can be seen in them. The samples' grain size statistics, including the minimum, maximum, and average grain size of each specimen, are provided in Table 4.1.

Table 4.1. Grain size distribution of the samples.

Pipe	Middle layer					Top layer				
	X70-1	X70-2		X70-3		X70-1	X70-2		X70-3	
#	-	1	2	1	2	-	1	2	1	2
D_{\min} (μm)	0.18	0.17	0.17	0.17	0.17	0.17	0.17	0.17	0.17	0.17
D_{\max} (μm)	31.1	46.93	60.50	65.48	86.84	52.02	39.14	55.2	57.17	40.64
D_{ave} (μm)	2.68	2.71	2.31	2.34	3.28	1.40	2.53	1.32	1.94	2.76

The TMCP of the samples directly reflects these grain sizes. The largest grains are measured in X70-3-2, where the least rolling passes happened. There were six roughing and five

finishing passes (Table 3.2) in this specimen. This specimen's cooling rate was lowest, too (26.9 C/s). On the other hand, if comparing two different X70-2 samples with varying parameters of TMCP, it is understandable that the smaller grains are presented in X70-2-2 specimen in both top and middle layers. Although the rough rolling steps were 5 in X70-2-2 (compared with 8 in X70-2-1), there was more finish rolling steps in this specimen (7 compared with 5 in X70-2-1). This suggests that the number of finish rolling is more critical than rough rolling in shaping the smaller grains. The same conclusion can be reached by comparing X70-3 specimens. The rough rolling was the same in X70-3-1 and X70-3-2 specimens; the only difference was the finish rolling steps number (seven steps in X70-3-1 and five in X70-3-2). The other difference in X70-2 specimens is their cooling rate. This number was 62.5 C/s and 30.8 C/s in X70-2-2 and X70-2-1 specimens. The higher cooling rate in X70-2-2 did not allow the grains to grow and created some martensite phase in this specimen. The cooling rate was similar across the X70-3 specimens. Altogether, from this table, it is evident that the smallest grains belong to the X70-2-2 specimen, while the largest one is for X70-3-2. Here we just compared the grain size of X70-2 and X70-3 samples with different TMCP parameters, and the X70-1 grain size just reported for further analysis and tests on this specimen.

4.2 Texture and phase characterization of as-received samples

The effect of texture and grain boundary is undeniable on the mechanical properties and HIC resistance of the steels. Changing the texture and grain boundaries is an innovative technique that is considered an effective way to increase both HIC resistance and steels' mechanical properties. In this section, the texture and phase characterization of all samples are presented using the EBSD technique. This section contains the phase map, inverse pole figure, misorientation, and recrystallization fraction for both the middle and top layers of all samples.

The phase map of the samples is presented in Figures 4.6 and 4.7. From photos, all samples in the top and middle layers mostly consist of BCC structure. The high angle grain boundaries ($\theta > 15^\circ$) are set in the software to show in all phases. It is worth mentioning that the ferrite phase has the highest resistance to the HIC phenomenon. However, it has almost lower strength in comparison with the other phases. Therefore, pipeline manufacturers should provide some additional phases to increase the strength of steel. For instance, adding manganese to the steel increases the strength of it by solid solution strengthening phenomenon. Moreover, the pearlite

microstructure has a higher strength than ferrite. Therefore, the main objective would be to provide the optimum situation for the product based on the strength and crack propagation resistivity.

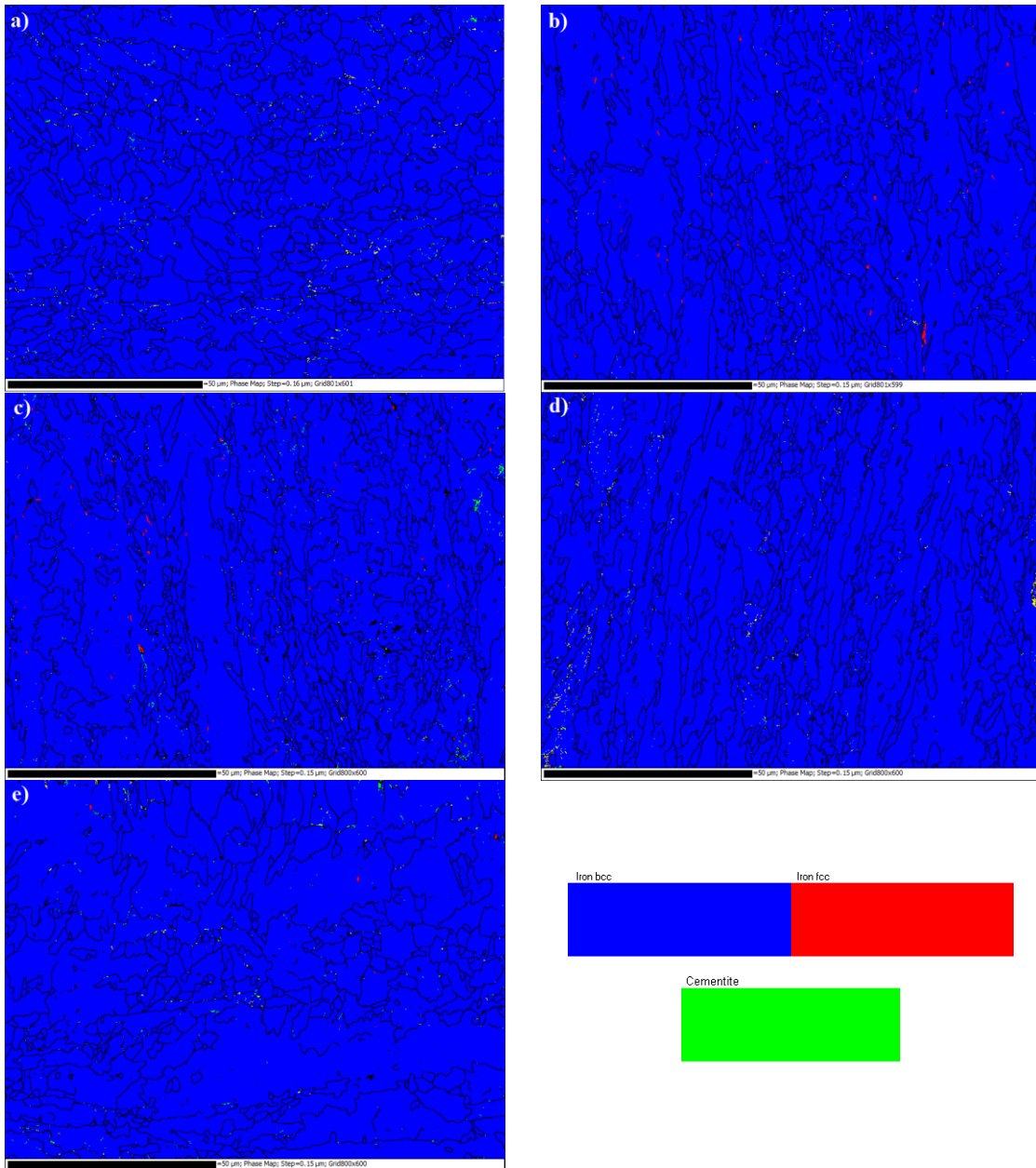


Figure 4.6. The Phase map of a) X70-1, b) X70-2-1, c) X70-2-2, d) X70-3-1, e) X70-3-2 samples at middle layer.

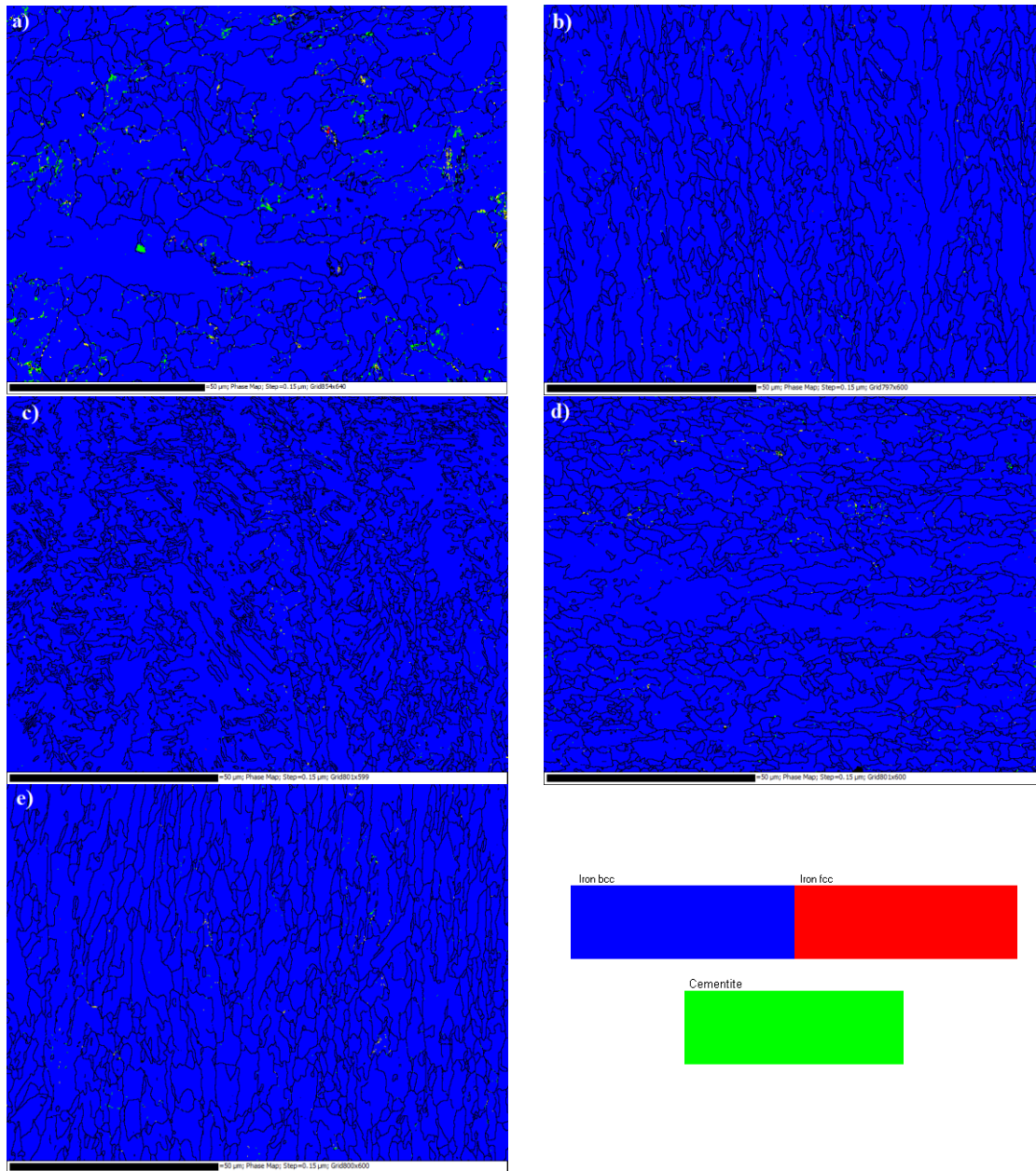


Figure 4.7. The Phase map of a) X70-1, b) X70-2-1, c) X70-2-2, d) X70-3-1, e) X70-3-2 samples at top layer.

The phase map of all samples are shown in figures 4.8 and 4.9. From the maps, it can be concluded that there is no dominant texture in the samples and that the grains are distributed in random directions. When the texture is random in a region, the HIC crack can easily propagate [121, 122]. As a result, it is impossible to judge the HIC susceptibility of these samples and layers based on the macro-texture study.

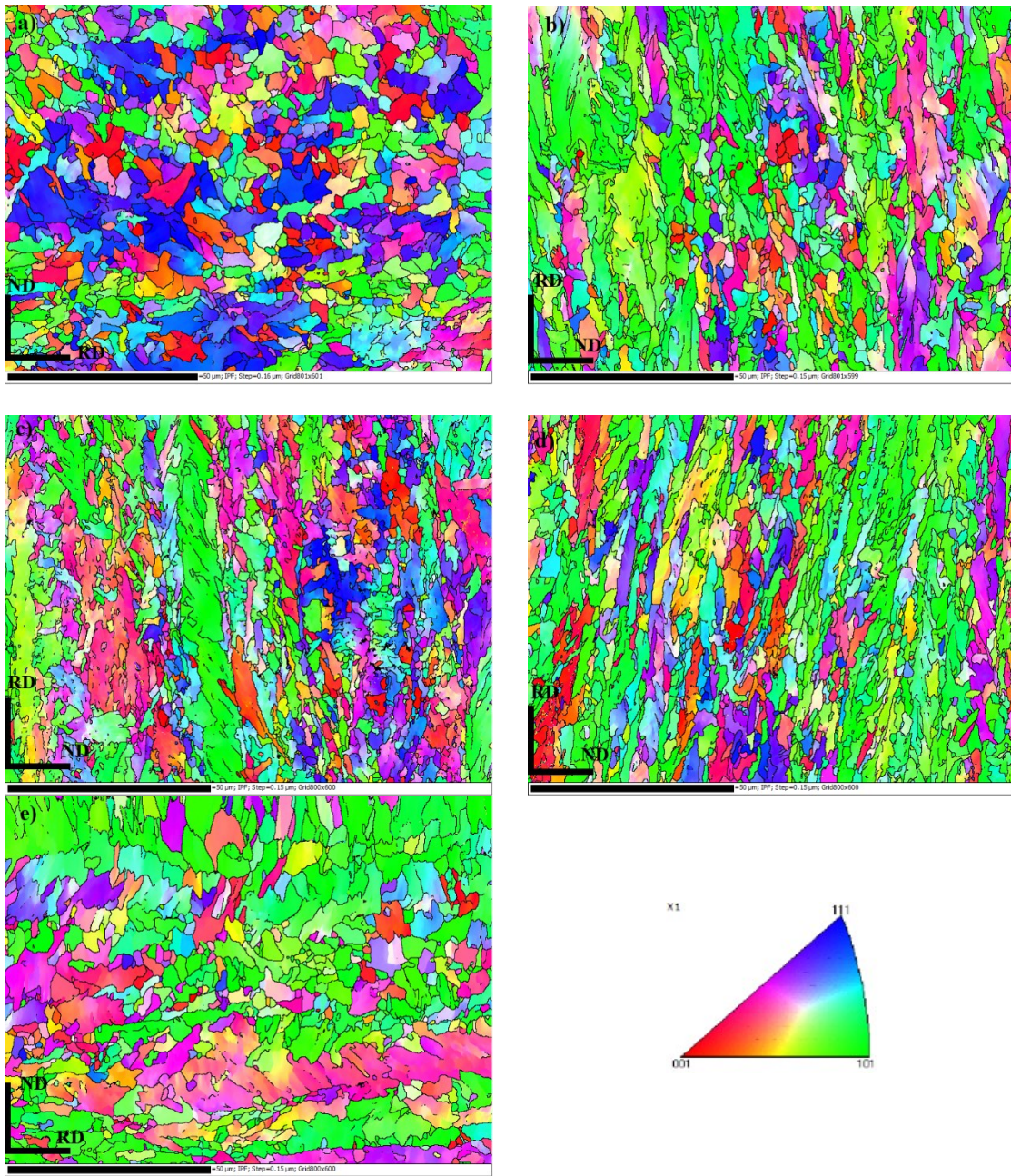


Figure 4.8. The IPF a) X70-1, b) X70-2-1, c) X70-2-2, d) X70-3-1, e) X70-3-2 samples at middle layer.

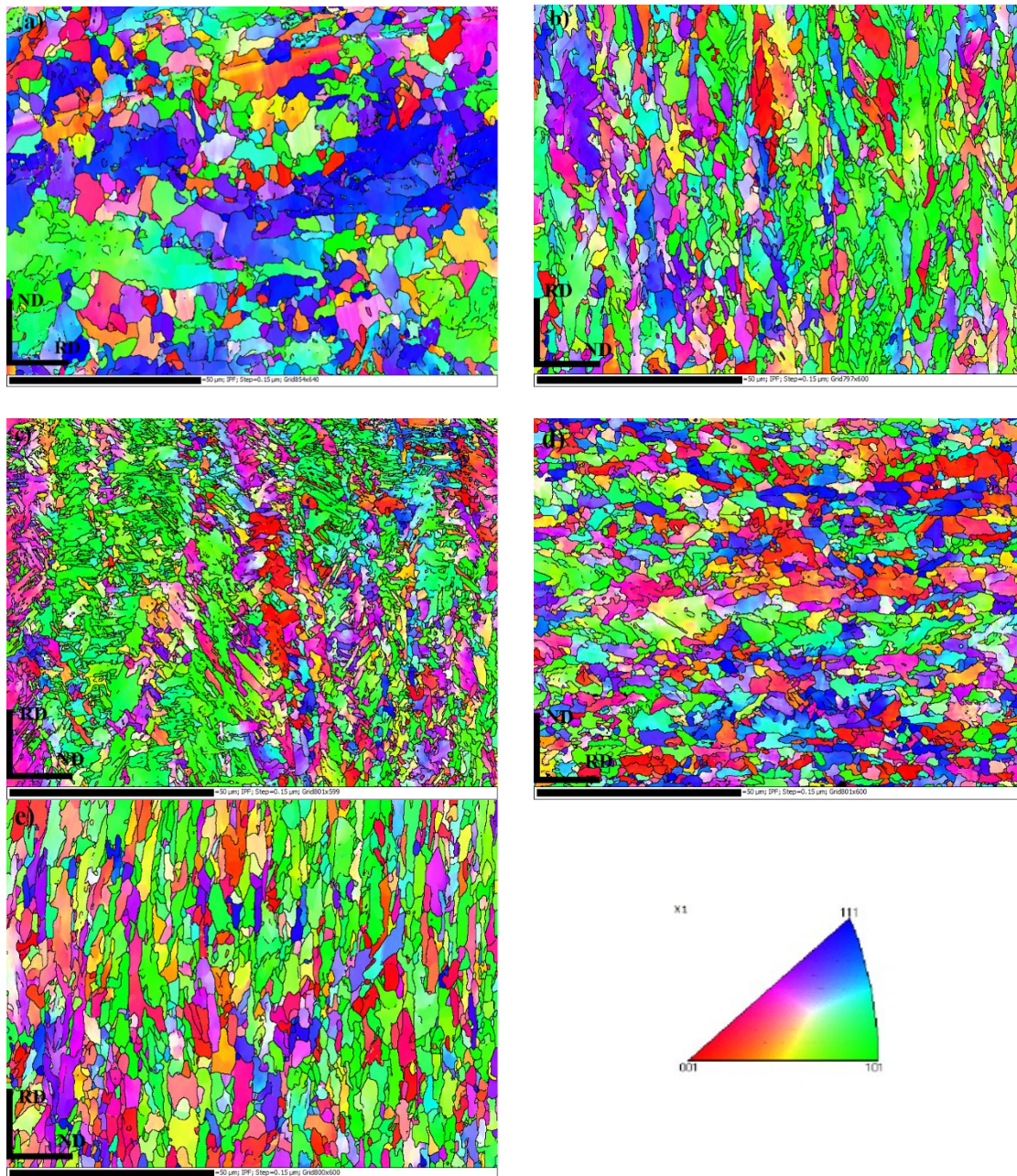


Figure 4.9. The IPF of a) X70-1, b) X70-2-1, c) X70-2-2, d) X70-3-1, e) X70-3-2 samples at top layer.

The kernel average misorientation (KAM) of both top and middle layers is shown in Figures 4.10 and 4.11. The Kernel map shows the average misorientation between a given point and its nearest neighbours that belongs to the same grain [125]. In other words, the regions with high kernel data have a high dislocation density and can be considered as hydrogen trap sites. In comparison between KAM maps, it is seen that the X70-2-2 sample has more misorientations higher than 1° , and this can be as a result of higher cooling rate and creation of residual stresses in this sample.

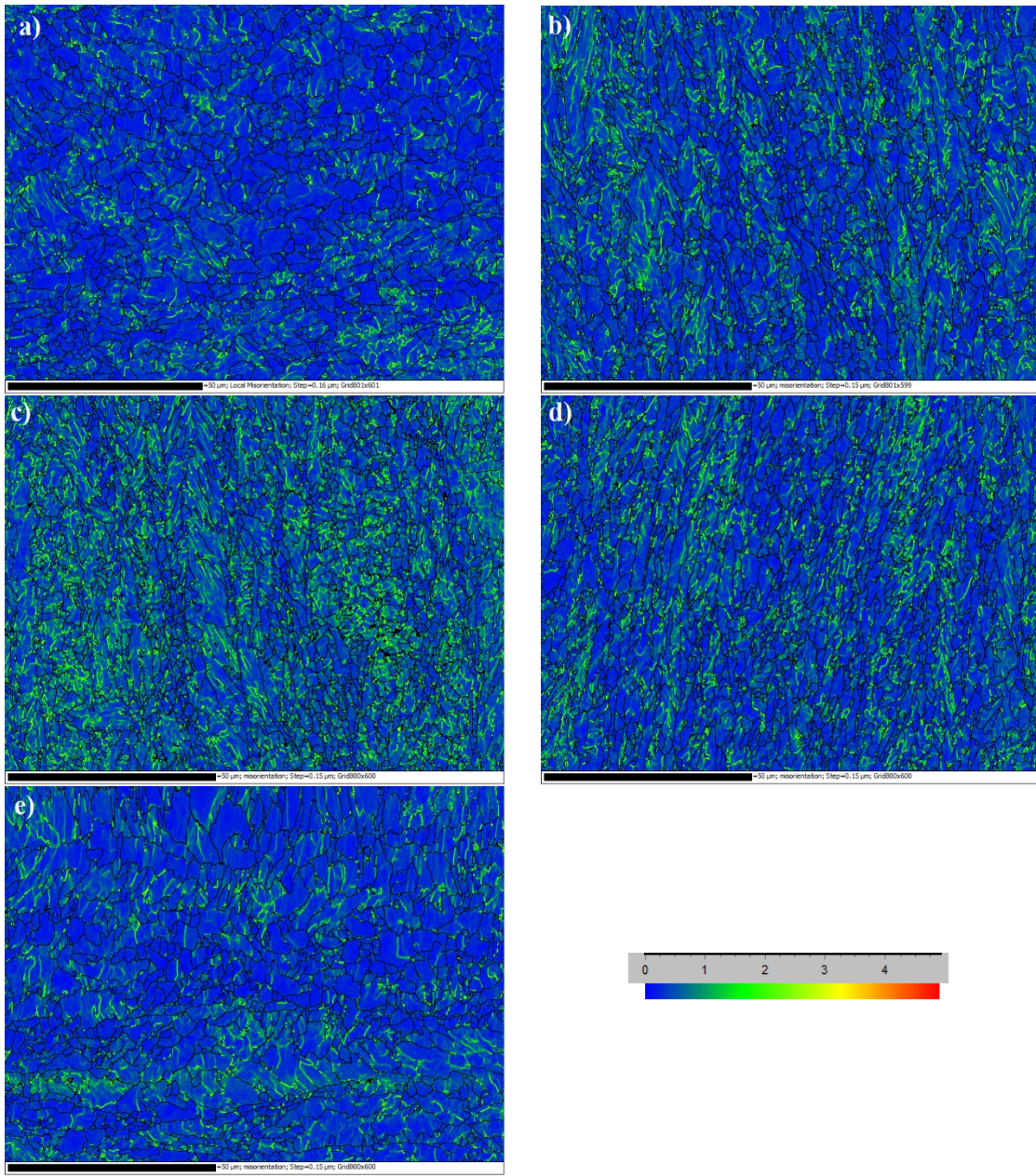


Figure 4.10. The KAM map of a) X70-1, b) X70-2-1, c) X70-2-2, d) X70-3-1, e) X70-3-2 samples at middle layer.

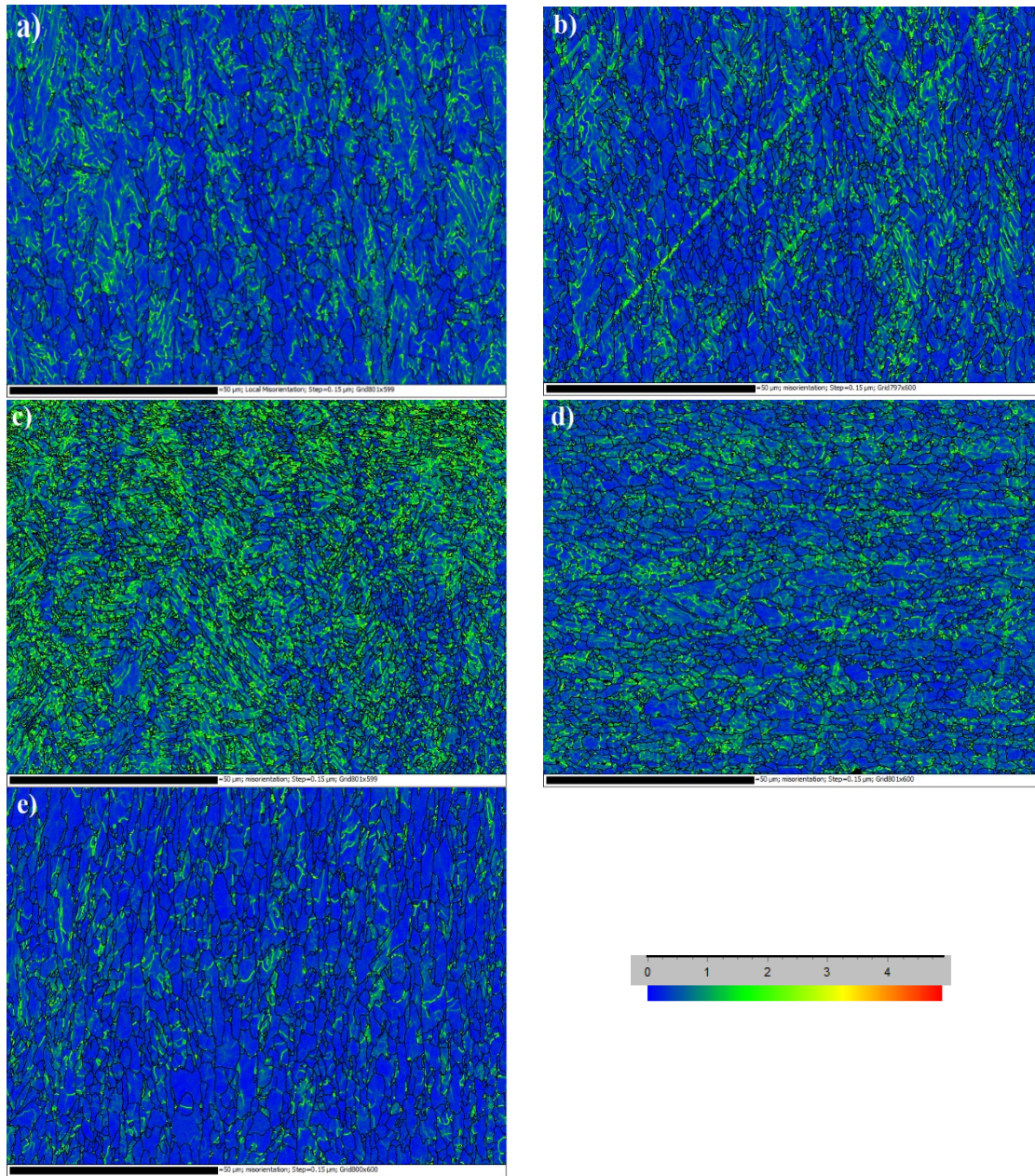


Figure 4.11. The KAM map of a) X70-1, b) X70-2-1, c) X70-2-2, d) X70-3-1, e)X70-3-2 samples at top layer.

The recrystallization fraction of both top and middle layers is shown in Figures 4.12 and 4.13, in which the blue, yellow, and red colours represent the recrystallized grains, sub structured, and deformed grains, respectively.

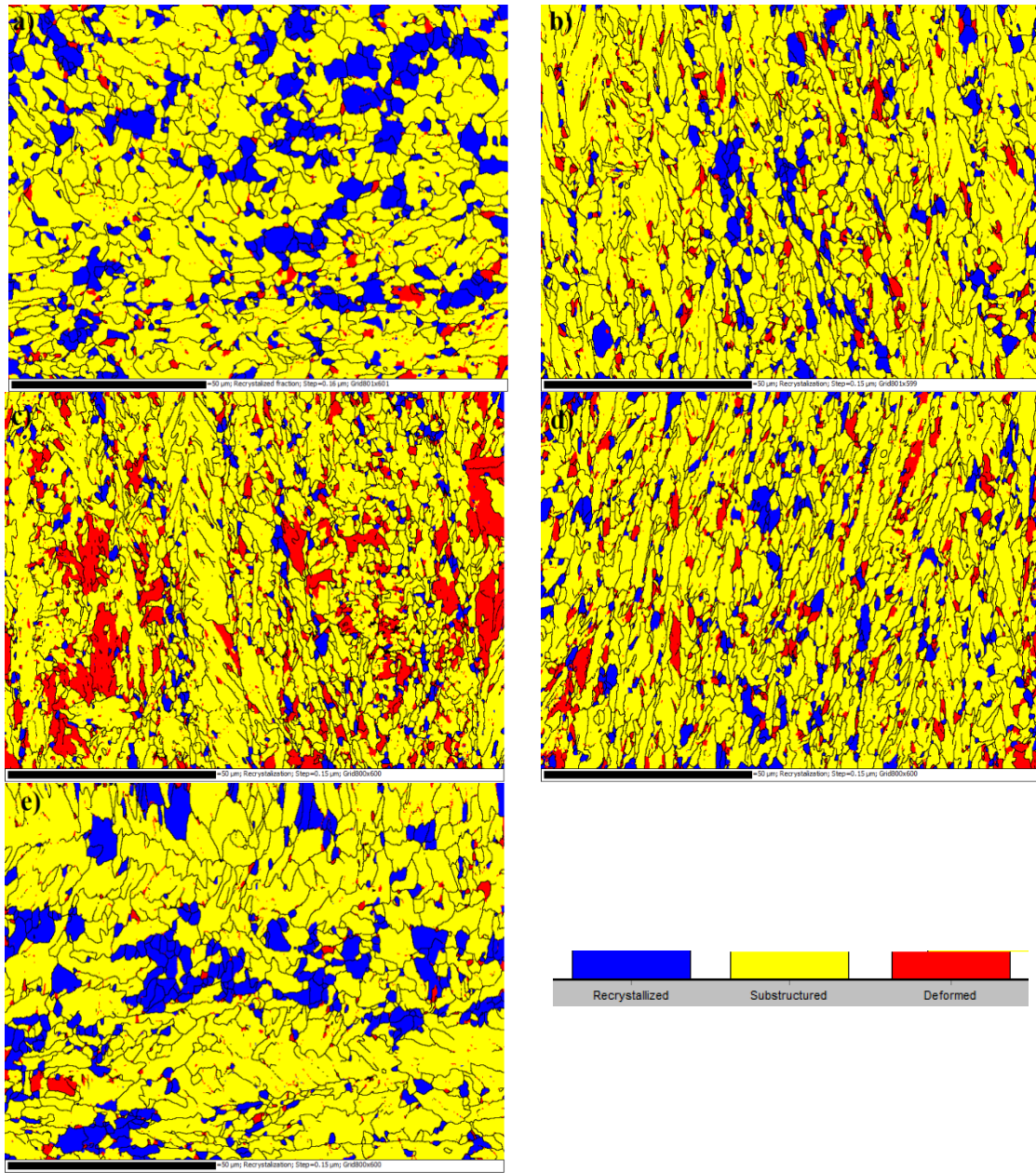


Figure 4.12. The recrystallization fraction of a) X70-1, b) X70-2-1, c) X70-2-2, d) X70-3-1, e)X70-3-2 samples at middle layer.

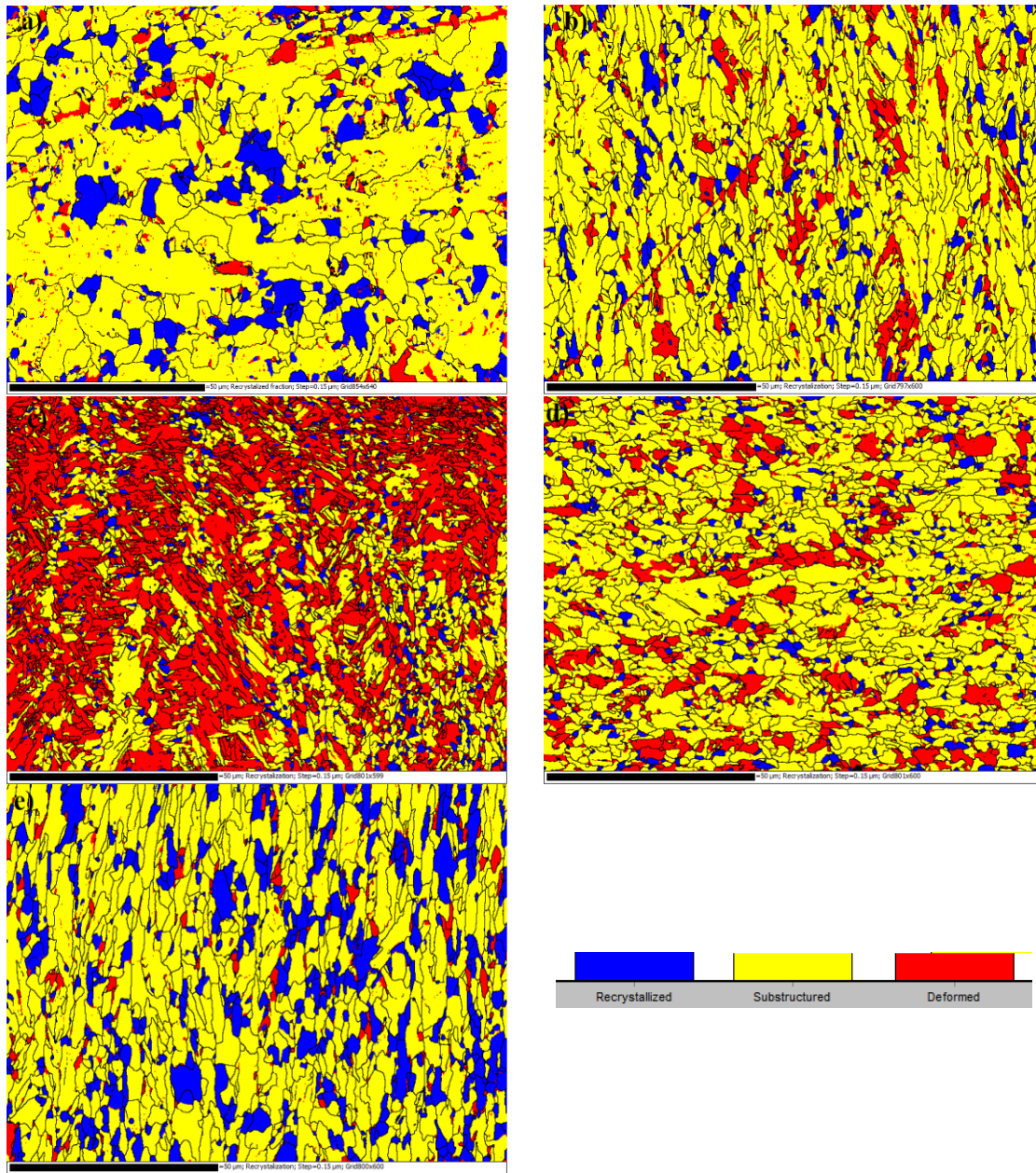


Figure 4.13. The recrystallization fraction of a) X70-1, b) X70-2-1, c) X70-2-2, d) X70-3-1, e) X70-3-2 samples at top layer.

The detailed recrystallization fraction of the BCC phase for all samples is presented in Table 4.2.

Table 4.2. The recrystallization fraction of BCC phase in the samples.

Pipe	#	Top layer			Middle layer		
		Recrystallized (%)	Substructured (%)	Deformed (%)	Recrystallized (%)	Substructured (%)	Deformed (%)
X70-1	-	15.9	78.8	5.3	21.4	76.2	2.4
X70-2	1	8.4	80.5	11.1	10	83.8	6.2
	2	6.6	34.8	58.6	6	74.6	19.4
X70-3	1	6.7	72.8	20.5	9.6	80.1	10.3
	2	23.2	71.9	4.9	17.4	79.9	2.7

In this table, the highest deformed fraction belongs to X70-2-2, followed by X70-3-1 and X70-2-1 samples in both top and middle layers. The least deformed fraction of the BCC phase is related to X70-3-2 and X70-1 samples in the top and middle layers. On the other hand, the fraction of recrystallized phases has the opposite manner in the samples. X70-2-2 and X70-3-1 have the lowest recrystallized fraction, while X70-3-2 and X70-1 have the highest amounts. The table also shows that the greatest fraction of the BCC structure (>72%) in the samples remains in their initial shape (Sub-structured fraction) except in the top layer of the X70-2-2 specimen.

4.3 Mechanical testing

4.3.1 Tensile and hardness testing results

The S-S diagram of all samples after the TMCP procedure are presented in Figure 4.14 and Table 4.3.

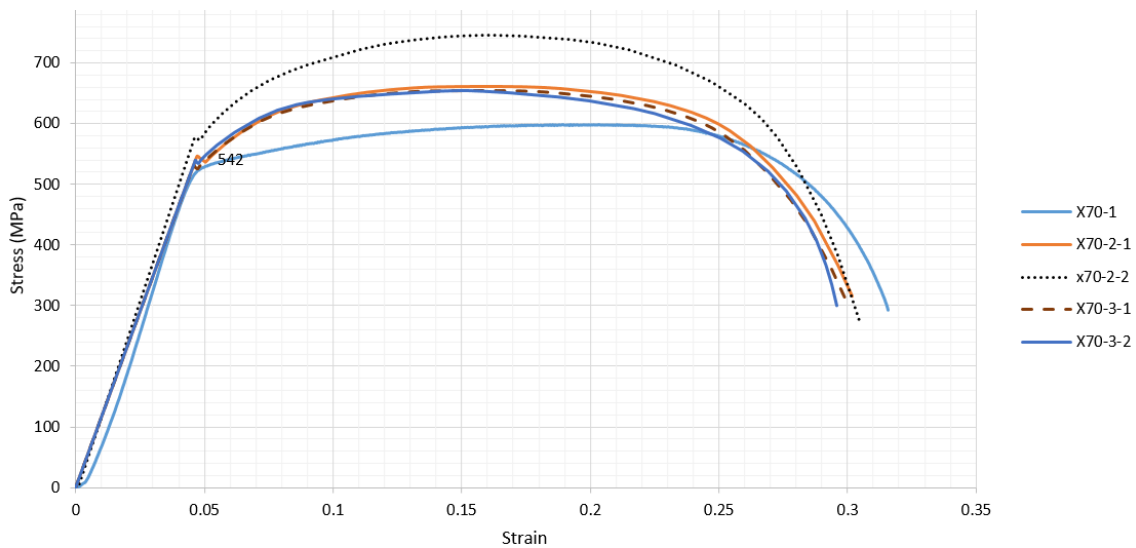


Figure 4.14. Stress-Strain diagram of the samples.

Table 4.3. Mechanical properties of the samples before and after hydrogen charging.

	YS (MPa)	UTS (MPa)	HV
As-received samples' surface			
X70-1	521	598	228
X70-2-1	547	661	205
X70-2-2	578.5	745.5	238
X70-3-1	533.7	629.7	219
X70-3-2	540.7	654	202
After hydrogen charging			
X70-1	-	-	241
X70-2-1	-	-	216
X70-2-2	-	-	244
X70-3-1	-	-	234
X70-3-2	-	-	218

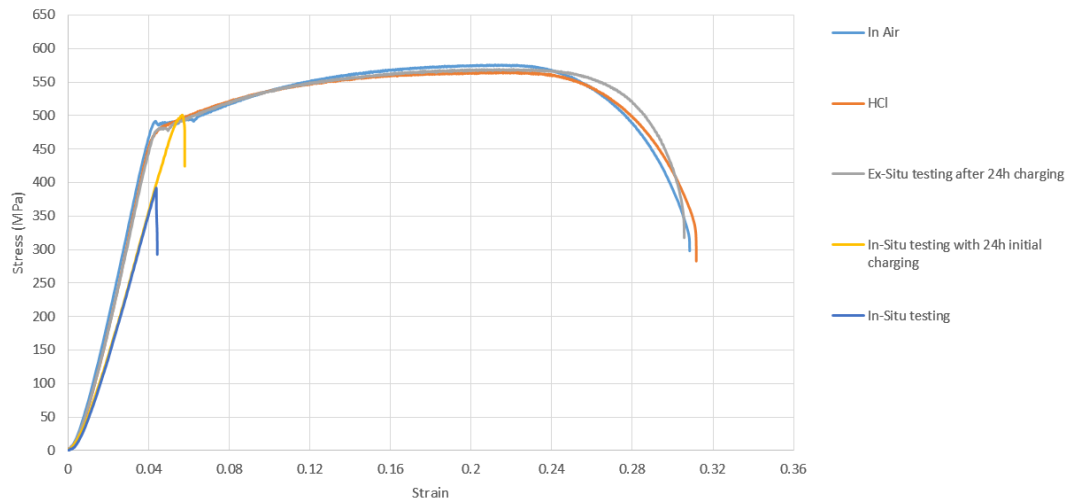
According to the table and diagram, the yield and ultimate stresses of the X70-2-2 sample are higher than other samples, while these strengths are lower for the X70-1 sample. This table shows that the grain size and the steel phases are not the only parameters that affect the steel's strength.

The hardness of samples measured between 202 HV and 238 HV. The highest hardness is for X70-2-2, while the lowest one is for the X70-3-2 specimen. All these numbers are justifiable by specimens' microstructure. The smallest grain size is for X70-2-2, where the highest hardness and strengths happened there. There was also some martensite microstructure in this specimen. On the other hand, the largest grain size is for X70-3-2, the specimen with the lowest hardness. This results suggest that the hardness of steel has a direct relationship with its grain size: the larger the grain size, the lower the hardness. The small grains create more grain boundaries and the grain boundaries act as a barrier for the dislocations' motion. This interfering with the movement of the dislocations, the metal becomes harder. It is a reason for the observations in this study.

As mentioned in the experimental procedure section, the effects of different environmental conditions on the mechanical properties of X70-1 steel are investigated. For this purpose, the tensile stress testing is conducted in five different environmental conditions. Three of them are in

the presence of hydrogen charging, one in an acidic environment, and the other is conducted in an ambient condition. The test results are presented in Figure 4.15.

a)



b)

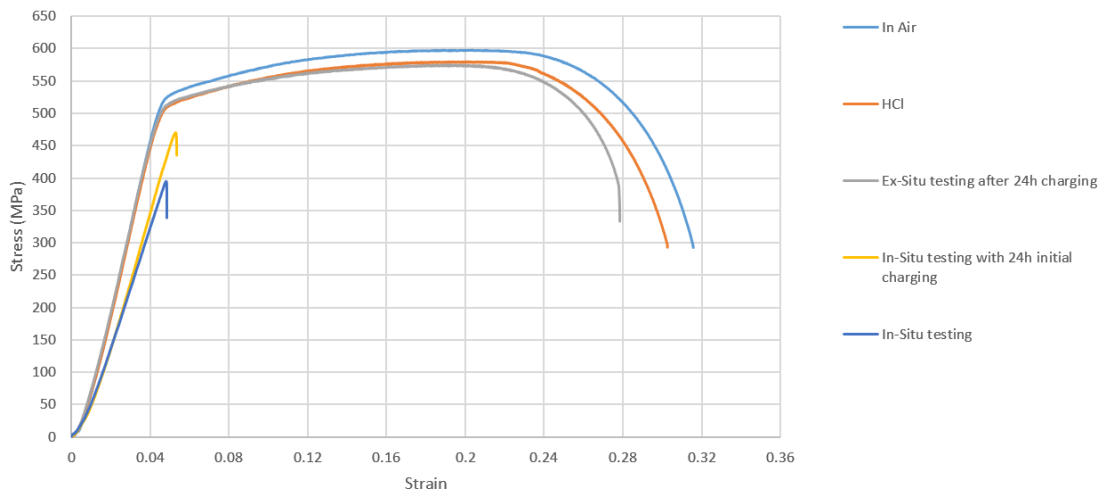


Figure 4.15. Stress-Strain diagram of a) middle, and b) top layer of X70-1 steel in different environmental conditions.

The test results indicate that the acidic environment and Ex-Situ testing do not significantly affect the strength of API X70 pipeline steels, while the in-situ hydrogen charging can substantially change the mechanical properties of steels. This indicates that the in-situ charging might decrease the tensile modulus and the mechanism of failure. The yield stress goes down for the in-situ charging test, followed by sudden failure without any plastic deformation. It is concluded that the effect of hydrogen on the strength of steels is temporary, and if hydrogen atoms are allowed to escape from reversible traps, the steel strength will be the same as before without any change and the irreversible traps do not have significant effects on the mechanical properties of the samples.

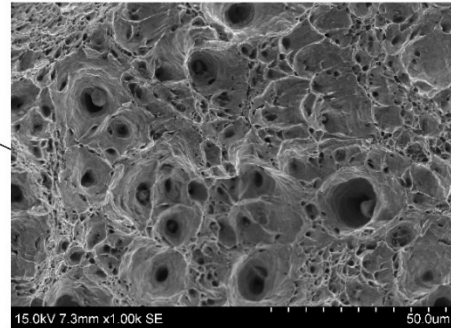
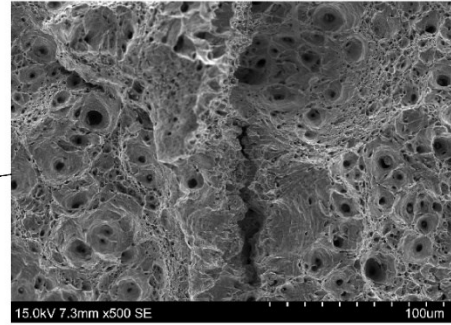
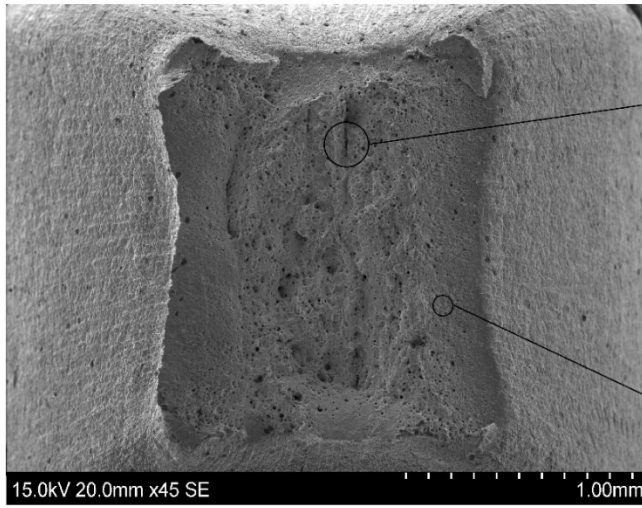
The accumulation of some elements such as manganese, phosphorous, and carbon at the center segregated zone increases this region's yield stress. For instance, the manganese element increases the strength of steel by solid solution strengthening. Moreover, the alloying elements' segregation usually happens at the slab's mid-thickness because of final solidification happening during casting. However, it is possible to reduce the effect of the center segregated zone by special TMCP. Tamehiro et al. [112] investigated the effect of accelerated cooling after controlled rolling on the HIC resistance of pipeline steel. These researchers concluded that the high cooling rate and the optimized start and finish temperatures in accelerated cooling might avoid the rejection of carbon from the non-segregated area to the segregated zone during the austenite to ferrite transformation. This phenomenon makes a more uniform distribution of carbon in the through-thickness direction of the plate. By such a TMCP process, these researchers improved the HIC resistance in pipeline steels. In our research, we could not find any elements' segregation effects on the strength of the samples, and the grain size effects on the strength of the samples in both top and middle layers are bolder.

The other point related to the S-S diagram is the relation between the sample grain size and their strength in the top and middle layers. The steels' overall yield and ultimate strength in their middle layers are about 20 MPa less than what they are in the top layers. The average grain size of the X70-1 specimen in the middle layer is 1.28 microns more than the top layer. These results indicate that the smaller grains result in higher mechanical strength of the steel.

4.3.2 Fractography of failed samples

SEM was used to study the fracture mechanism and its relation to the obtained stress-strain curves in the X70-1 samples. The fracture surfaces of both layers (top and middle) were almost the same, and therefore only images of the middle layer samples are presented in Figure 4.16.

a)



b)

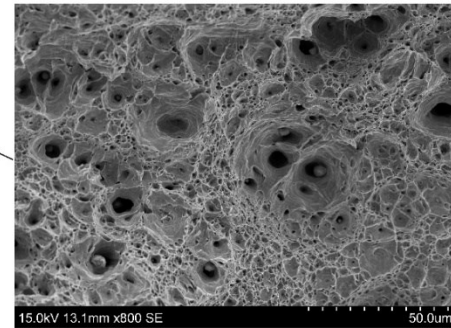
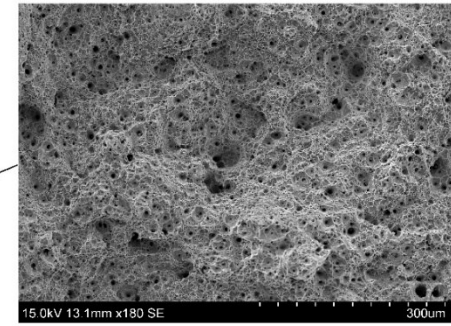
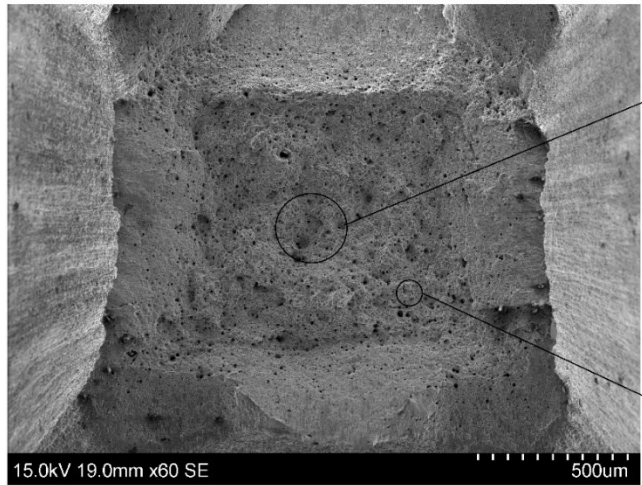
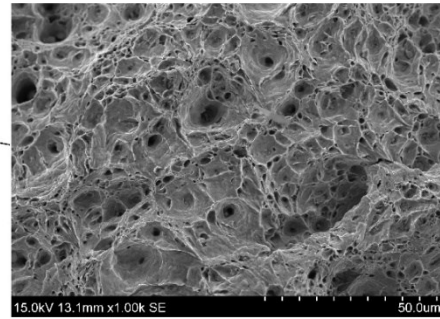
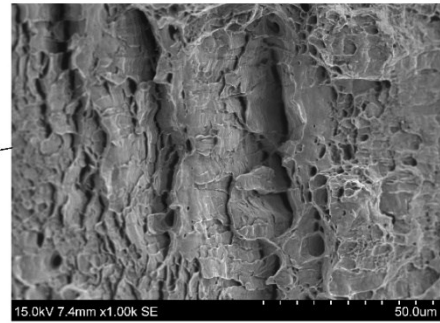
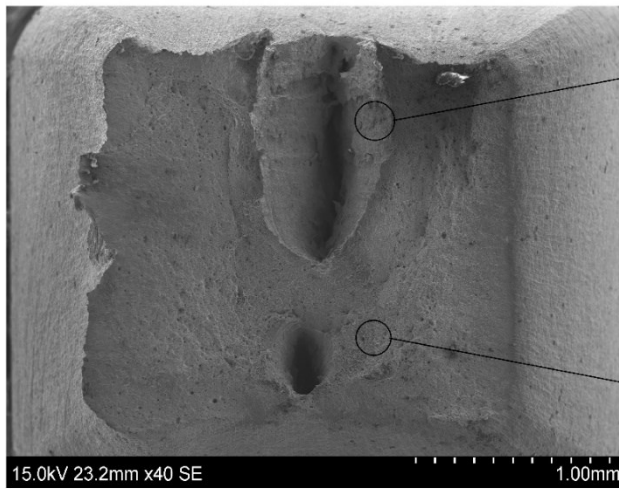


Figure 4.16. SEM images from fracture surface of X70-1 in a) Air condition, b) Acidic environment, c) Ex-Situ testing after 24h hydrogen charging, d) In-Situ testing after 24h hydrogen charging, e) In-Situ testing without initial hydrogen charging.

c)



d)

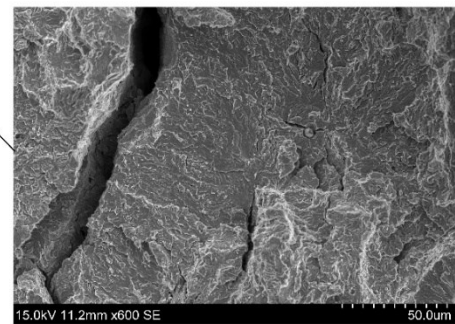
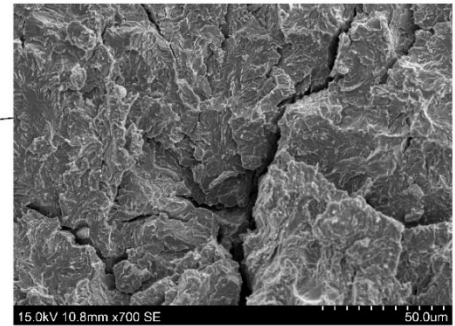
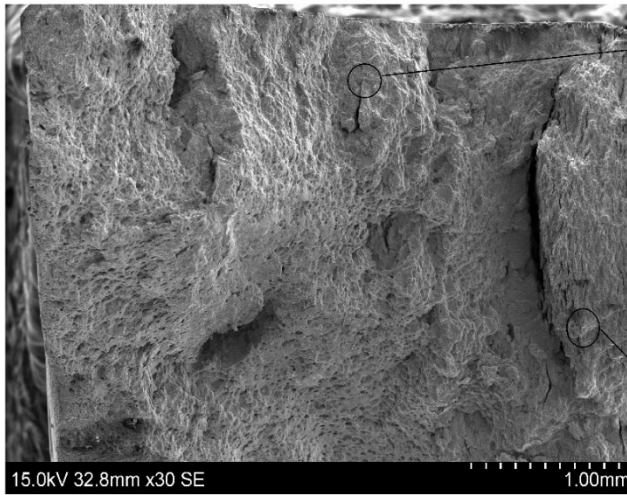


Figure 4.16. SEM images from fracture surface of X70-1 in a) Air condition, b) Acidic environment, c) Ex-Situ testing after 24h hydrogen charging, d) In-Situ testing after 24h hydrogen charging, e) In-Situ testing without initial hydrogen charging. (Cont.)

e)

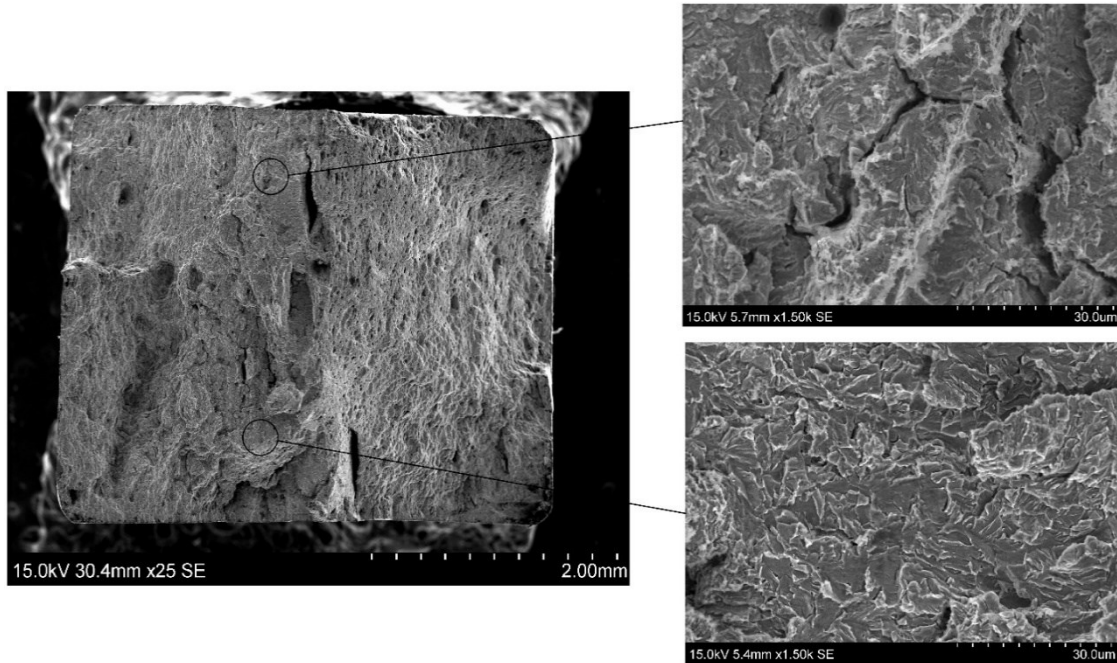


Figure 4.16. SEM images from fracture surface of X70-1 in a) Air condition, b) Acidic environment, c) Ex-Situ testing after 24h hydrogen charging, d) In-Situ testing after 24h hydrogen charging, e) In-Situ testing without initial hydrogen charging. (Cont.)

It is seen that the first two experiments in air and acidic environments experienced a ductile failure. For Ex-Situ tensile testing, many pits were found on the fracture surface, proving a ductile fracture. There were also some flat surfaces, especially around the crack at the center of the fracture surface, which is evidence for a brittleness caused by hydrogen charging. For In-Situ tensile testing without/with initial hydrogen charging, almost all parts of the fracture surface consisted of flat surfaces. This means that the brittle fracture occurred. These observations are consistent with the results obtained from the strain-stress diagrams.

The EDS results on the fracture surface of the samples show the inclusions and/or other impurities, as shown in Figure 4.17. These inclusions included CaS, Al₂O₃, and MnS and were almost the same in all samples. The number of inclusions observed in the fracture surface of the sample tested in an ambient condition was less than the other samples tested in the acidic and sour environments. Most of the inclusions in the fracture surface of the samples were CaS and Al₂O₃ types. Manganese sulfide inclusion was rarely observed compared to the previous generation of pipelines manufactured with the same company [75]. The inclusions are usually placed in the pits showing the incoherency of inclusions with the metal matrix from the EDS photos. Moreover, these pits, together with inclusions, can be the crack initiation sites [75].

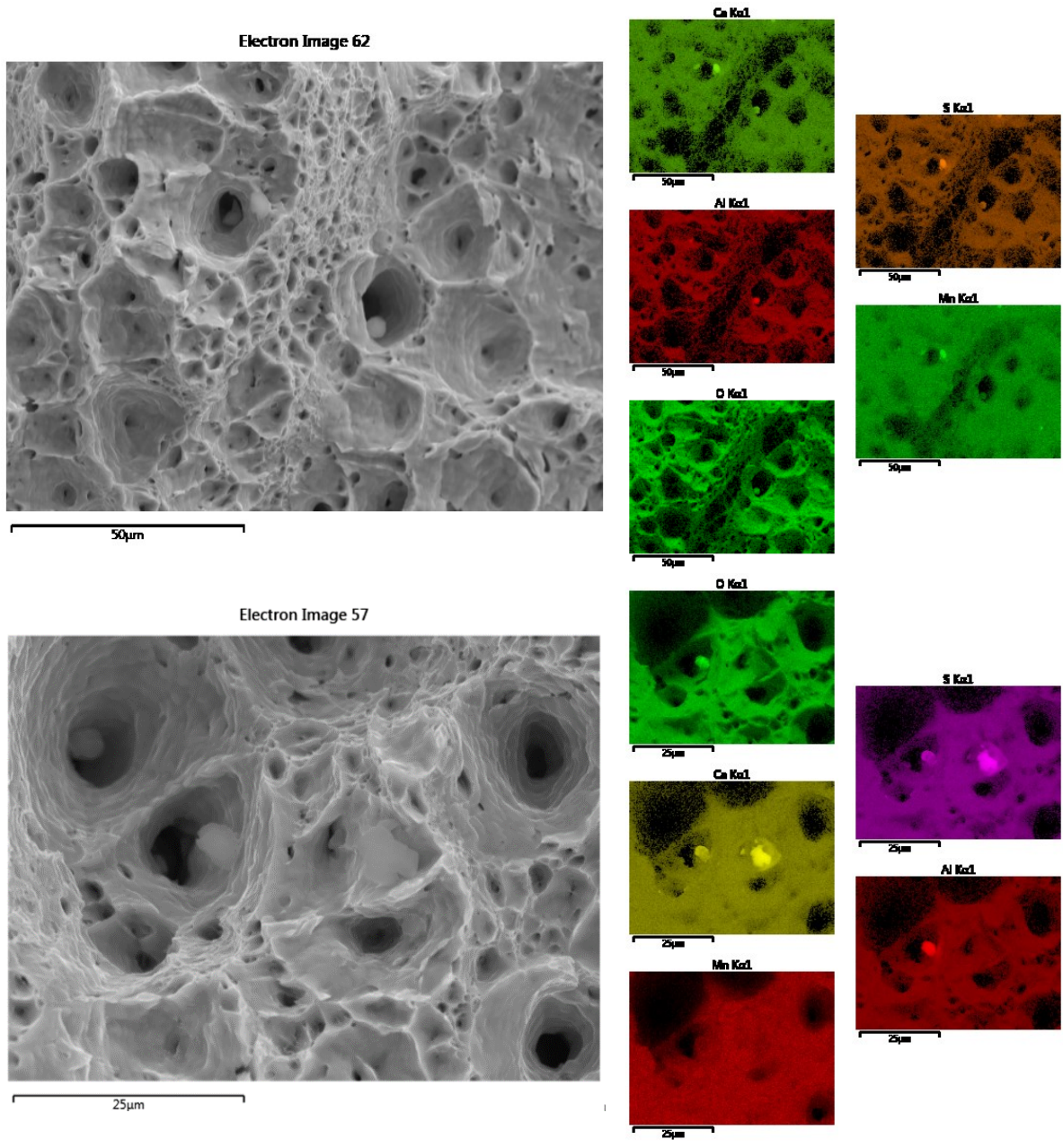


Figure 4.17. EDS images from fracture surface of electrochemically charged samples.

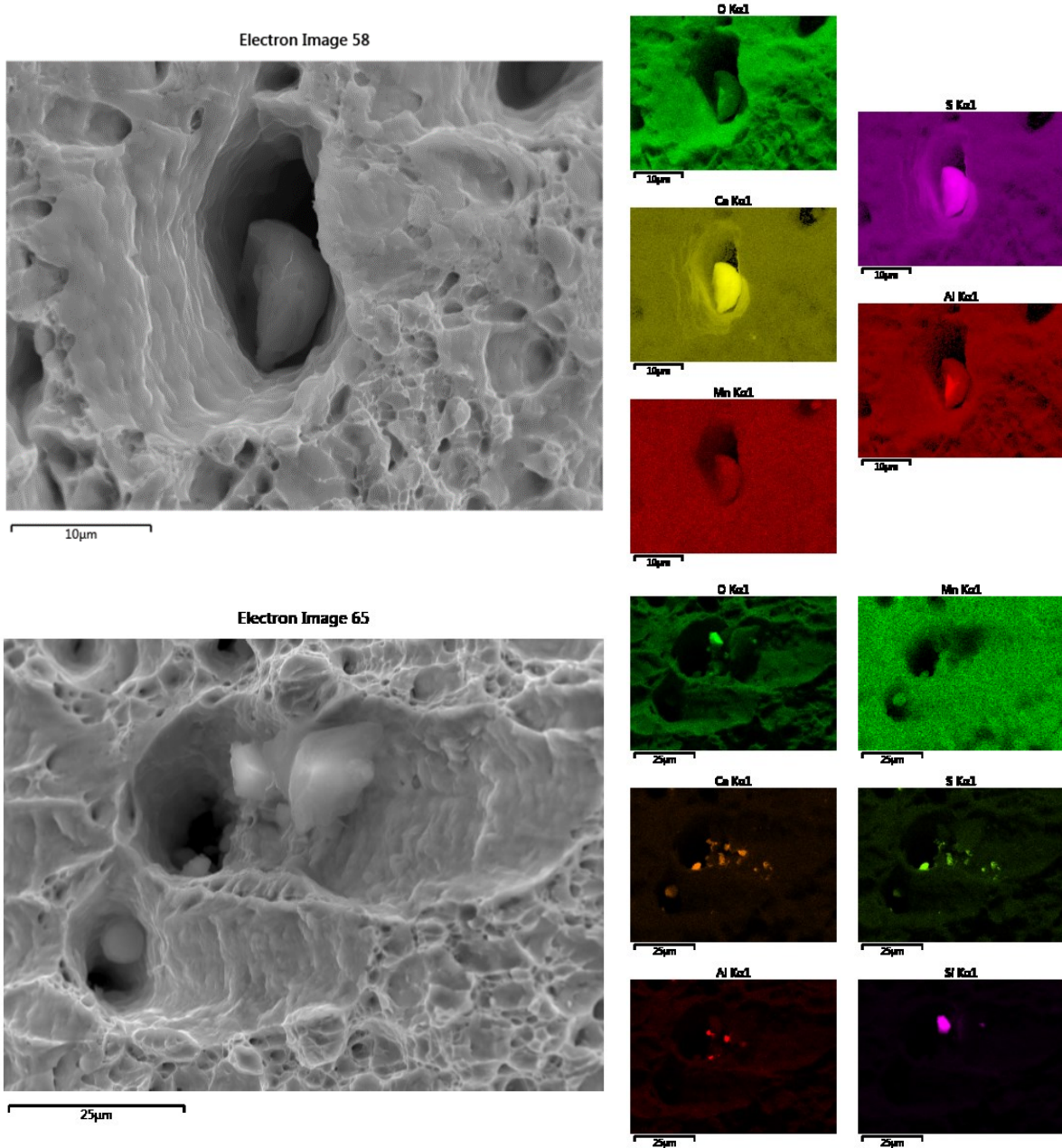


Figure 4.17. EDS images from fracture surface of electrochemically charged samples. (Cont.)

4.4 HIC testing results

As mentioned in the procedure section, the samples were electrochemically charged to evaluate samples' resistance to HIC cracking. The hydrogen charging causes cracking and blistering on the surface of samples. The blisters of the samples are shown in Figure 4.18.

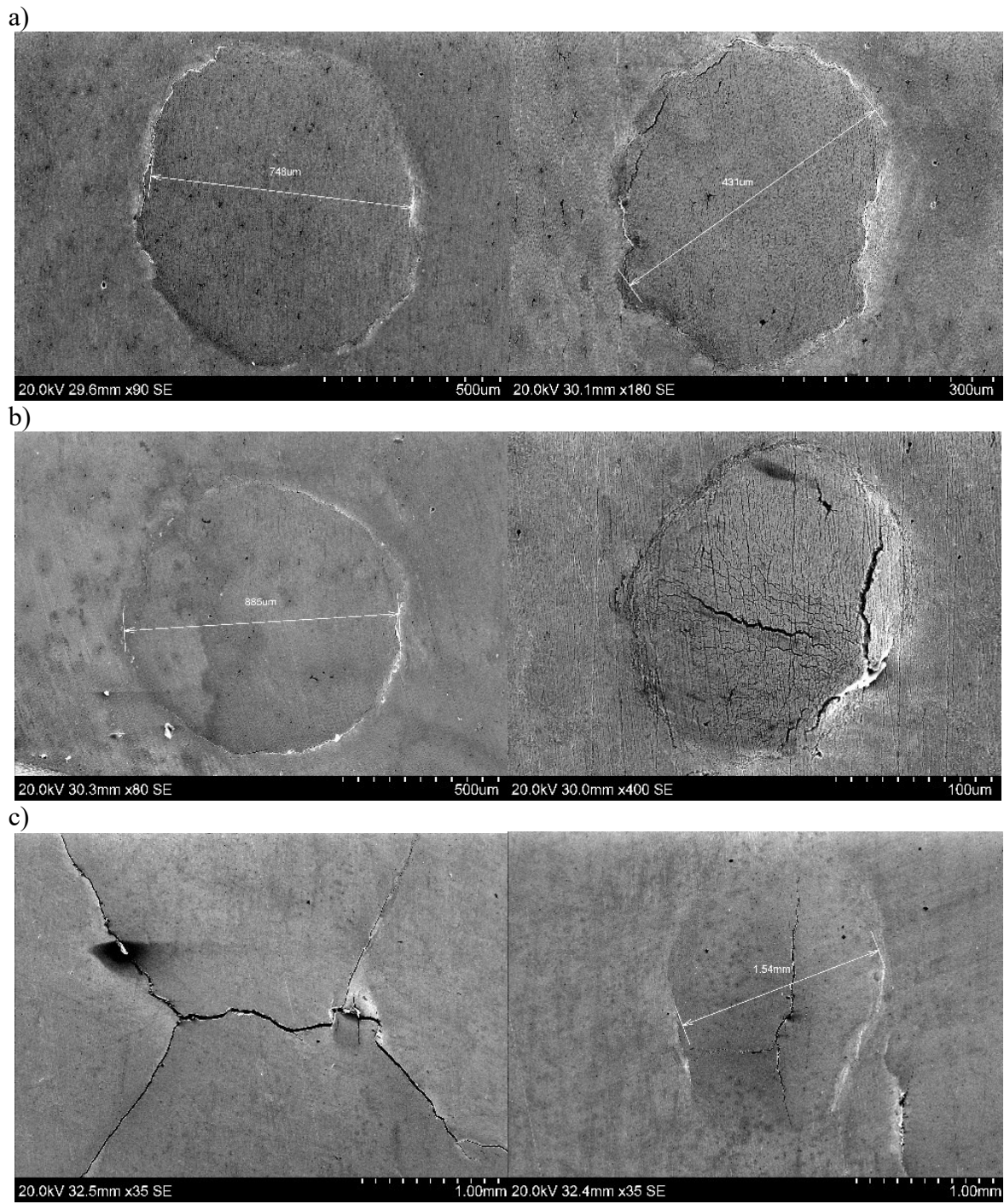


Figure 4.18. The examples of blisters on a) X70-1, b) X70-2-1, c) X70-2-2, d) X70-3-1, e) X70-3-2 surfaces.

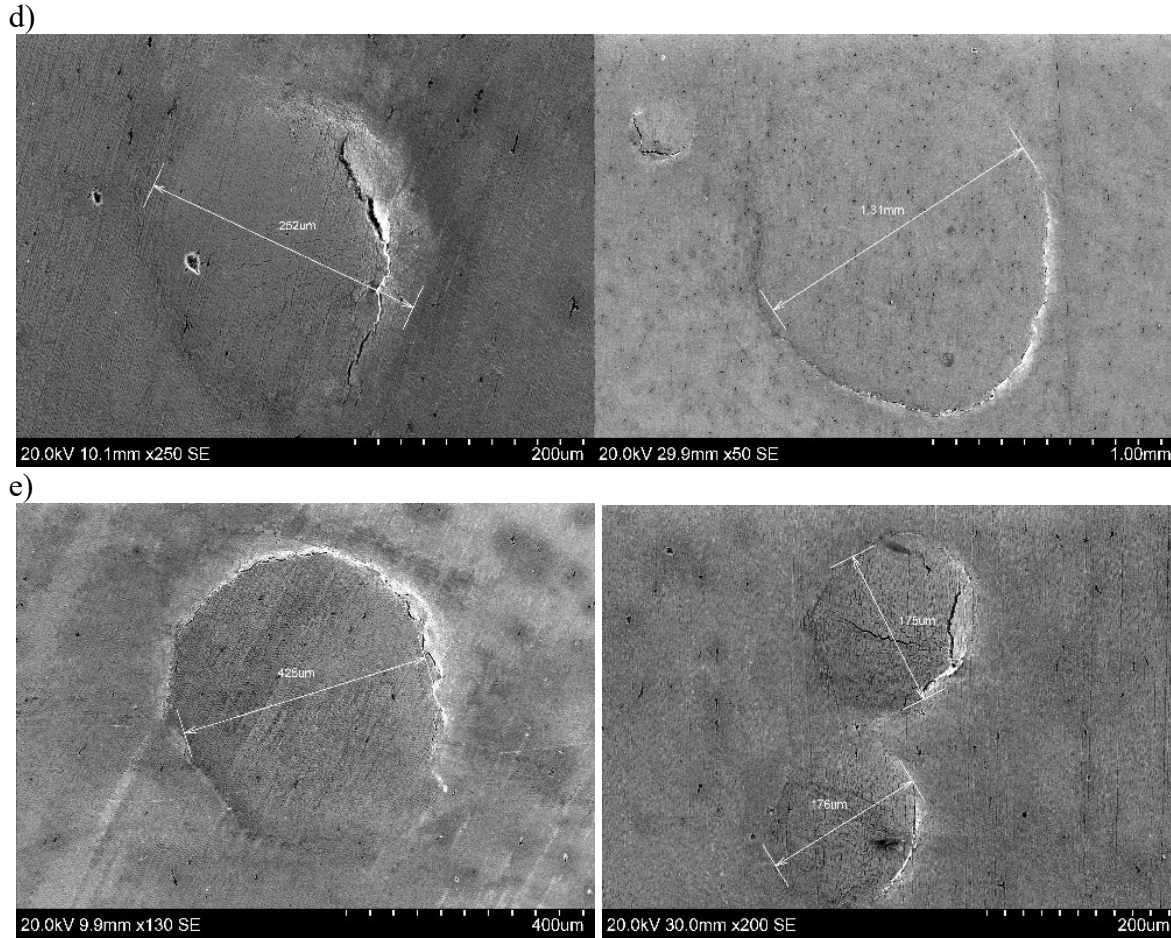


Figure 4.18. The examples of blisters on a) X70-1, b) X70-2-1, c) X70-2-2, d) X70-3-1, e) X70-3-2 surfaces. (Cont.)

Figure 4.18 shows that the different blisters with different shapes and diameters were formed after the hydrogen charging of the samples. The statistical analysis of blisters is presented in Table 4.4. In this table, the percentage of blisters on the surface is presented that pointed out the friction of the blister area to the whole exposed area of the samples. The length of cracking is the summation of all cracks length in the cross-section of the samples.

Table 4.4. Statistics of blisters and cracks on electrochemically charged samples.

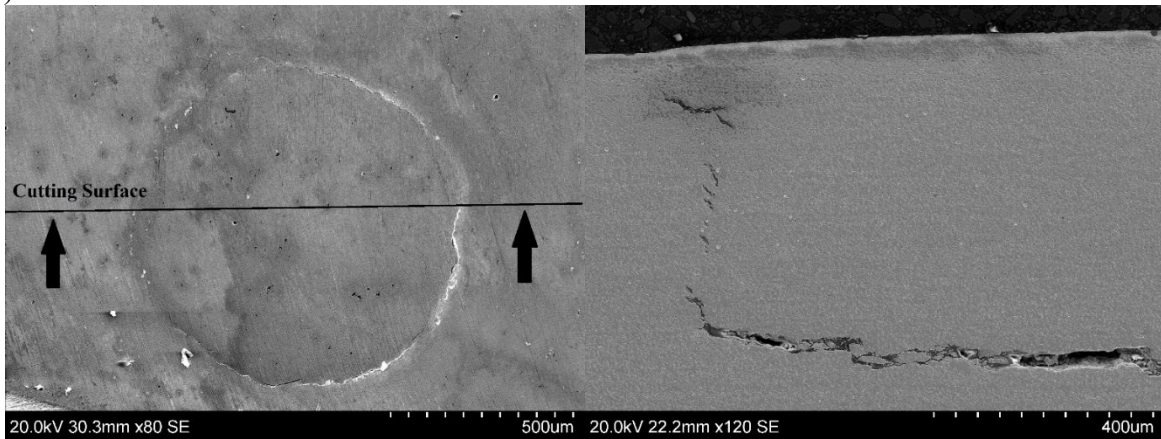
Pipe	Number of blisters on the top and bottom surfaces	Average Diameter of blisters (μm) $\pm 10\%$	Percentage of blisters on the surfaces (%) $\pm 10\%$	The length of cracking in cross-section (mm) $\pm 10\%$
X70-1	8	796	1.58	6.72
X70-2-1	19	892	3.54	11.32
X70-2-2	35	4230	19.74	21.15
X70-3-1	4	1061	1.48	6.48
X70-3-2	9	325	0.24	4.16

As mentioned in this table, the blisters on the X70-2-2 specimen surfaces consist of huge blisters, seen with the naked eyes, and some small blisters. The average diameter of these blisters

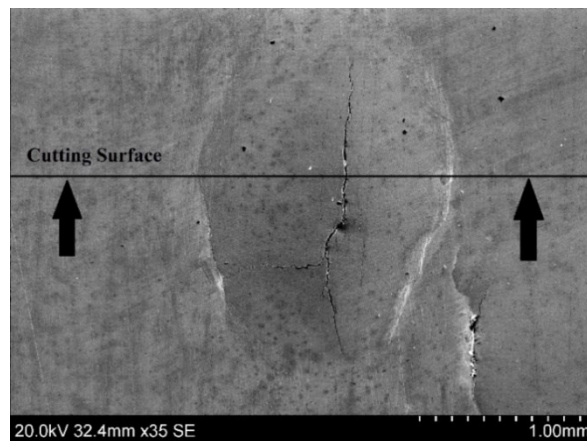
is 4.23 mm, which is significantly higher than the blisters' diameter formed on the other samples' surface. The least number of blisters formed in the X70-3-1 specimen with just four blisters on its surface, but the smallest blisters are found on the X70-3-2 specimens' surfaces with an average diameter of 325 microns and only 0.24% of the surface.

The samples' cross-section is used to characterize the HIC cracking of the samples. These cross-sections indicate the RD-ND surface of the steels. Thus, the samples are cut through their blisters to evaluate the samples' crack initiation and propagation sites. The statistical analysis of the cracks (Table 4.4) is done using these surfaces. Figure 4.19 is showing the cross-section of the X70-2-1, X70-2-2, and X70-3-2 specimens.

a)



b)



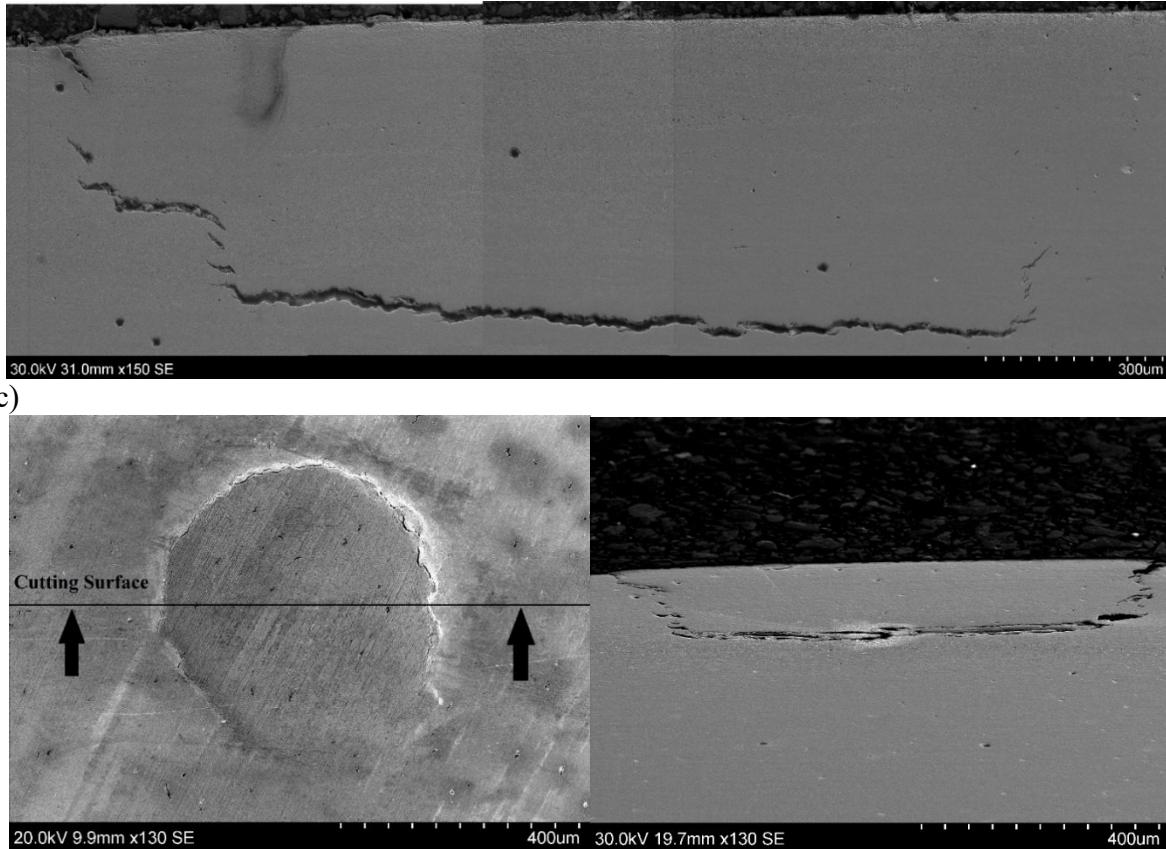


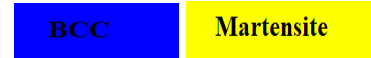
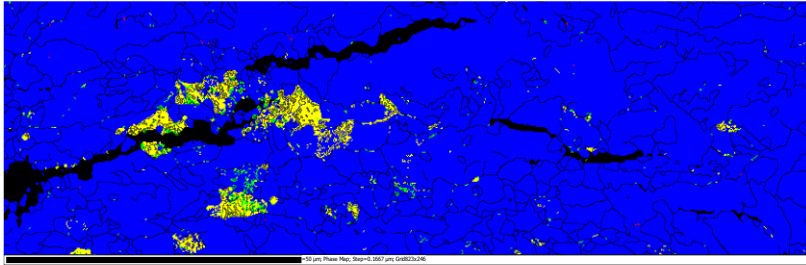
Figure 4.19. The examples of cracking on a) X70-2-1, b) X70-2-2 and c) X70-3-2 cross-sections.

Figure 4.19 presented some cracks that were formed underneath the blisters. Some other cracks on the cross-section of samples are considered in calculating the total length of cracks in Table 4.4 but are not shown here. X70-2-2 had the highest total crack length (21.15 mm) on its surfaces, while X70-3-2 had the lowest total crack length (4.16 mm).

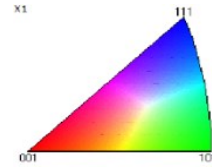
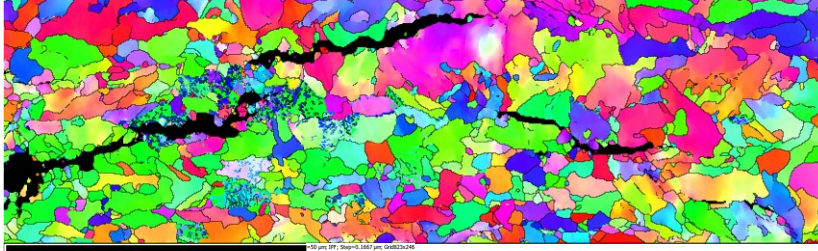
4.5 Texture characterization of the samples around the cracks

The pipeline steels in the service environment fail when the cracks initiate and propagate through the steel. Therefore, it is essential to understand the crack initiation sites and the factors that affect crack propagation. For this reason, the factors affecting crack initiation and propagation were observed in the cross-section of the samples. These factors include precipitates, inclusions, and texture. The texture and phase map of failed samples around the cracks are presented in Figures 4.20 to 4.24 for all samples. The legends in all photos are the same, and they are mentioned just in the first set of photos.

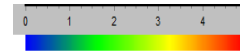
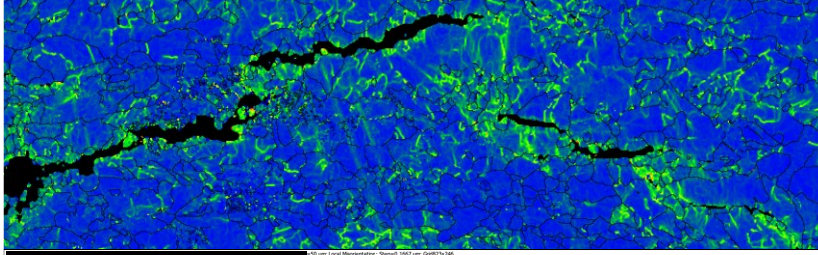
a) phase map



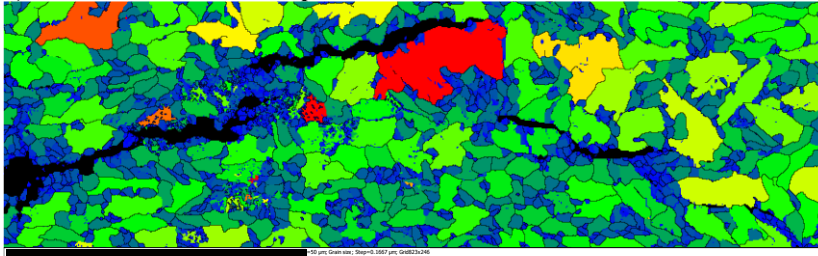
b) IPF map



c) Misorientation map



d) Grain size distribution map



e) Recrystallization fraction

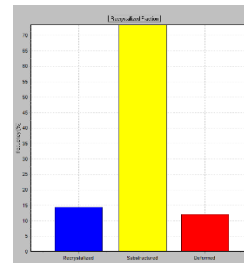
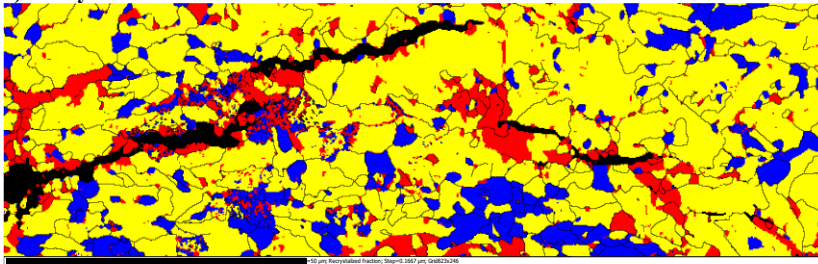
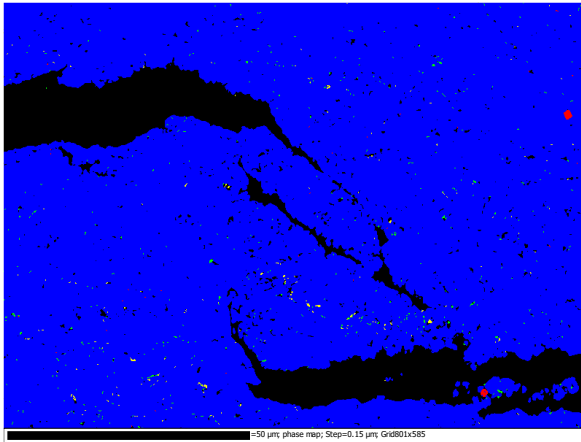
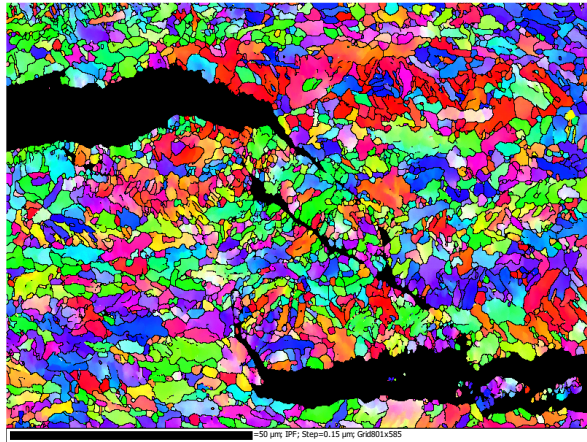


Figure 4.20. a) The phase map, b) IPF, c) Misorientation, d) Grain size and e) Recrystallization fraction of X70-1 around the crack.

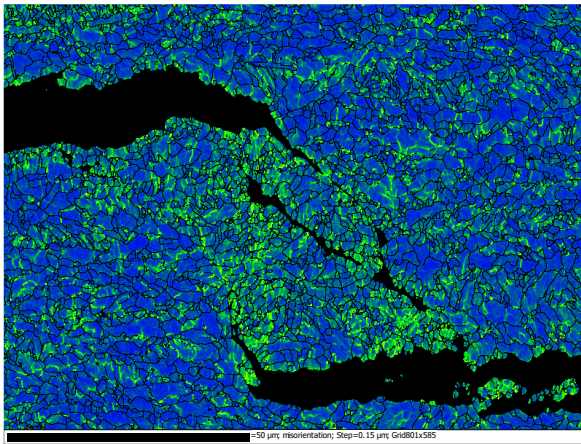
a) phase map



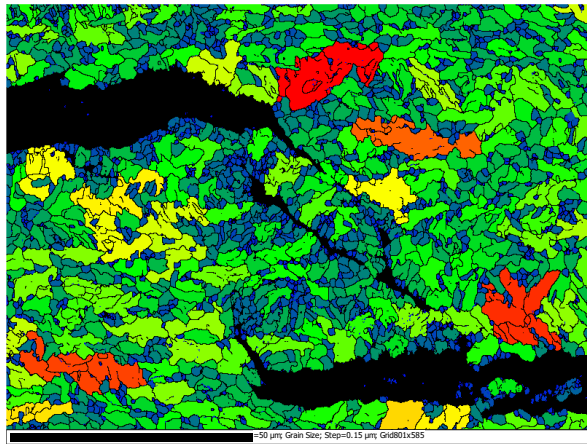
b) IPF map



c) Misorientation map



d) Grain size distribution map



e) Recrystallization fraction

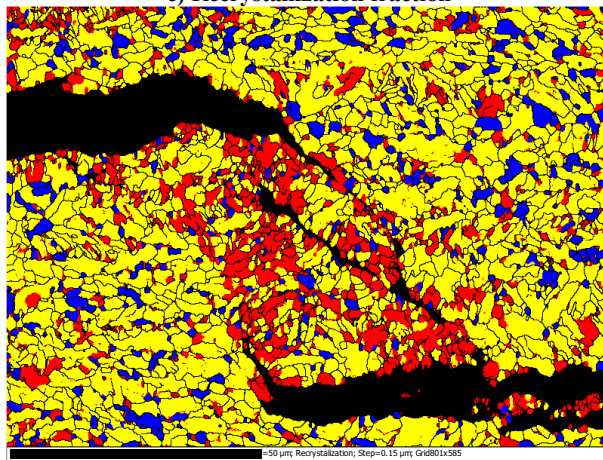
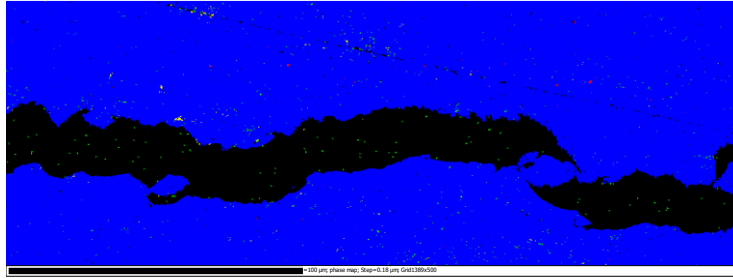
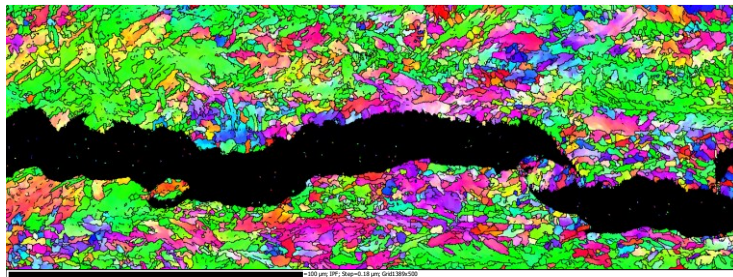


Figure 4.21. a) The phase map, b) IPF, c) Misorientation, d) Grain size and e) Recrystallization fraction of X70-2-1 around the crack.

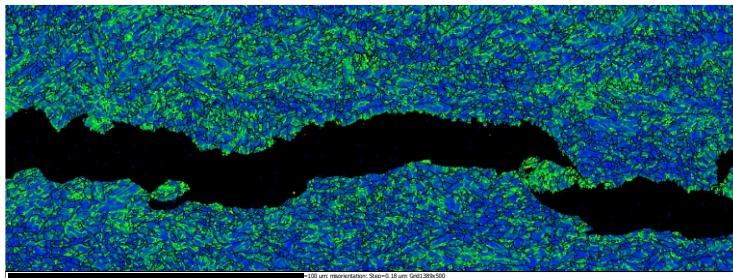
a) phase map



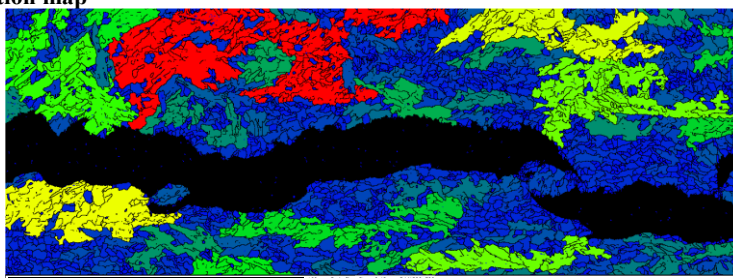
b) IPF map



c) Misorientation map



d) Grain size distribution map



e) Recrystallization fraction

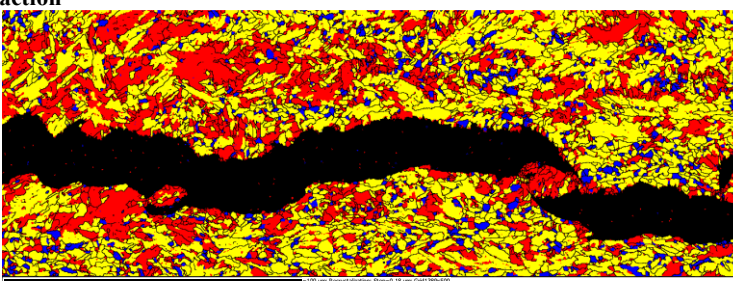
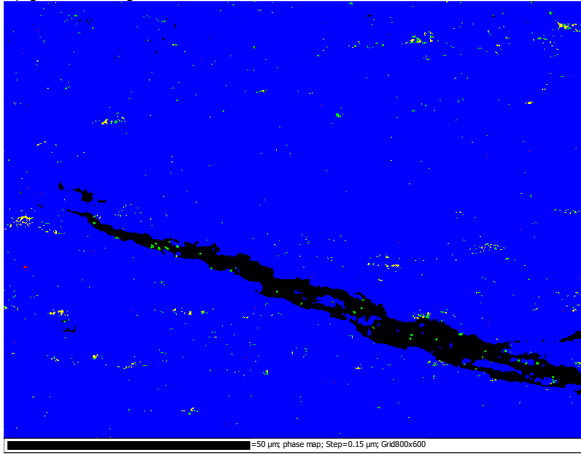
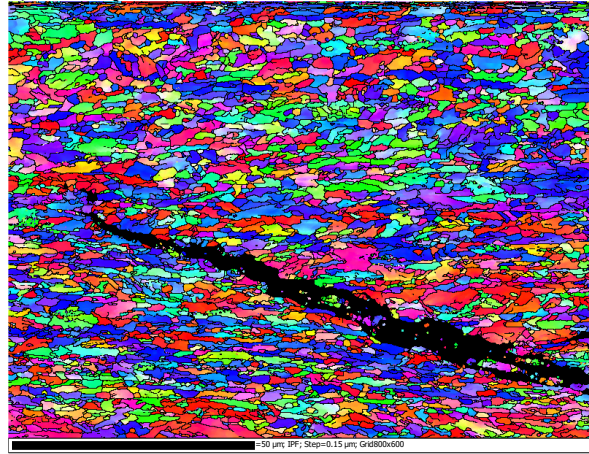


Figure 4.22. a) The phase map, b) IPF, c) Misorientation, d) Grain size and e) Recrystallization fraction of X70-2-2 around the crack.

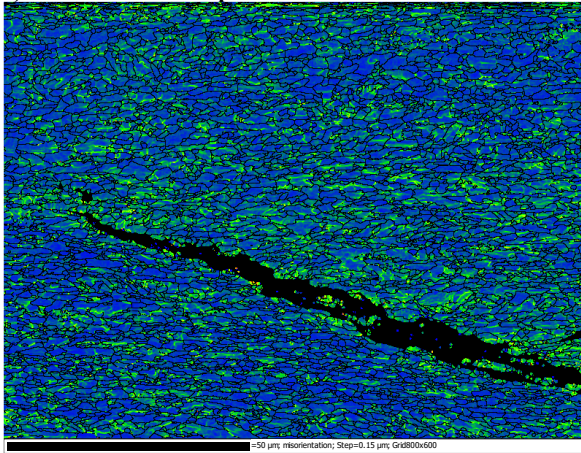
a) phase map



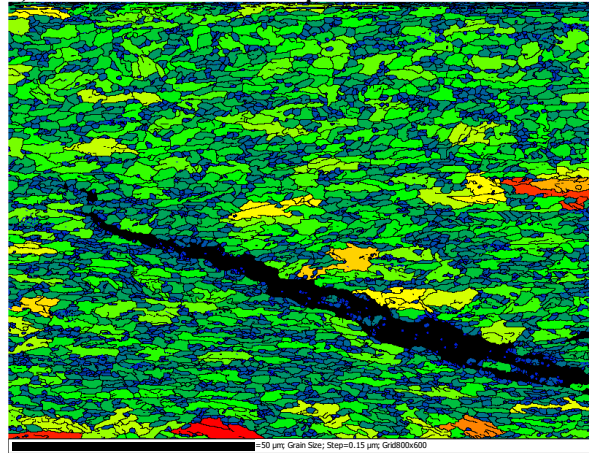
b) IPF map



c) Misorientation map



d) Grain size distribution map



e) Recrystallization fraction

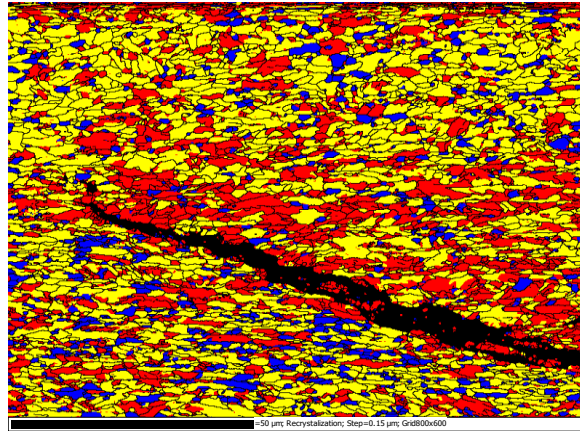
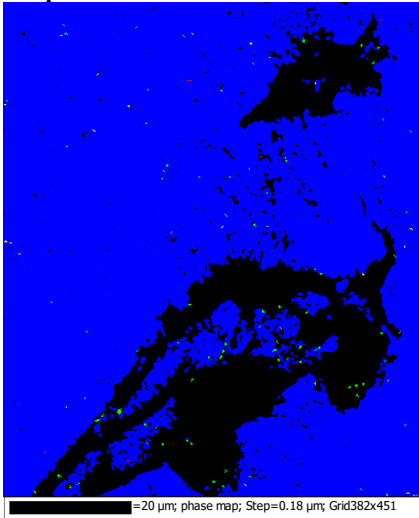
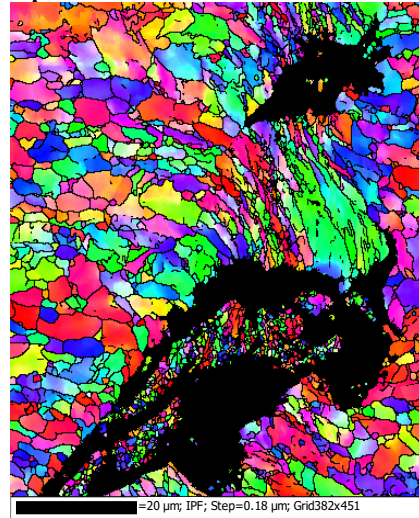


Figure 4.23. a) The phase map, b) IPF, c) Misorientation, d) Grain size and e) Recrystallization fraction of X70-3-1 around the crack.

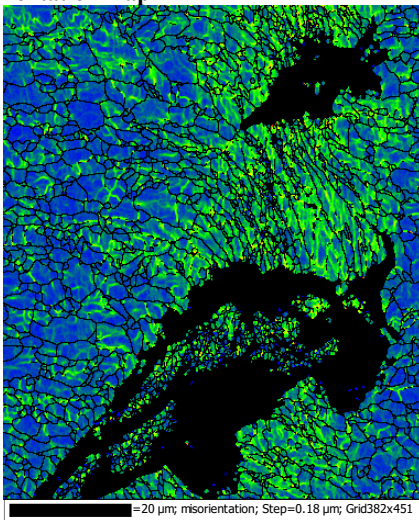
a) phase map



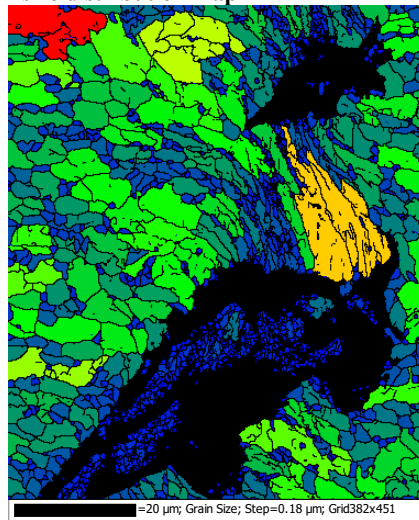
b) IPF map



c) Misorientation map



d) Grain size distribution map



e) Recrystallization fraction

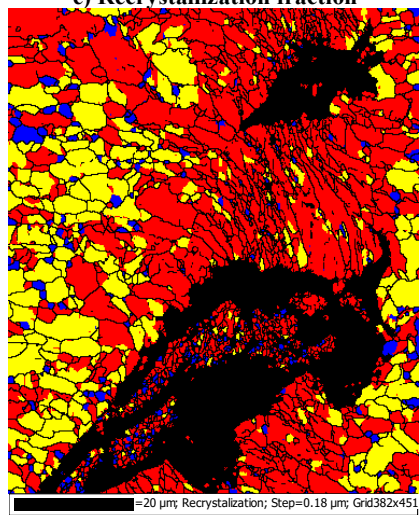


Figure 4.24. a) The phase map, b) IPF, c) Misorientation, d) Grain size and e) Recrystallization fraction of X70-3-2 around the crack.

The recrystallization fraction of specimens around the cracks is presented in Table 4.5. From the table below and recrystallized fraction photos, it can be concluded that the recrystallized grains are less than 15%, where the cracks are formed. The deformed grains are the largest fraction of grains in X70-3 specimens, while the substructured grains formed most of the grains in the other samples.

The phase map of all as received samples show BCC structure in the specimens (Figures 4.6 and 4.7), and the phase map of the specimens around the cracks show the same thing except for X70-1. In this sample, the martensite phase formed around 3% of all phases around the crack. This change was not due to the phase change, as the temperature was not changed. The reason was that the cracks tended to initiate and propagate through the martensite phases, and that was why a high amount of martensite phase was observed around the present cracks. The reason for propagation through the martensite phase relied on the lower closed packed density of martensite compared to the BCC structure, which allowed the hydrogen ions to be trapped. These hydrogen atoms make pressure, and the crack initiates at these phases.

Table 4.5. Recrystallization fraction of grains around the cracks.

Pipe	Deformed grains fraction (%)	Recrystallized grains fraction (%)
X70-1	12.2	14.6
X70-2-1	20.2	10.3
X70-2-2	37.6	8
X70-3-1	68.3	13.2
X70-3-2	63.4	5.6

From the maps, it seems the Kernel Local Misorientation (KLM) around the cracks ($\theta < 5^\circ$) have higher angles, although the angle of misorientations rarely exceeds 2.5° in all samples. A high KAM value means a high dislocation density [126]. Since dislocations are considered reversible traps for hydrogen atoms, they can facilitate hydrogen movement through the metal and propagate the cracks. Therefore, it is the reason why the value of KAM is high around the cracks.

The influence of the grain orientation on the mechanical properties and HIC resistance of steels is undeniable. According to the literature, the $\langle 111 \rangle \parallel \text{ND}$ oriented grains are highly HIC resistant, while $\langle 001 \rangle \parallel \text{ND}$ oriented grains make the steels more susceptible to the HIC [35, 36]. On the other hand, the $\langle 111 \rangle \parallel \text{ND}$ grains caused more ductility in the steels. The IPF map around the cracks indicates the mixing grain orientations around the cracks in all samples. By looking at the X70-2-2 sample IPF map, the lack of the $\langle 111 \rangle \parallel \text{ND}$ oriented grains around the crack is

apparent. The colour spectrums around the crack mostly consist of red (<001>||ND) and green (<101>||ND) colours. This shows the tendency of cracks to propagate through the <101>||ND and <001>||ND oriented grains when there are less <111>||ND oriented grains in the steel.

From the grains' orientation in the cracks' sides, it can also be concluded that the transgranular cracking has happened in all samples. The reason is the strong grain boundaries in ambient temperatures (in comparison with GB strength in high temperatures), which prevents the intergranular cracking.

4.6 Hydrogen permeation testing results

The permeation test is conducted for all samples according to what was explained in the permeation experimental procedure section at standard room temperature (23°C) and standard room pressure (1 atmosphere). The test results are presented in Table 4.6.

Table 4.6. Permeation test results.

Diffusion Parameters (grain size, μm)	Charging	Saturated current density $\pm 2\%$, I_{∞} (μA)	Time lag $\pm 10\%$, t_L (s)	Thickness, L (cm)	Permeability $\pm 2\%$, $J_{\infty} L \times 10^{-11}$ (mol/cm.s)	Effective Diffusivity $\pm 10\%$, $D_{eff} \times 10^{-6}$ (cm ² /s)	Apparent Solubility $\pm 10\%$, $C_{app} \times 10^{-6}$ (mol/cm ³)	Total density of traps $\times 10^{19}$ (cm ⁻³) $\pm 10\%$	Density of reversible traps $\times 10^{19}$ (cm ⁻³) $\pm 10\%$	Density of irreversible traps $\times 10^{19}$ (cm ⁻³) $\pm 10\%$
Top layer										
X70-1 (1.4)	First	94.32	3648	0.13	13.58	0.80	170.60	547.2	359.9	187.3
	Second	92.71	2986	0.13	13.35	0.97	137.26			
X70-2-1 (2.53)	First	80.33	2478	0.13	11.22	1.10	101.78	235.3	141.1	94.2
	Second	70.32	2053	0.13	9.82	1.33	73.82			
X70-2-2 (1.32)	First	97.80	2985	0.12	13.23	0.86	154.09	458.0	364.1	93.9
	Second	98.43	2654	0.12	13.31	0.97	137.88			
X70-3-1 (1.94)	First	102.9	2422	0.11	12.57	0.86	145.65	430.6	341.6	89.0
	Second	92.81	2272	0.11	11.34	0.92	123.22			
X70-3-2 (2.76)	First	91.56	1489	0.11	10.79	1.31	82.62	161.0	75.0	86.0
	Second	78.74	1098	0.11	9.28	1.77	52.39			
Middle layer										
X70-1 (2.68)	First	89.24	3988	0.23	12.27	0.66	184.86	712.2	120.5	591.7
	Second	78.5	1755	0.13	10.79	1.51	71.56			
X70-2-1 (2.71)	First	98.41	2492	0.13	13.42	1.05	128.40	313.1	76.8	236.3
	Second	91.68	1284	0.13	12.50	2.03	61.64			
X70-2-2 (2.31)	First	91.64	2396	0.10	9.90	0.68	145.16	544.1	164.4	379.7
	Second	85.67	1365	0.10	9.25	1.20	77.31			
X70-3-1 (2.2)	First	89.93	2565	0.11	10.99	0.82	134.80	422.2	272.3	149.9
	Second	79.95	2186	0.11	9.77	0.96	102.13			
X70-3-2 (3.28)	First	85.24	1583	0.11	10.04	1.23	81.77	169.4	57.0	112.4
	Second	64.92	1055	0.11	7.65	1.84	41.51			

Some important results can be gained from this table. First, by looking at the reversible traps in these samples, the direct relationship between the grain size and number of these traps is apparent. The highest amount of reversible traps (458) is for the X70-2-2 specimen at its top layer, which has the smallest grain size among all other samples (1.32 micron). On the other side, the least amount of reversible traps is for the X70-3-2 sample at its middle layer, in which the average grain size is 3.3 microns. Increasing the grain size will reduce the grain's boundaries and triple junctions, which count as the steels' main reversible traps.

By comparing the first and second polarization parameters, it is seen that the steady-state current and permeability of the first polarization is higher than the second one in all samples for both the middle and top layers. The reason relies on the presence of the irreversible traps inside the metal. The hydrogen atoms saturate these traps after the first polarization that reduced the steel's porosity for the second polarization. So, the distance travelled by the hydrogen atoms through the steel in second polarization increases that reduce the permeability.

From Table 4.6, it can be seen that the number of irreversible traps in the middle layer of all samples is significantly higher than their top layers. This is because of inclusions segregation in the middle of the sheets. The irreversible traps are counted as irreversible traps, and the hydrogen atoms trap in them for longer times.

Finally, the total number of traps in the middle layer of almost all samples are higher than their top layers. The reason is the higher impact of the presence of inclusions than the grain size. Although all samples' grain size is higher in their middle layer, that causes less reversible traps as the inclusions segregate in the middle layer of the sheets, the irreversible and total amount of traps are higher in this layer in all samples.

4.7 Results analysis

The test results presented in previous sections should have some logical relationship with each other and that we will try to explain in this section.

4.7.1 Effects of TMCP parameters on the microstructure, texture, and mechanical properties of the samples

According to the presented results, two of the TMCP parameters affected the samples' microstructure and texture. The first one is the rolling procedure of the samples. The mixture of

rough rolling and finish rolling is used in the rolling procedure of steel sheets. Our results show that finish rolling has more impact on the grain size of steels than rough rolling. For example, by holding other parameters constant, the steel produced with five rough and six finish rolling will have smaller grains than the one produced with six rough and five finish rolling. The second parameter in TMCP that influences the texture and microstructure of the steels is the cooling rate. Increasing the cooling rate forms smaller grains and the martensite phase in the steels. In our experiment, the X70-3-2 specimen formed with the least amount of finish rolling and the slowest cooling rate and had the largest grains. In contrast, X70-2-2 thickness was reduced mainly by finish rolling and the cooling rate was faster, and the result is a sheet with the smallest grain size. The highest cooling rate changed the phase of this specimen from ferrite to martensite. Higher number of finish rolling steps and higher cooling rate are creating the high angle misorientations and more deformed grains in the steels. In our samples, X70-3-2 and X70-2-2 have the lowest and the highest misorientation and deformed grains in their structures, respectively. On the other hand, X70-3-2 and X70-2-2 have the highest and the lowest numbers of recrystallized grains, respectively. As all samples were exposed to some rolling steps, their texture was very weak, so it is not possible to recognize any dominant microstructural orientation inside them.

The mechanical properties of the samples were directly affected by the TMCP parameters of the steels. The higher cooling rate and finish rolling steps result in smaller grains and higher hardness of the steels. The hardest specimen is X70-2-2 with 232 HV, while the softest one is X70-3-2 with 202 HV. The yield strength of the X70-2-2 specimen is the highest, too, with 578.5 MPa, while the yield strength of X70-3-2 is just 540.75 MPa.

The susceptibility of the steels to HIC is affected by the microstructure of steels too. By exposing the samples to an environment of hydrogen atoms, the X70-3-2 specimen with the largest grains and lowest mechanical strength shows the least cracks on its surfaces. This specimen is manufactured with the lowest number of steps of finish rolling and the lowest cooling rate. So, increasing the number of steps of finish rolling and cooling rate make the steel more susceptible to HIC cracking. One other consequence of a high cooling rate is creating the martensite phase, observed around the cracks. From our experiments, if the martensite phase exists in the structure, the cracking tends to propagate through this phase.

The permeation test results indicated that the X70-2-2 has more reversible traps, which is why there are more blisters and cracks on its surfaces. Higher reversible traps are due to smaller

grains. Taken together, these results suggest that the higher number of finish rolling steps and higher cooling rates will cause more reversible traps. From the other side, X70-3-2 has the smallest number of reversible and irreversible traps. The lower number of reversible traps is due to large grains and lower number of irreversible traps is related to fewer inclusions. It seems that the irreversible traps in steel's structure depend on the chemical composition, and that TMCP parameters do not have any effect on them. Only with proper TMCP, will the clusters' segregation be removed and the inclusions will be dispersed uniformly.

4.7.2 Effects of environmental conditions on the mechanical properties of specimens

The pipeline steel's service environment is a factor that defines the failure type of steels. According to our experiments on the X70-1 specimens, the sour environment causes the steels' brittle fracture. When the steel is exposed to the sour environments, the hydrogen atoms interfere with the dislocation movements, causing the hydrogen embrittlement. On the other hand, the acidic environment does not affect the mechanical properties of pipeline steels. According to our experiments, when there is any applied stress on the specimens, the steel's yield and ultimate strength are not changed in the acidic solutions.

EDS scan on the samples' fracture surface shows that the crack initiation and propagation are started from the sites full of Al_2O_3 and CaS inclusions. When the hydrogen atoms, which are trapped around these inclusions, release from these sites the cracks are initiated. So, the middle layer of the samples, where the inclusions segregate, is more susceptible to the HIC.

CHAPTER 5: CONCLUSION AND RECOMMENDATIONS

5.1 Overview

The first part of this chapter summarizes the effects of TMCP parameters on the microstructure, texture and mechanical properties of API X70 pipeline steels. The last part of the chapter includes the recommendations for future works based on the results of this research.

5.2 Conclusions

The deliverables and conclusions are presented separately. The findings include the analysis of the role of TMCP parameters on API X70 microstructure and texture. This evaluation has been conducted based on experiments on two batches of steels. The relationship between the microstructure and texture and mechanical properties and HIC resistance of steels (second objective) is presented in the next part of this chapter. The third part of this section outlines the evaluation of the effects of different service environments on API X70 mechanical properties (the third objective), based on the results obtained from one batch of pipeline steels.

Different TMCP parameters lead to different microstructure and texture in the specimens. The texture and microstructure of the samples were investigated and the relationship between texture and TMCP parameters are evaluated. These observations are concluded as below:

1- The microstructure of all samples consists of acicular and polygonal ferrite and a small amount of pearlite, mostly around the grain boundaries, except X70-2-2. In the X70-2-2 microstructure, the presence of martensite was apparent. The reason for such microstructure is the higher cooling rate used after hot rolling of this specimen. According to my experiments, the cooling rate of 62°C/s is associated with the martensite phase in the API X70 pipeline steels.

2- The IPF map of the samples in both middle and top layers shows that there is no dominant texture in the samples, and that the grains are distributed randomly. Therefore, it is possible to conclude that different TMCP parameters did not form any dominant grain orientation in our samples and the texture was very weak.

3- Different TMCP parameters and rolling processes generated different grain size, and grains were often elongated along the rolling direction. The X70-3-2 sample has the largest grains. The balance of total reduction between roughing and finishing rolling is of major interest in the steel's industry. According to the results, the finish rolling has a greater effect on the grain size

than the rough rolling. For instance, reducing the thickness using 7 roughing and 5 finishing steps leads to larger grains than reducing the thickness using 5 roughing and 7 finishing steps (all other parameters being constant). This conclusion is gained by comparing X70-2-1 and X70-2-2 specimens. The other conclusion is related to the total reduction steps. The higher number of total reduction steps, the smaller the grain size will be. In my samples, X70-3-2, with the lowest number of total and finishing reduction steps, has the largest grains.

4- Cooling rate is another factor that affects the grain size. A high cooling rate does not allow the grains to grow. With the cooling rate of 62 C/S, in addition to small grains, the martensite phase is formed.

5- Both high cooling rate and high number of finishing steps were related to higher misorientation angles in our samples. On the other side, the recrystallization fraction of microstructure decreases with increasing cooling rate and finish rolling steps.

6- By comparing the specimens' hardness, it is apparent that there is a direct relationship between the hardness and the grain size. The hardest specimen is X70-2-2 with 232 HV (with the smallest grain, 1.3 microns), while the softest one is X70-3-2 with 202 HV (with the largest grain size, 2.8 microns). The yield strength of the X70-2-2 specimen is the highest, too, with 578.5 MPa, while the yield strength of X70-3-2 is just 540.75 MPa. So, a higher cooling rate and higher number of finishing steps lead to higher hardness and strength in our investigated specimens.

The samples' HIC measurement gave some results, including the relationship between microstructural texture, TMCP parameters, mechanical properties, and HIC cracking. Our achievements are concluded at some point as below.

1- Increasing the grain size leads to better resistance of the steel to the HIC cracking. In our experiments, X70-3-2, which has the largest grains, shows the lowest cracking length and smallest blisters' diameter among all samples. On the other side, X70-2-2, which has the smallest grains, represents the longest total cracking length and the most blisters on its surfaces. The average diameter of blisters is highest in this specimen, too.

2- Martensite phase is not resistant to HIC cracking. According to our experiments, BCC microstructure is more resistant than martensite microstructure to HIC cracking in the sour environments. The propagation of cracks is often observed through the martensite phase.

3- Lower number of rolling steps and lower cooling rates in X70-3-2 specimen lead to better resistance of this steel to HIC cracking.

4- The X70-2-2 specimen with higher misorientation in its grain boundaries and more deformed grains is more susceptible to HIC cracking. This sample had more blisters and the longest total cracking length on its surfaces. On the other side, by investigating the cracking in all samples, it is seen that the cracks usually propagate through the deformed grains.

5- Although with changing the rolling procedure and TMCP parameters the texture of the samples remains low, it is possible to conclude that the HIC cracks do not tend to propagate through the $\langle 111 \rangle$ grains, and that the cracks propagate through the grains other than this orientation. This conclusion is derived from the observation of the orientation of grains around the cracks.

6- The transgranular cracking observed in the sour environment in all samples. The reason might be the strong grain boundaries in ambient temperatures (in comparison with GB strength in high temperatures), which prevents the intergranular cracking.

7- Steel containing reversible traps seems to be more susceptible to HIC cracking. In our samples, X70-2-2, which has a higher amount of reversible traps, has the worst resistance to HIC cracking. The reason for higher number of reversible traps in the X70-2-2 specimen is the smaller grain size in it. So, it is possible to conclude that more number of finish rolling steps and faster cooling rate will increase number of reversible traps and facilitate HIC cracking.

The effects of the different service environments on the mechanical properties of X70-1 specimen are investigated and the parameters affect the failure of steels in these environments are studied. The conclusion of my achievements is presented below.

1- The acidic environment does not have any immediate effect on the mechanical properties of steels. The stress-strain diagram of steel tested in an acidic environment shows that the strength and type of failure are similar to atmospheric conditions.

2- Exposing the samples to an environment full of hydrogen will cause hydrogen embrittlement in the steels. In this condition, the brittle failure of steel was seen under the applied stresses.

3- Using EDS scanning on the samples' fractured surface, it seems that the cracks initiate from Al_2O_3 and CaS inclusions.

4- The hydrogen environment does not have permanent effects on the mechanical properties of the investigated specimens. In ex-situ experiments, the yield and ultimate strength of the samples were the same as the samples were tested under atmospheric conditions. The only

difference was the failure point between these samples. The results indicated that the samples were had initial charging before tensile testing had lower fracture toughness.

5- After the hydrogen charging of the samples, the hardness of them increased by 2-8%. The highest increment was observed for X70-3-2 (7.9% of the increase) that has the largest grains. A very low increment was observed for X70-2-2 (2.5% of the increase), which has the smallest grains. The hardness of specimens with larger grains (after charging) was increased more than the specimens with smaller grains. The grain refinement seems to improve the resistance to hydrogen embrittlement.

5.3 Recommendations for future researches

This thesis helps to understand better the effects of different TMCP parameters and rolling procedures on steels' microstructure and HIC resistance and the effects of different environmental conditions. However, some potential areas are identified for future research on the HIC resistance of steels. Also, additional efforts can be made to increase the experiments' accuracy.

5.3.1 Potential areas for the future researches

1- The balance between rough and finish rolling should be investigated to find the optimum number of each step to have both HIC resistance and higher mechanical properties in API X70 pipeline steels by changing the microstructure.

2- The effects of adding different chemical compositions like Nb on HIC resistance of pipeline steels can be investigated.

3- The methods to manufacture texture in the steels should be investigated.

5.3.2 Suggested improvements to experimental setup

1- First, it should be follow up by the next researcher to get permission from the department to use H₂S gas inside the laboratories with all cautious and safety requirements. Using H₂S gas, the students can perform the tests according to the NACE standards.

2- The permeation test setup should be changed as in this setup, the hydrogen bubble is created in the charging cell, causing fluctuation in the cathodic current. The power supplier type should be changed to a potentiostat. The current power supplier does not have a feedback system

and the user should adjust the input current manually and continuously during the test, which is about 12 hours.

3- The tensile testing machine's clamps should be designed and changed. The current one is susceptible to the thickness of the samples and if the thickness has a 0.1 mm differential with its sketch, it is not possible to put the sample between the clamps. The other problem is related to taking samples out of the clamps after hydrogen charging as the samples' thickness becomes a little larger after hydrogen charging.

REFERENCES

- [1] Canadian Association of Petroleum Producers (CAPP), “2018 Economic Report,” 2018. [Online]. Available: https://www.capp.ca/wp-content/uploads/2019/11/CAPP_2018_Economic_Report_Series_Leveraging_Opportunities_Diversifying_Canada_s_Oil_and_Natural_Gas_Market-333595.pdf.
- [2] T. Nace, L. Plante, and J. Browning, “Global Energy Monitor ‘Pipeline Bubble,’” 2019. https://globalenergymonitor.org/wp-content/uploads/2019/04/GFITPipelineBubble_2019_v6.pdf.
- [3] Enbridge, “Enbridge Quick Facts,” 2020. <https://www.enbridge.com/media-center/enbridge-quick-facts>.
- [4] “Natural Resources Canada, Frequently Asked Questions (FAQs) Concerning Federally-Regulated Petroleum Pipelines in Canada,” 2020. <https://www.nrcan.gc.ca/our-natural-resources/energy-sources-distribution/clean-fossil-fuels/pipelines/faqs-federally-regulated-petroleum-pipelines-canada/5893#h-2-1>.
- [5] G. Koch, J. Varney, N. Thompson, O. Moghissi, M. Gould, and J. Payer, “NACE 2016 impact study,” 2016.
- [6] R. L. Sutherby, “CEPA report on circumferential stress corrosion cracking,” in *Proceedings of the International Pipeline Conference, IPC*, 1998.
- [7] “Safety of Gas Gathering Pipelines, PHMSA report,” 2019.
- [8] R. Rihan, B. Al-Wakaa, N. Tanoli, and H. Shalaby, “The susceptibility of P110 downhole tubular steel to sulfide stress cracking in H₂S and NaCl,” *J. Pet. Sci. Eng.*, vol. 174, no. September 2018, pp. 1034–1041, 2019, doi: 10.1016/j.petrol.2018.10.102.
- [9] M. Elboujdaini and R. W. Revie, “Metallurgical factors in stress corrosion cracking (SCC) and hydrogen-induced cracking (HIC),” *J. Solid State Electrochem.*, 2009, doi: 10.1007/s10008-009-0799-0.
- [10] NEB (National Energy Board), *Stress Corrosion Cracking on Canadian Oil and Gas Pipelines, Report of the Inquiry*. 1996.
- [11] B. Y. Fang, A. Atrens, J. Q. Wang, E. H. Han, Z. Y. Zhu, and W. Ke, “Review of stress corrosion cracking of pipeline steels in ‘low’ and ‘high’ pH solutions,” *J. Mater. Sci.*, vol. 38, no. 1, pp. 127–132, 2003, doi: 10.1023/A:1021126202539.
- [12] R. N. Parkins, “A review of stress corrosion cracking of high pressure gas pipelines,” in *NACE - International Corrosion Conference Series*, 2000, doi: 10.1002/maco.201508454.
- [13] R. N. Parkins, “Mechanistic aspects of intergranular stress corrosion cracking of ferritic steels,”

- Corros.*, 1996, doi: 10.5006/1.3292124.
- [14] M. Yunovich, Z. Xia, and Z. Szklarska-Smialowska, “Factors influencing stress corrosion cracking of carbon steel in diluted bicarbonate environments,” *Corrosion*, vol. 54, no. 2, pp. 155–161, 1998, doi: 10.5006/1.3284839.
- [15] R. Kodým, D. Šnita, V. Fíla, K. Bouzek, and M. Kouřil, “Investigation of processes occurring at cathodically protected underground installations: Experimental study of pH alteration and mathematical modeling of oxygen transport in soil,” *Corros. Sci.*, 2017, doi: 10.1016/j.corsci.2016.12.003.
- [16] M. C. Yan, J. Q. Wang, E. H. Han, and W. Ke, “Electrochemical measurements using combination microelectrode in crevice simulating disbonded of pipeline coatings under cathodic protection,” *Corros. Eng. Sci. Technol.*, 2007, doi: 10.1179/174327807X159934.
- [17] M. Yan, J. Wang, E. Han, and W. Ke, “Local environment under simulated disbonded coating on steel pipelines in soil solution,” *Corros. Sci.*, 2008, doi: 10.1016/j.corsci.2008.01.004.
- [18] F. Gan, Z. W. Sun, G. Sabde, and D. T. Chin, “Cathodic protection to mitigate external corrosion of underground steel pipe beneath disbonded coating,” *Corrosion*, 1994, doi: 10.5006/1.3293470.
- [19] Z. F. Wang and A. Atrens, “Initiation of stress corrosion cracking for pipeline steels in a carbonate-bicarbonate solution,” *Metall. Mater. Trans. A Phys. Metall. Mater. Sci.*, vol. 27, no. 9, pp. 2686–2691, 1996, doi: 10.1007/BF02652362.
- [20] T. K. Christman, “Relationship between pitting, stress, and stress corrosion cracking of line pipe steels,” *Mater. Perform.*, vol. 30, no. 10, pp. 23–27, 1991.
- [21] J. A. Beavers and B. A. Harle, “Mechanisms of high-pH and near-neutral-pH SCC of underground pipelines,” *J. Offshore Mech. Arct. Eng.*, 2002, doi: 10.1115/1.1376716.
- [22] R. N. Parkins, E. Belhimer, and W. K. Blanchard, “Stress-corrosion cracking characteristics of a range of pipeline steels in carbonate-bicarbonate solution,” *Corrosion*, vol. 49, no. 12, pp. 951–966, 1993, doi: 10.5006/1.3316023.
- [23] H. Asahi, “Role of microstructures on stress corrosion cracking of pipeline steels in carbonate-bicarbonate solution,” *Corrosion*, vol. 55, no. 7, pp. 644–652, 1999, doi: 10.5006/1.3284018.
- [24] T. Kushida *et al.*, “Effects of metallurgical factors and test conditions on near neutral pH SCC of pipeline steels,” in *Corrosion*, 2001, p. 1213.
- [25] L. W. Wang, C. W. Du, Z. Y. Liu, X. H. Wang, and X. G. Li, “Influence of carbon on stress corrosion cracking of high strength pipeline steel,” *Corros. Sci.*, 2013, doi: 10.1016/j.corsci.2013.06.051.
- [26] H. M. Nykyforchyn, S. F. Savula, G. Gabetta, V. M. Tsependa, and O. I. Zvirko, “Stress corrosion cracking of gas pipeline steels of different strength,” *Procedia Struct. Integr.*, vol. 2, pp. 509–516, 2016, doi: 10.1016/j.prostr.2016.06.066.

- [27] Z. Fan, X. Hu, J. Liu, H. Li, and J. Fu, "Stress corrosion cracking of L360NS pipeline steel in sulfur environment," *Petroleum*, vol. 3, no. 3, pp. 377–383, 2017, doi: 10.1016/j.petlm.2017.03.006.
- [28] M. A. Arafin and J. A. Szpunar, "A novel microstructure - Grain boundary character based integrated modeling approach of intergranular stress corrosion crack propagation in polycrystalline materials," *Comput. Mater. Sci.*, vol. 47, no. 4, pp. 890–900, 2010, doi: 10.1016/j.commatsci.2009.11.020.
- [29] M. C. Zhao, M. Liu, A. Atrens, Y. Y. Shan, and K. Yang, "Effect of applied stress and microstructure on sulfide stress cracking resistance of pipeline steels subject to hydrogen sulfide," *Mater. Sci. Eng. A*, 2008, doi: 10.1016/j.msea.2007.05.067.
- [30] B. T. Lu and J. L. Luo, "Relationship between yield strength and near-neutral pH stress corrosion cracking resistance of pipeline steels - An effect of microstructure," *Corrosion*, 2006, doi: 10.5006/1.3278258.
- [31] Y. F. Cheng, "Analysis of electrochemical hydrogen permeation through X-65 pipeline steel and its implications on pipeline stress corrosion cracking," *Int. J. Hydrogen Energy*, 2007, doi: 10.1016/j.ijhydene.2006.07.018.
- [32] M. A. Arafin and J. A. Szpunar, "A new understanding of intergranular stress corrosion cracking resistance of pipeline steel through grain boundary character and crystallographic texture studies," *Corros. Sci.*, 2009, doi: 10.1016/j.corsci.2008.10.006.
- [33] A. King, G. Johnson, D. Engelberg, W. Ludwig, and J. Marrow, "Observations of intergranular stress corrosion cracking in a grain-mapped polycrystal," *Science (80-.)*, vol. 321, no. 5887, pp. 382–385, 2008, doi: 10.1126/science.1156211.
- [34] A. Kawashima, K. Hashimoto, and S. Shimodaira, "hydrogen electrode reaction and hydrogen embrittlement of mild steel in hydrogen sulfide solutions," *Corrosion*, 1976, doi: 10.5006/0010-9312-32.8.321.
- [35] J. F. Newman and L. L. Shreir, "Role of hydrides in hydrogen entry into steel from solutions containing promoters," *Corros. Sci.*, 1969, doi: 10.1016/S0010-938X(69)80117-4.
- [36] NACE TM-0177, "Laboratory testing of metals for resistance to sulfide stress cracking and stress corrosion cracking in H₂S environments," *NACE International*. 2005.
- [37] M. Al-Mansour, A. M. Alfantazi, and M. El-boujdaini, "Sulfide stress cracking resistance of API-X100 high strength low alloy steel," *Mater. Des.*, vol. 30, no. 10, pp. 4088–4094, 2009, doi: 10.1016/j.matdes.2009.05.025.
- [38] S. Koh, H. M. Hung, K. Y. Kim, and B. Y. Yang, "Effect of Cr and Mo on susceptibility to sulfide stress cracking of API X70 grade line pipe steels," *Corros. 2004*, no. March, pp. 244–253, 2004.
- [39] K. Ume, T. Taira, T. Hyodo, and Y. Kobayashi, "Initiation and propagation morphology of sulphide

- stress corrosion cracking at welds on linepipe steels,” in *NACE Corrosion/85*, 1985, p. paper 240.
- [40] NACE International, “Petroleum and natural gas industries — Materials for use in H₂S-containing environments in oil and gas production — Part 1 : General principles for selection of cracking-resistant materials,” *ANSI/NACE MR0175/ISO 15156-1:2009*, 2009.
- [41] A. Barnoush, “Hydrogen embrittlement, revisited by in situ electrochemical nanoindentation,” Universität des Saarlandes, 2007.
- [42] T. Michler and J. Naumann, “Influence of high pressure hydrogen on the tensile and fatigue properties of a high strength Cu-Al-Ni-Fe alloy,” *Int. J. Hydrogen Energy*, vol. 35, no. 20, pp. 11373–11377, Oct. 2010, doi: 10.1016/j.ijhydene.2010.07.093.
- [43] C. A. Zapffe and C. E. Sims, “Hydrogen embrittlement, internal stress and defects in steels,” *Met. Technol.*, pp. 1–37, 1941, [Online]. Available: <http://www.scopus.com/inward/record.url?eid=2-s2.0-0006938317&partnerID=tZOtx3y1>.
- [44] C. D. Beachem, “A new model for hydrogen-assisted cracking (hydrogen ‘embrittlement’),” *Metall. Trans.*, 1972, doi: 10.1007/BF02642048.
- [45] R. A. Oriani and P. H. Josephic, “Hydrogen-enhanced load relaxation in a deformed medium-carbon steel,” *Acta Metall.*, 1979, doi: 10.1016/0001-6160(79)90187-1.
- [46] M. A. Mohtadi-Bonab, J. A. Szpunar, R. Basu, and M. Eskandari, “The mechanism of failure by hydrogen induced cracking in an acidic environment for API 5L X70 pipeline steel,” *Int. J. Hydrogen Energy*, vol. 40, no. 2, pp. 1096–1107, 2015, doi: 10.1016/j.ijhydene.2014.11.057.
- [47] R. Pourazizi, M. A. Mohtadi-Bonab, and J. A. Szpunar, “Investigation of different failure modes in oil and natural gas pipeline steels,” *Eng. Fail. Anal.*, vol. 109, p. 104400, Jan. 2020, doi: 10.1016/J.ENGFAILANAL.2020.104400.
- [48] National Association of Corrosion Engineers, “TM0284 Standard test method: evaluation of pipeline and pressure vessel steels for resistance to hydrogen-induced cracking,” 2011.
- [49] H. M. Ha, J. H. Ai, and J. R. Scully, “Effects of prior cold work on hydrogen trapping and diffusion in API X-70 line pipe steel during electrochemical charging,” *Corrosion*, vol. 70, no. 2, pp. 166–184, Feb. 2014, doi: 10.5006/0990.
- [50] F. G. Wei and K. Tsuzaki, “Hydrogen absorption of incoherent TiC particles in iron from environment at high temperatures,” *Metall. Mater. Trans. A Phys. Metall. Mater. Sci.*, vol. 35 A, no. 10, pp. 3155–3163, 2004, doi: 10.1007/s11661-004-0060-5.
- [51] T. Zakroczymski, “Permeability of iron to hydrogen cathodically generated in 0.1 M NaOH,” *Scr. Metall.*, vol. 19, pp. 521–524, 1985.
- [52] V. Venegas, F. Caleyó, T. Baudin, J. H. Espina-Hernández, and J. M. Hallen, “On the role of crystallographic texture in mitigating hydrogen-induced cracking in pipeline steels,” *Corros. Sci.*,

- 2011, doi: 10.1016/j.corsci.2011.08.031.
- [53] S. Wang, M. L. Martin, P. Sofronis, S. Ohnuki, N. Hashimoto, and I. M. Robertson, "Hydrogen-induced intergranular failure of iron," *Acta Mater.*, 2014, doi: 10.1016/j.actamat.2014.01.060.
- [54] H. Asahi, D. Hiramami, and S. Yamasaki, "Hydrogen trapping behavior in vanadium-added steel," *ISIJ Int.*, 2008, doi: 10.2355/isijinternational.43.527.
- [55] A. Griesche, E. Dabah, T. Kannengiesser, N. Kardjilov, A. Hilger, and I. Manke, "Three-dimensional imaging of hydrogen blister in iron with neutron tomography," *Acta Mater.*, 2014, doi: 10.1016/j.actamat.2014.06.034.
- [56] S. Yamasaki and H. K. D. H. Bhadeshia, "M₄C₃ precipitation in Fe-C-Mo-V steels and relationship to hydrogen trapping," *Proc. R. Soc. A Math. Phys. Eng. Sci.*, 2006, doi: 10.1098/rspa.2006.1688.
- [57] M. F. Stevens and I. M. Bernstein, "Microstructural trapping effects on hydrogen induced cracking of a microalloyed steel," *Metall. Trans. A*, 1989, doi: 10.1007/BF02651657.
- [58] H. B. Xue and Y. F. Cheng, "Characterization of inclusions of X80 pipeline steel and its correlation with hydrogen-induced cracking," *Corros. Sci.*, 2011, doi: 10.1016/j.corsci.2010.12.011.
- [59] M. A. Mohtadi-Bonab, M. Eskandari, and J. A. Szpunar, "Texture, local misorientation, grain boundary and recrystallization fraction in pipeline steels related to hydrogen induced cracking," *Mater. Sci. Eng. A*, vol. 620, pp. 97–106, 2014, doi: 10.1016/j.msea.2014.10.009.
- [60] Y. Kobayashi and Z. Szklarska-Smialowska, "A study of the hydrogen-induced degradation of two steels differing in sulfur content," *Metall. Trans. A*, 1986, doi: 10.1007/BF02645923.
- [61] V. P. Ramunni, T. D. P. Coelho, and P. E. V de Miranda, "Interaction of hydrogen with the microstructure of low-carbon steel," *Mater. Sci. Eng. A*, 2006, doi: 10.1016/j.msea.2006.07.089.
- [62] F. G. Wei, T. Hara, T. Tsuchida, and K. Tsuzaki, "Hydrogen Trapping in Quenched and Tempered 0.42C-0.30Ti Steel Containing Bimodally Dispersed TiC Particles," *ISIJ Int.*, 2008, doi: 10.2355/isijinternational.43.539.
- [63] G. H. Yu, Y. H. Cheng, L. Chen, L. J. Qiao, Y. B. Wang, and W. Y. Chu, "Hydrogen accumulation and hydrogen-induced cracking of API C90 tubular steel," *Corros.*, 1997, doi: 10.5006/1.3290260.
- [64] D. Perez Escobar, K. Verbeken, L. Duprez, and M. Verhaege, "Experimental evaluation of the hydrogen distribution in steel by thermal desorption spectroscopy," *Petros Sofron.*, 2009.
- [65] R. F. Schaller and J. R. Scully, "Measurement of effective hydrogen diffusivity using the Scanning Kelvin Probe," *Electrochem. commun.*, 2014, doi: 10.1016/j.elecom.2013.12.025.
- [66] W. K. Kim, S. U. Koh, B. Y. Yang, and K. Y. Kim, "Effect of environmental and metallurgical factors on hydrogen induced cracking of HSLA steels," *Corros. Sci.*, 2008, doi: 10.1016/j.corsci.2008.09.030.
- [67] J. L. Gonzalez, R. Ramirez, J. M. Hallen, and R. A. Guzman, "Hydrogen-Induced Crack Growth

- Rate in Steel Plates Exposed to Sour Environments,” *Corros.*, 1997, doi: 10.5006/1.3290278.
- [68] K. O. Angus, G. R.; Martins, G. P.; Speer, J. G.; Matlock, D. K.; Findley, “Characterization of an electrolytic charging method to assess hydrogen-induced damage in pipeline steels,” in *Steely Hydrogen Conference Proceedings*, 2014, pp. 291–301.
- [69] ISE/NFE/8, *Method of measurement of hydrogen permeation and determination of hydrogen uptake and transport in metals by an electrochemical technique. ISO/FDIS 17081:2013(E)*. 2013.
- [70] F. Huang, X. G. Li, J. Liu, Y. M. Qu, J. Jia, and C. W. Du, “Hydrogen-induced cracking susceptibility and hydrogen trapping efficiency of different microstructure X80 pipeline steel,” *J. Mater. Sci.*, 2011, doi: 10.1007/s10853-010-4799-3.
- [71] C. F. Dong, K. Xiao, Z. Y. Liu, W. J. Yang, and X. G. Li, “Hydrogen induced cracking of X80 pipeline steel,” *Int. J. Miner. Metall. Mater.*, 2010, doi: 10.1007/s12613-010-0360-2.
- [72] K. O. Findley, M. K. O’Brien, and H. Nako, “Critical assessment 17: Mechanisms of hydrogen induced cracking in pipeline steels,” *Mater. Sci. Technol. (United Kingdom)*, vol. 31, no. 14, pp. 1673–1680, 2015, doi: 10.1080/02670836.2015.1121017.
- [73] P. Castaño Rivera, V. P. Ramunni, and P. Bruzzoni, “Hydrogen trapping in an API 5L X60 steel,” *Corros. Sci.*, 2012, doi: 10.1016/j.corsci.2011.09.008.
- [74] D. Li, R. P. Gangloff, and J. R. Scully, “Hydrogen trap states in ultrahigh-strength AERMET 100 steel,” *Metall. Mater. Trans. A Phys. Metall. Mater. Sci.*, 2004, doi: 10.1007/s11661-004-0011-1.
- [75] M. A. Mohtadi-Bonab, J. A. Szpunar, and S. S. Razavi-Tousi, “A comparative study of hydrogen induced cracking behavior in API 5L X60 and X70 pipeline steels,” *Eng. Fail. Anal.*, vol. 33, pp. 163–175, 2013, doi: 10.1016/j.engfailanal.2013.04.028.
- [76] R. L. S. Thomas, D. Li, R. P. Gangloff, and J. R. Scully, “Trap-governed hydrogen diffusivity and uptake capacity in ultrahigh-strength AERMET 100 steel,” *Metall. Mater. Trans. A Phys. Metall. Mater. Sci.*, 2002, doi: 10.1007/s11661-002-0032-6.
- [77] A. Kumar, “Mechanism of failure of pipeline steels in sour environment,” in *International Conference on Material Science and Condensed Matter Physics*, 2015.
- [78] D. Hejazi *et al.*, “Effect of manganese content and microstructure on the susceptibility of X70 pipeline steel to hydrogen cracking,” *Mater. Sci. Eng. A*, vol. 551, pp. 40–49, 2012, doi: 10.1016/j.msea.2012.04.076.
- [79] K. Ushijima, Y. Sugitani, S. Yamaguchi, S. Shiode, M. Hashio, and H. Tomono, “The technology of continuous casting for the application of HSLA steels,” in *Int. Conf. on HSLA Steels Technology and Application (Materials Park, OH: ASM International)*, 1984, p. 403.
- [80] J. Moon, S. J. Kim, and C. Lee, “Role of Ca treatment in hydrogen induced cracking of hot rolled API pipeline steel in acid sour media,” *Met. Mater. Int.*, 2013, doi: 10.1007/s12540-013-1008-3.

- [81] S. M. Lee and J. Y. Lee, "The effect of the interface character of TiC particles on hydrogen trapping in steel," *Acta Metall.*, 1987, doi: 10.1016/0001-6160(87)90268-9.
- [82] M. Garet, A. M. Brass, C. Haut, and F. Guttierez-Solana, "Hydrogen trapping on non metallic inclusions in Cr-Mo low alloy steels," *Corros. Sci.*, 1998, doi: 10.1016/S0010-938X(98)00008-0.
- [83] A. J. Haq, K. Muzaka, D. P. Dunne, A. Calka, and E. V. Pereloma, "Effect of microstructure and composition on hydrogen permeation in X70 pipeline steels," *Int. J. Hydrogen Energy*, 2013, doi: 10.1016/j.ijhydene.2012.11.127.
- [84] S. K. Yen and I. B. Huang, "Critical hydrogen concentration for hydrogen-induced blistering on AISI 430 stainless steel," *Mater. Chem. Phys.*, 2003, doi: 10.1016/S0254-0584(03)00084-1.
- [85] C. F. Dong, X. G. Li, Z. Y. Liu, and Y. R. Zhang, "Hydrogen-induced cracking and healing behaviour of X70 steel," *J. Alloys Compd.*, 2009, doi: 10.1016/j.jallcom.2009.05.085.
- [86] D. L. Johnson, G. Krauss, J. K. Wu, and K. P. Tang, "Correlation of microstructural parameters and hydrogen permeation in carbon steel," *Metall. Trans. A, Phys. Metall. Mater. Sci.*, 1987.
- [87] W. Y. Choo and J. Y. Lee, "Effect of cold working on the hydrogen trapping phenomena in pure iron," *Metall. Trans. A*, 1983, doi: 10.1007/BF02664812.
- [88] T. Hara, H. Asahi, and H. Ogawa, "Conditions of hydrogen-induced corrosion occurrence of X65 grade line pipe steels in sour environments," *Corrosion*, vol. 60, no. 12, pp. 1113–1121, 2004, doi: 10.5006/1.3299225.
- [89] J. Kittel, V. Smanio, L. Garnier, and X. Lefebvre, "Hydrogen induced cracking (HIC) testing of low alloy steel in sour environment - Impact of time of exposure on the extent of damage," in *European Corrosion Congress 2009, EUROCORR 2009*, 2009.
- [90] J. Takahashi, K. Kawakami, Y. Kobayashi, and T. Tarui, "The first direct observation of hydrogen trapping sites in TiC precipitation-hardening steel through atom probe tomography," *Scr. Mater.*, 2010, doi: 10.1016/j.scriptamat.2010.03.012.
- [91] S. Nafisi, M. Arafin, B. S. Amirkhiz, R. Glodowski, L. Collins, and J. Szpunar, "Effect of vanadium addition on API X100 linepipe steel," in *HSLA Steels 2015, Microalloying 2015 and Offshore Engineering Steels 2015 Conference Proceedings*, 2015.
- [92] G. M. Pressouyre and I. M. Bernstein, "A quantitative analysis of hydrogen trapping," *Metall. Trans. A*, 1978, doi: 10.1007/BF02661939.
- [93] H. G. Lee and J. Y. Lee, "Hydrogen trapping by TiC particles in iron," *Acta Metall.*, 1984, doi: 10.1016/0001-6160(84)90210-4.
- [94] J. Moon, C. Park, and S. J. Kim, "Influence of Ti addition on the hydrogen induced cracking of API 5L X70 hot-rolled pipeline steel in acid sour media," *Met. Mater. Int.*, 2012, doi: 10.1007/s12540-012-4007-x.

- [95] F. G. Wei and K. Tsuzaki, “Quantitative analysis on hydrogen trapping of TiC particles in steel,” *Metall. Mater. Trans. A Phys. Metall. Mater. Sci.*, 2006, doi: 10.1007/s11661-006-0004-3.
- [96] F. G. Wei, T. Hara, and K. Tsuzaki, “Nano-precipitates design with hydrogen trapping character in high strength steel,” in *Advanced Steels*, 2011.
- [97] J. Takahashi, K. Kawakami, and T. Tarui, “Direct observation of hydrogen-trapping sites in vanadium carbide precipitation steel by atom probe tomography,” *Scr. Mater.*, 2012, doi: 10.1016/j.scriptamat.2012.04.022.
- [98] A. Nagao, M. L. Martin, M. Dadfarnia, P. Sofronis, and I. M. Robertson, “The effect of nanosized (Ti,Mo)C precipitates on hydrogen embrittlement of tempered lath martensitic steel,” *Acta Mater.*, vol. 74, pp. 244–254, 2014, doi: 10.1016/j.actamat.2014.04.051.
- [99] A. Turk, D. San Martín, P. E. J. Rivera-Díaz-del-Castillo, and E. I. Galindo-Nava, “Correlation between vanadium carbide size and hydrogen trapping in ferritic steel,” *Scr. Mater.*, 2018, doi: 10.1016/j.scriptamat.2018.04.013.
- [100] L. Li, B. Song, J. Cheng, Z. Yang, and Z. Cai, “Effects of vanadium precipitates on hydrogen trapping efficiency and hydrogen induced cracking resistance in X80 pipeline steel,” *Int. J. Hydrogen Energy*, vol. 43, no. 36, pp. 17353–17363, 2018, doi: 10.1016/j.ijhydene.2018.07.110.
- [101] S. Ogiyayashi, T. Mukai, M. Hirai, M. Tezuka, M. Yamada, and S. Mizoguchi, “Control of center segregation in continuous cast slabs for sour gas service line pipe steels,” in *7th Japan-Germany Seminar*, 1987, p. 309.
- [102] N. Zan, H. Ding, X. Guo, Z. Tang, and W. Bleck, “Effects of grain size on hydrogen embrittlement in a Fe-22Mn-0.6C TWIP steel,” *Int. J. Hydrogen Energy*, vol. 40, no. 33, pp. 10687–10696, 2015, doi: 10.1016/j.ijhydene.2015.06.112.
- [103] E. Fallahmohammadi, F. Bolzoni, G. Fumagalli, G. Re, G. Benassi, and L. Lazzari, “Hydrogen diffusion into three metallurgical microstructures of a C-Mn X65 and low alloy F22 sour service steel pipelines,” in *International Journal of Hydrogen Energy*, 2014, doi: 10.1016/j.ijhydene.2014.06.122.
- [104] K. Takasawa, Y. Wada, R. Ishigaki, and R. Kayano, “Effects of grain size on hydrogen environment embrittlement of high strength low alloy steel in 45 MPa gaseous hydrogen,” *Strength, Fract. Complex.*, 2011, doi: 10.3233/SFC-2011-0127.
- [105] T. Tanaka, “Controlled rolling of steel plate and strip,” *Int. Met. Rev.*, vol. 26, no. 1, pp. 185–212, Jan. 2014, doi: 10.1179/imtr.1981.26.1.185.
- [106] S. U. Koh, H. G. Jung, K. B. Kang, G. T. Park, and K. Y. Kim, “Effect of microstructure on hydrogen-induced cracking of linepipe steels,” *Corrosion*, vol. 574–585, no. 64, p. 7, 2008.
- [107] A. Brown and C. L. Jones, “Hydrogen induced cracking in pipeline steels,” *Corrosion*, vol. 40, no.

- 7, pp. 330–336, 1984.
- [108] J. Nieto *et al.*, “Development of technology for the production of HIC resistant slabs for sour service applications at Arcelormittal Lazaro Cardenas,” *Mater. Sci. Technol.*, pp. 1044–1053, 2012.
- [109] G. T. Park, S. U. Koh, H. G. Jung, and K. Y. Kim, “Effect of microstructure on the hydrogen trapping efficiency and hydrogen induced cracking of linepipe steel,” *Corros. Sci.*, vol. 50, no. 7, pp. 1865–1871, 2008, doi: 10.1016/j.corsci.2008.03.007.
- [110] B. Beidokhti, A. Dolati, and A. H. Koukabi, “Effects of alloying elements and microstructure on the susceptibility of the welded HSLA steel to hydrogen-induced cracking and sulfide stress cracking,” *Mater. Sci. Eng. A*, 2009, doi: 10.1016/j.msea.2008.11.064.
- [111] E. Ohaeri, U. Eduok, and J. Szpunar, “Relationship between microstructural features in pipeline steel and hydrogen assisted degradation,” *Eng. Fail. Anal.*, vol. 96, no. November 2018, pp. 496–507, 2019, doi: 10.1016/j.engfailanal.2018.11.008.
- [112] H. Tamehiro, T. Takeda, S. Matsuda, K. Yamamoto, and N. Okumura, “Effect of accelerated cooling after controlled rolling on the hydrogen induced cracking resistance of line pipe steel,” *Trans. Iron Steel Inst. Japan*, vol. 25, no. 9, pp. 982–988, 1985, doi: 10.2355/isijinternational1966.25.982.
- [113] M. Masoumi, C. C. Silva, M. Béreš, D. H. Ladino, and H. F. G. de Abreu, “Role of crystallographic texture on the improvement of hydrogen-induced crack resistance in API 5L X70 pipeline steel,” *Int. J. Hydrogen Energy*, vol. 42, no. 2, pp. 1318–1326, 2017, doi: 10.1016/j.ijhydene.2016.10.124.
- [114] J. I. Verdeja, J. Asensio, and J. A. Pero-Sanz, “Texture, formability, lamellar tearing and HIC susceptibility of ferritic and low-carbon HSLA steels,” *Mater. Charact.*, 2003, doi: 10.1016/S1044-5803(03)00106-2.
- [115] J. Xu, R. D. K. Misra, B. Guo, Z. Jia, and L. Zheng, “Understanding variability in mechanical properties of hot rolled microalloyed pipeline steels: Process-structure-property relationship,” *Mater. Sci. Eng. A*, vol. 574, pp. 94–103, Jul. 2013, doi: 10.1016/j.msea.2013.03.017.
- [116] V. Venegas, F. Caleyó, O. Herrera, J. Hernández-Sánchez, and J. M. Hallen, “Crystallographic texture helps reduce hydrogen induced cracking in pipeline steels,” *Int. J. Electrochem. Sci.*, 2014.
- [117] V. Venegas, F. Caleyó, J. M. Hallen, T. Baudin, and R. Penelle, “Role of crystallographic texture in hydrogen-induced cracking of low carbon steels for sour service piping,” *Metall. Mater. Trans. A Phys. Metall. Mater. Sci.*, 2007, doi: 10.1007/s11661-007-9130-9.
- [118] M. Masoumi, H. L. F. Coelho, S. S. M. Tavares, C. C. Silva, and H. F. G. de Abreu, “Effect of grain orientation and boundary distributions on hydrogen-induced cracking in low-carbon-content steels,” *JOM*, 2017, doi: 10.1007/s11837-017-2319-5.
- [119] M. A. V. Devanathan and Z. Stachurski, “The adsorption and diffusion of electrolytic hydrogen in palladium,” *Proc. R. Soc. London. Ser. A. Math. Phys. Sci.*, vol. 270, no. 1340, 1962, doi:

10.1098/rspa.1962.0205.

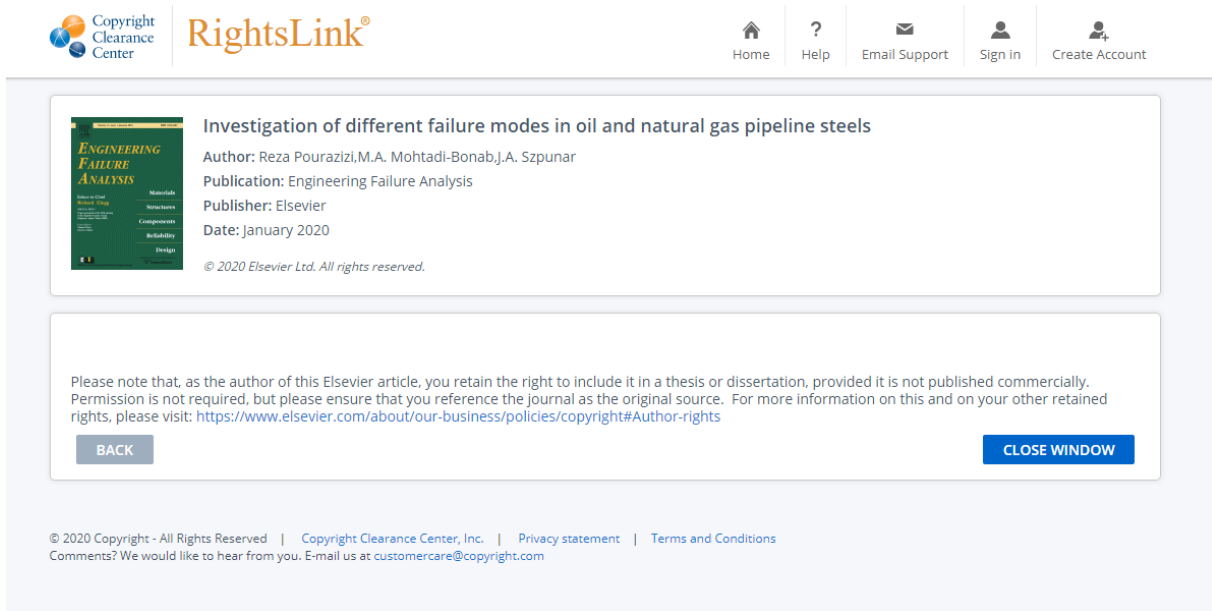
- [120] M. A. Mohtadi-Bonab, M. Eskandari, K. M. M. Rahman, R. Ouellet, and J. A. Szpunar, “An extensive study of hydrogen-induced cracking susceptibility in an API X60 sour service pipeline steel,” *Int. J. Hydrogen Energy*, 2016, doi: 10.1016/j.ijhydene.2016.01.031.
- [121] ASTM (American Society for Testing and Materials) standard, *E8/E8M standard test methods for tension testing of metallic materials*. 2010.
- [122] ASTM standard, “Standard test method for microindentation hardness of materials,” *ASTM Int.*, vol. E384, pp. 1–40, 2017, doi: 10.1520/E0384-17.
- [123] M. A. Mohtadi-Bonab, J. A. Szpunar, and S. S. Razavi-Tousi, “Hydrogen induced cracking susceptibility in different layers of a hot rolled X70 pipeline steel,” *Int. J. Hydrogen Energy*, vol. 38, no. 31, pp. 13831–13841, 2013, doi: 10.1016/j.ijhydene.2013.08.046.
- [124] M. A. Mohtadi-Bonab, J. A. Szpunar, L. Collins, and R. Stankievech, “Evaluation of hydrogen induced cracking behavior of API X70 pipeline steel at different heat treatments,” *Int. J. Hydrogen Energy*, vol. 39, no. 11, pp. 6076–6088, 2014, doi: 10.1016/j.ijhydene.2014.01.138.
- [125] M. A. Mohtadi-Bonab, M. Eskandari, M. Sanayei, and S. Das, “Microstructural aspects of intergranular and transgranular crack propagation in an API X65 steel pipeline related to fatigue failure,” *Eng. Fail. Anal.*, 2018, doi: 10.1016/j.engfailanal.2018.08.014.
- [126] R. Pourazizi, M. A. Mohtadi-Bonab, and J. A. Szpunar, “Role of texture and inclusions on the failure of an API X70 pipeline steel at different service environments,” *Mater. Charact.*, vol. 164, no. April, p. 110330, 2020, doi: 10.1016/j.matchar.2020.110330.
- [127] M. Masoumi, C. C. Silva, and H. F. G. de Abreu, “Effect of crystallographic orientations on the hydrogen-induced cracking resistance improvement of API 5L X70 pipeline steel under various thermomechanical processing,” *Corros. Sci.*, vol. 111, pp. 121–131, 2016, doi: 10.1016/j.corsci.2016.05.003.
- [128] E. Ohaeri, U. Eduok, and J. Szpunar, “Hydrogen related degradation in pipeline steel: A review,” *International Journal of Hydrogen Energy*. 2018, doi: 10.1016/j.ijhydene.2018.06.064.

APPENDIX A: LIST OF PUBLICATIONS FROM THIS STUDY

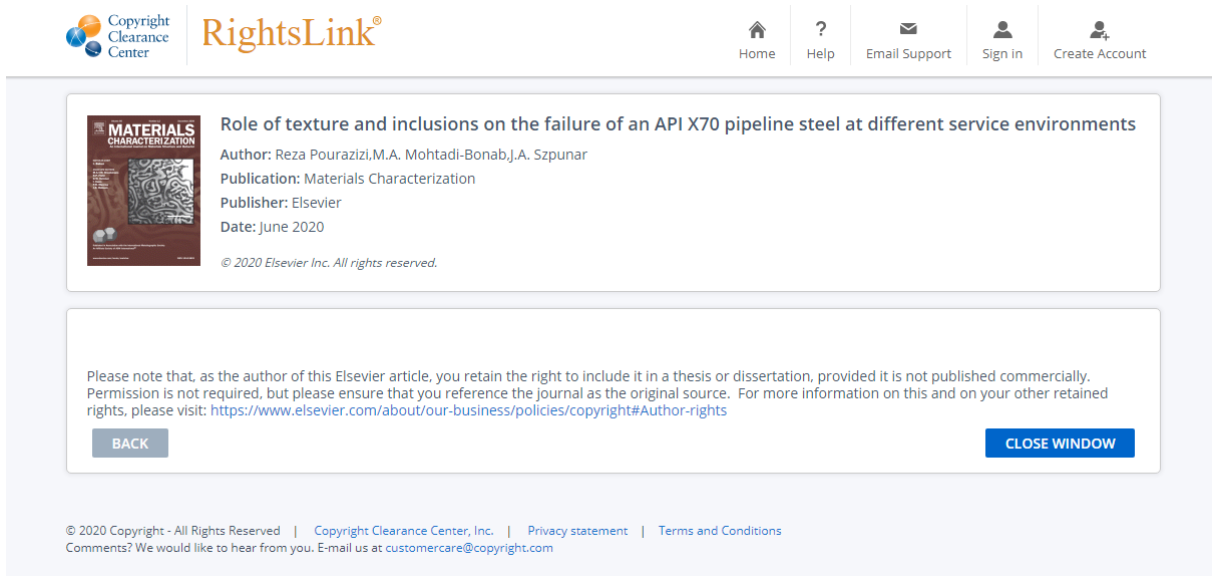
- 1- **R. Pourazizi**, M. A. Mohtadi-Bonab, and J. A. Szpunar, “Investigation of different failure modes in oil and natural gas pipeline steels,” *Eng. Fail. Anal.*, vol. 109, 2020.
- 2- **R. Pourazizi**, M. A. Mohtadi-Bonab, and J. A. Szpunar, “Role of texture and inclusions on the failure of an API X70 pipeline steel at different service environments,” *Mater. Charact.*, vol. 164, no. April, p. 110330, 2020.
- 3- M. A. Mohtadi-Bonab, H. Mousavi, **R. Pourazizi**, and J. A. Szpunar, “Finite element modeling of HIC propagation in pipeline steel with regard to experimental observations,” *Int. J. Hydrogen Energy*, vol. 45, no. 43, pp. 23122–23133, 2020, doi: 10.1016/j.ijhydene.2020.06.054.

APPENDIX B: ELSEVIER PERMISSION FOR USING PUBLISHED PAPER IN MY THESIS

Using the papers in the dissertation does not need the permission as long as they are cited in the body of the thesis.



The screenshot shows the RightsLink interface for an Elsevier article. At the top left are the Copyright Clearance Center and RightsLink logos. On the top right are navigation links: Home, Help, Email Support, Sign in, and Create Account. The main content area displays the article title, author (Reza Pourazizi, M.A. Mohtadi-Bonab, J.A. Szpunar), publication (Engineering Failure Analysis), publisher (Elsevier), and date (January 2020). A copyright notice states: © 2020 Elsevier Ltd. All rights reserved. Below this is a disclaimer: "Please note that, as the author of this Elsevier article, you retain the right to include it in a thesis or dissertation, provided it is not published commercially. Permission is not required, but please ensure that you reference the journal as the original source. For more information on this and on your other retained rights, please visit: <https://www.elsevier.com/about/our-business/policies/copyright#Author-rights>". At the bottom of the content area are "BACK" and "CLOSE WINDOW" buttons. The footer contains copyright information and contact details for the Copyright Clearance Center.



The screenshot shows the RightsLink interface for another Elsevier article. At the top left are the Copyright Clearance Center and RightsLink logos. On the top right are navigation links: Home, Help, Email Support, Sign in, and Create Account. The main content area displays the article title, author (Reza Pourazizi, M.A. Mohtadi-Bonab, J.A. Szpunar), publication (Materials Characterization), publisher (Elsevier), and date (June 2020). A copyright notice states: © 2020 Elsevier Inc. All rights reserved. Below this is a disclaimer: "Please note that, as the author of this Elsevier article, you retain the right to include it in a thesis or dissertation, provided it is not published commercially. Permission is not required, but please ensure that you reference the journal as the original source. For more information on this and on your other retained rights, please visit: <https://www.elsevier.com/about/our-business/policies/copyright#Author-rights>". At the bottom of the content area are "BACK" and "CLOSE WINDOW" buttons. The footer contains copyright information and contact details for the Copyright Clearance Center.



Sulfide stress cracking resistance of API-X100 high strength low alloy steel

Author: M. Al-Mansour, A.M. Afantazi, M. El-boujdaini
Publication: Materials & Design
Publisher: Elsevier
Date: December 2009

Copyright © 2009 Elsevier Ltd. All rights reserved.

Order Completed

Thank you for your order.

This Agreement between Mr. Reza Pourazizi ("You") and Elsevier ("Elsevier") consists of your license details and the terms and conditions provided by Elsevier and Copyright Clearance Center.

Your confirmation email will contain your order number for future reference.

License Number 4967720861774

[Printable Details](#)

License date Dec 14, 2020

Licensed Content

Licensed Content Publisher Elsevier
Licensed Content Publication Materials & Design
Licensed Content Title Sulfide stress cracking resistance of API-X100 high strength low alloy steel
Licensed Content Author M. Al-Mansour, A.M. Afantazi, M. El-boujdaini
Licensed Content Date Dec 1, 2009
Licensed Content Volume 30
Licensed Content Issue 10
Licensed Content Pages 7
Journal Type S&T

Order Details

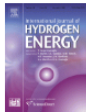
Type of Use reuse in a thesis/dissertation
Portion figures/tables/illustrations
Number of figures/tables/illustrations 1
Format both print and electronic
Are you the author of this Elsevier article? No
Will you be translating? No

About Your Work

Title Microstructure Optimization to Prevent Hydrogen-Induced Cracking of API X70 Pipeline Steels in Sour Environments
Institution name University of Saskatchewan
Expected presentation date Dec 2020

Additional Data

Portions Fig. 9. Longitudinal section of an X100 specimen loaded at 65%YS showing main SSC crack (right of image) and small microcracks (left of image) (light).



Influence of high pressure hydrogen on the tensile and fatigue properties of a high strength Cu-Al-Ni-Fe alloy

Author: Thorsten Michler, Jörg Naumann
Publication: International Journal of Hydrogen Energy
Publisher: Elsevier
Date: October 2010

Copyright © 2010 Professor T. Nejat Veziroglu. Published by Elsevier Ltd. All rights reserved.

Order Completed

Thank you for your order.

This Agreement between Mr. Reza Pourazizi ("You") and Elsevier ("Elsevier") consists of your license details and the terms and conditions provided by Elsevier and Copyright Clearance Center.

Your confirmation email will contain your order number for future reference.

License Number 4967730095699

[Printable Details](#)

License date Dec 14, 2020

Licensed Content

Licensed Content Publisher Elsevier
Licensed Content Publication International Journal of Hydrogen Energy
Licensed Content Title Influence of high pressure hydrogen on the tensile and fatigue properties of a high strength Cu-Al-Ni-Fe alloy
Licensed Content Author Thorsten Michler, Jörg Naumann
Licensed Content Date Oct 1, 2010
Licensed Content Volume 35
Licensed Content Issue 20
Licensed Content Pages 5
Journal Type S&T

Order Details

Type of Use reuse in a thesis/dissertation
Portion figures/tables/illustrations
Number of figures/tables/illustrations 1
Format both print and electronic
Are you the author of this Elsevier article? No
Will you be translating? No

About Your Work

Title Microstructure Optimization to Prevent Hydrogen-Induced Cracking of API X70 Pipeline Steels in Sour Environments
Institution name University of Saskatchewan
Expected presentation date Dec 2020

Additional Data

Portions Fig. 6. Stages of hydrogen material interactions.